

**INVESTIGATION OF STRESS DISTRIBUTION IN GLASS
FIBER REINFORCED COMPOSITE MATERIALS WITH
MICROVASCULAR CHANNELS UNDER TRANSVERSE
LOADING AND BENDING**

**MİKROVASKÜLER KANALA SAHİP CAM FİBER
DESTEKLİ KOMPOZİT MALZEMELERDEKİ GERİLİM
DAĞILIMLARININ ENİNE YÜKLEME VE EĞİLME
ALTINDA İNCELENMESİ**

ABDULLAH GENCER ATASOY

ASSOC. PROF. DR. BARIŞ SABUNCUOĞLU

Supervisor

DR. HAMED TANABİ

Co-Supervisor

Submitted to

Graduate School of Science and Engineering of Hacettepe University

as a Partial Fulfillment to the Requirements

for the Award of the Degree of Master of Science

in Mechanical Engineering

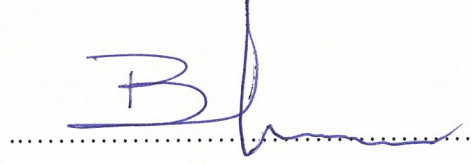
2019

i

This work titled “**Investigation of Stress Distribution in Glass Fiber Reinforced Composite Materials with Microvascular Channels Under Transverse Loading and Bending**” by **ABDULLAH GENCER ATASOY** has been as a thesis for the Degree of Master Of Science In Mechanical Engineering by the below mentioned Examining Committee Members.

Prof. Dr. Bora YILDIRIM

Head



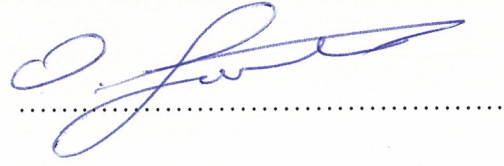
Assoc. Prof. Dr. Barış SABUNCUOĞLU

Supervisor




Dr. Mehmet Okan GÖRTAN

Member



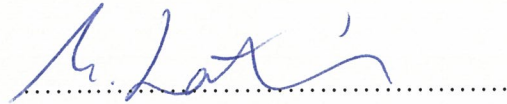
Dr. Reza AGHAZADEH

Member



Dr. Masoud LATIFI-NAVID

Member



This thesis has been approved as a thesis for the degree of **MASTER OF SCIENCE IN MECHANICAL ENGINEERING** by Board of Directors of the Institute for Graduate School of Science and Engineering on/..../.....

Prof. Dr. Menemşe GÜMÜŞDERELİOĞLU

Director of the Institute of

Graduate School of Science and Engineering

to my wife and my family...

ETHICS

In this thesis study, prepared in accordance with the spelling rules of Institute of Graduate School of Science and Engineering of Hacettepe University,

I declare that

- all the information and documents have been obtained in the base of academic rules
- all audio-visual and written information and results have been presented according to the rules of scientific ethics
- in case of using other works, related studies have been cited in accordance with the scientific standards
- all cited studies have been fully referenced
- I did not do any distortion in the data set
- and any part of this thesis has not been presented as another thesis study at this or any other university.

05 / 09 / 2019



Abdullah Gencer ATASOY

YAYINLANMA VE FİKRİ MÜLKİYET HAKKLARI BEYANI

Enstitü tarafından onaylanan lisansüstü tezimin tamamını veya herhangi bir kısmını, basılı (kağıt) ve elektronik formatta arşivleme ve aşağıda verilen koşullarla kullanıma açma iznini Hacettepe Üniversitesine verdiğimi bildiririm. Bu izinle Üniversiteye verilen kullanım hakları dışındaki tüm fikri mülkiyet haklarım bende kalacak, tezimin tamamının ya da bir bölümünün gelecekteki çalışmalarda (makale, kitap, lisans ve patent vb.) kullanım hakları bana ait olacaktır.

Tezin kendi orijinal çalışmam olduğunu, başkalarının haklarını ihlal etmediğimi ve tezimin tek yetkili sahibi olduğumu beyan ve taahhüt ederim. Tezimde yer alan telif hakkı bulunan ve sahiplerinden yazılı izin alınarak kullanması zorunlu metinlerin yazılı izin olarak kullandığımı ve istenildiğinde suretlerini Üniversiteye teslim etmeyi taahhüt ederim.

Yükseköğretim Kurulu tarafından yayınlanan “*Lisansüstü Tezlerin Elektronik Ortamda Toplanması, Düzenlenmesi ve Erişime Açılmasına İlişkin Yönerge*” kapsamında tezimi aşağıda belirtilen koşullar haricince YÖK Ulusal Tez Merkezi / H. Ü. Kütüphaneleri Açık Erişim Sisteminde erişime açılır.

- Enstitü / Fakülte yönetim kurulu kararı ile tezimin erişime açılması mezuniyet tarihimden itibaren 2 yıl ertelenmiştir.
- Enstitü / Fakülte yönetim kurulu gerekçeli kararı ile tezimin erişime açılması mezuniyet tarihimden itibaren ay ertelenmiştir.
- Tezim ile ilgili gizlilik kararı verilmiştir.

05. / 09 / 2019



Abdullah Gencer ATASOY

ÖZET

MİKROVASKÜLER KANALA SAHİP CAM FİBER DESTEKLİ KOMPOZİT MALZEMELERDEKİ GERİLİM DAĞILIMLARININ ENİNE YÜKLEME VE EĞİLME ALTINDA İNCELENMESİ

Abdullah Gencer ATASOY

Yüksek Lisans, Makina Mühendisliği Bölümü

Tez Danışmanı: Doç. Dr. Barış SABUNCUOĞLU

Eş Danışman: Dr. Hamed TANABİ

Eylül 2019, 67 sayfa

Kompozit malzemeler arasında yer alan fiber destekli kompozit malzemeler savunma sanayii, havacılık, otomotiv endüstrisi, denizcilik ve altyapı sektörlerinde yaygın olarak kullanılmaktadır. Bu malzemeler yüksek mukavemet, dayanıklılık, hafiflik ve maliyet etkinlik gibi çok önemli özelliklere sahiptirler.

Bu çalışma kapsamında mikrokanalların gömülü olduğu cam fiber destekli polimer kompozit malzemelerin enine yükleme altında gerilme dağılımları incelenmektedir. Söz konusu kanallar kendini yenileme, kompozitlerin aktif ısı yönetimi ile elektromanyetik yönetimi konularında çoklu işlevselliğini sağlamaktadır. Sayılan bu faydalar, mikrokanalların oluşturulduğu yerlerde mekanik mukavemetin düşmesi karşılığında sağlanmaktadır. Bu düşüşün temel sebebi fiber mimarisindeki bozulmanın reçine zengini cepler yaratarak gerilme yoğunlukları oluşturmasıdır. Enine yükler altındaki ve eğilme

altında farklı istifleme biçimleri incelenerek en iyi istifleme biçimine ilişkin öngörü sunulması amaçlanmaktadır.

Çalışma kapsamında fiber destekli kompozit malzemelere ilişkin klasik lamine teorisi ve imalat yöntemleri hakkında bilgi sunmaktadır. Modelin vasküler kanal etrafındaki geometri ve ölçüleri mikro-fotoğraflar tarafından elde edilmiştir. Müteakiben, sonlu elemanlar modeli geliştirilerek elde edilen sonuçların literatürde yer alan çalışmalar ile kıyaslaması yapılmak suretiyle doğrulması gerçekleştirilmiştir. Reçine zengini ceplerin enine basma, enine çekme yükleri ve eğilme altındaki gerilim dağılımları incelenmiştir. Elde edilen sonuçlar enine yüklemelerde UD90 konfigürasyonunun en fazla gerilim yoğunluğuna, UD0 konfigürasyonunun ise en düşük gerilim yoğunluğuna sahip olduğunu göstermiştir. Eğilme yükleri altında ise, mikrokanallı ve mikro kanalı olmayan lamina istiflemeleri kıyaslanarak, $[90/0]_{3s}$ konfigürasyonunun diğer konfigürasyonlara kıyasla en düşük gerilim farkına sahip olduğu tespit edilmiştir. Bu nedenle optimum istifleme konfigürasyonunun $[90/0]_{3s}$ olduğu bulunmuştur.

Anahtar Kelimeler: kompozit, mikrovasküler kanal, cam fiber takviyeli polimer, enine yük, eğilme

ABSTRACT

INVESTIGATION OF STRESS DISTRIBUTION IN GLASS FIBER REINFORCED COMPOSITE MATERIALS WITH MICROVASCULAR CHANNELS UNDER TRANVERSE LOADING AND BENDING

Abdullah Gencer ATASOY

Master's Thesis, Department of Mechanical Engineering

Supervisor: Assoc. Prof. Dr. Barış SABUNCUOĞLU

Co- Supervisor: Dr. Hamed TANABI

September 2019, 67 pages

Fiber reinforced polymer composites are widely utilized in the defense industry, aerospace, infrastructure and automotive industries. These materials have important properties like, durability, lightness, high strength and cost efficiency.

In this study, a glass fiber-reinforced polymer composite material with an embedded microvascular channel is researched for its stress distribution under transverse loads. Several research studies have been conducted on vascularized composites, aiming to develop techniques for health monitoring and self-healing through vascular channels. In spite of the aforementioned benefits, there is a trade-off regarding the reduction in mechanical strength where the microvascular channels are introduced. The main reason behind this is, the disruption of fiber architecture around the vasculature, creating resin-rich

pocket, leading to stress concentrations. By evaluating the stress concentrations under transverse loads and bending for different stacking configurations, the study aims to give insight for optimum configuration.

The study contains a general information about fiber-reinforced composite materials to grasp the basic knowledge about the classical laminate theory along with the manufacturing of the fiber reinforced polymer with microvascular channel. The geometry and dimension of the model near vascular channel is obtained by micro-pictures. Then, FEM is developed and validated with comparing the results obtained with the studies in the literature. The stress distributions for transverse tension, transverse compression and bending are analyzed for resin-rich pocket. The results showed that, UD90 configuration has the highest stress concentration while UD0 has the lowest under transverse loading. Under bending loads, by comparing the laminas with and without microchannels, it is found that $[90/0]_{3s}$ is the configuration that has the lowest stress difference. For this reason the optimum stacking configuration is found out to be $[90/0]_{3s}$.

Keywords: composite, microvascular channel, glass fiber reinforced polymer, transverse load, bending

ACKNOWLEDGMENT

Starting with, there are many people that contribute to this thesis to become what it is today, so I would like to thank them one by one.

I hereby imply my appreciation to my supervisor, Asst. Prof. Dr. Barış SABUNCUOĞLU, for his strong sense of patience and supervision. With his guidance, I was introduced to the world of composites, which I really enjoyed studying on.

I also want to state deep gratitude to my co-supervisor, Dr. Hamed TANABI, who assisted me on my researches on every step of my thesis. No matter what time of the day is, he was able to help me even with smallest details in my study.

I would like to thank to my committee members, whom gave me excellent critics to complete my thesis.

I'm really grateful for my family, my mother Hediye, my father Ömer and my brother Sencer, that made me available to continue my education life and supported me till this day.

Finally, I would give my greatest appreciation to my wife Başak, who gave me the opportunity to study with comfort from days to nights and provided me with every support she can give.

CONTENTS

ABSTRACT	viii
ACKNOWLEDGMENT	x
CONTENTS	xi
LIST OF TABLES.....	xiii
LIST OF FIGURES.....	xiv
SYMBOLS AND ABBREVIATIONS	xviii
1. INTRODUCTION.....	1
1.1 Aim and Objectives of the Thesis	2
1.2 Research Methodology.....	2
1.3 Main Frames of the Study.....	3
2. COMPOSITE MATERIALS	4
2.1. Definitions of Composite Materials	4
2.2 History of Composite Materials.....	4
2.3. Fiber Reinforced Composite Materials.....	4
2.3.1 Area of Utilization	5
2.3.2 Manufacturing	5
2.4. Macromechanical Analysis for Lamina	10
2.4.1 Hooke’s Law for Isotropic Materials	10
2.4.2 Hooke’s Law for Orthotropic Materials.....	12
2.5. Macromechanical Analysis for Laminate	12
2.5.1 Stacking Position.....	13
2.5.2 The Relations for Stress and Strain	14
2.5.3 The Relations for Forces and Moments in the Laminates	15
3. MICROVASCULAR CHANNELS IN COMPOSITE MATERIALS	16
3.1. Area of Utilization	16
3.2. Manufacturing.....	16

3.2.1 Vaporization of Sacrificial Components	16
3.2.2 Removable Solid Cores	17
3.2.3 Non-Removable Hollow Cores	17
3.3. Mechanical Behavior	19
4. FINITE ELEMENT ANALYSIS OF VASCULARIZED LAMINATE	20
4.1. About the Model	22
4.1.1. Finite Element Model Development of the Validation Model	22
4.1.2. Finite Element Model Development of the Present Model	27
5. RESULTS AND DISCUSSIONS	37
5.1. The Validation Model Results	37
5.2 Present Study Results	46
5.2.1 Longitudinal Stress Distributions for Transverse Compression:	46
5.2.2 Longitudinal Stress Distributions for Transverse Tension:	49
5.2.3 3-Point Bending:	52
6. CONCLUSIONS	61
6.1 Summary	61
6.2 Key Findings and Outcomes	61
6.3 Future Studies	62
REFERENCES	63
CURRICULUM VITAE	68
APPENDIX	69
THESIS/DISSERTATION ORIGINALITY REPORT	69

LIST OF TABLES

Table 1: The Elastic and Thermal Properties of IM7/8552 Composite Laminates and Hexcel 8552 Neat Epoxy [20]	24
Table 2: Comparison of Number of Elements and Number of Nodes in Huang et al. [20] and 2-D Validation Model	25
Table 3: Material properties for E-Glass fiber and Aradur-564: Araldite 2954 with %37 volume fraction	29
Table 4: The Material Properties Lamina 0 and Lamina 90 [76]	29
Table 5: Number of Elements and Number of Nodes in Present Model for Transverse Loads	32
Table 6: Number of Elements and Number of Nodes in Present Model for Transverse Loads and Bending Load	34
Table 7: The Difference in Maximum and Minimum Stresses of the Model with Microchannel and without Microchannel for 3 Point Bending Loads with y-Plane and z-Plane	53
Table 8: The Difference in Maximum and Minimum Stress Rates of Model with Microchannel and Without Microchannel for 3 Point Bending Loads with y-Plane and z-Plane	54

LIST OF FIGURES

Figure 1: A Schematic for Vacuum Bagging [25]	5
Figure 2: A Schematic for Compression Molding [23].....	6
Figure 3: A Typical Pultrusion Line [26].....	7
Figure 4: Filament Winding Schematic [27].....	7
Figure 5: Schematics for RTM Process for Desired Shapes of the Product [23].....	8
Figure 6: Schematics for VARTM Process [23]	9
Figure 7: Forming Methods of Thermoplastic Matrix Components for a) Matched Die Forming b) Hydroforming c) Thermoforming [23].....	10
Figure 8: Stiffness Matrix (C) and Compliance Matrix (S) for Anisotropic Materials [29]	11
Figure 9: Stiffness Matrix (C) and Compliance Matrix (S) for Isotropic Materials [29]	12
Figure 10: Stiffness Matrix (C) and Compliance Matrix (S) for Isotropic Materials [29]	12
Figure 11: A Drawing of a Laminate [29].....	13
Figure 12: A Laminate Geometry [23].....	14
Figure 13: Schematic for the Laminate Resultant Forces and Moments Acting on a Laminate [23]	15
Figure 14: Epoxy Composition and Curing Information	18
Figure 15: Schematic for Geometrical Parameters [21].....	23
Figure 16: Cutting Planes of the 3D Validation Model	23
Figure 17: Boundary Conditions and Loads for 2-D Validation Model	25
Figure 18: Boundary Conditions and Loads for 3-D Validation Model	25
Figure 19: A Display for the Resin Rich Portion of the 2-D Validation Model	26
Figure 20: A Display for the Resin Rich Portion of the 3-D Validation Model	26
Figure 21: A Display for the Mesh of the 3D Validation Model	27
Figure 22: Micro-pictures of GFRP samples with 1 mm diameter for: a) $[0/90]_{3s}$ and b) $[90/0]_{3s}$	27
Figure 23: The Dimensions of the Present Model for Transverse Loads.....	28
Figure 24: The Dimension of Specimen for 3-Point Bending	28

Figure 25: The Boundary Condition and Load for Present Model under Transverse Compression	30
Figure 26: The Boundary Condition and Load for Present Model under Transverse Tensile.....	30
Figure 27: The Boundary Condition Present Model under 3-Point Bending a) Displacement and No slip in z-Direction BC b) No slip in x-Direction and y-Direction BC	31
Figure 28: Comparison of S11 Contours with Different Number of Meshes for the Present Mesh in UD0 Stacking Configuration for a) Attempt 1 b) Attempt 2 c) Attempt 3	33
Figure 29: The Meshing of the Whole Model for the Present Model under Transverse Loads.....	34
Figure 30: The Meshing of the Area of Interest for the Present Model for Transverse Loads.....	34
Figure 31: The Meshing of the Present Model for 3-Point Bending a) with Microchannel b) without Microchannel.....	35
Figure 32: An Illustration of the Bent Model	35
Figure 33: The Meshing of the Area of Interest for the Present Model for 3-Point Bending a) with Microchannel b) without Microchannel	36
Figure 34: Comparison of Normalized σ_x along the x-axis for 2-D Validation Model and Huang's Plane Strain Model	38
Figure 35: Comparison of Normalized σ_x along x-axis for 3-D Validation Model and Huang's Plane Strain Model	38
Figure 36: Comparison of Normalized σ_y along the x-axis for 2-D Validation Model and Huang's Plane Strain Model for Point C to Point A.....	39
Figure 37: Comparison of Normalized σ_y along x-axis for 3-D Validation Model and Huang's Plane Strain Model for Point C to Point A.....	39
Figure 38: Comparison of Normalized σ_y along the BDA for 2-D Validation Model and Huang's Plane Strain Model for B-D-A Points	40
Figure 39: Comparison of Normalized σ_y along the BDA for 3-D Validation Model and Huang's Plane Strain Model for B-D-A Points	40
Figure 40: Comparison of S,Min, Principal Values of 2-D Validation Model, 3-D Validation Model and Huang's Plane Strain Model.....	41

Figure 41: Comparison of S,Max, Principal Values of 2-D Validation Model, 3-D Validation Model and Huang’s Plane Strain Model	42
Figure 42: Comparison of E,Min, Principal Values of 2-D Validation Model, 3-D Validation Model and Huang’s Plane Strain Model	43
Figure 43: Comparison of E,Max, Principal Values of 2-D Validation Model, 3-D Validation Model and Huang’s Plane Strain Model	44
Figure 44: Longitudinal Stress Contours for the Validation Model (a) with Curing Effects, (b) without Curing Effects.....	45
Figure 45: Transverse Stress Contours for the Validation Model (a) with Curing Effects, (b) without Curing Effects.....	46
Figure 46: Longitudinal Stress Distributions for Present Model under Transverse Compression for a) UD0 b) UD90 c) [0/90] _{3s} d) [90/0] _{3s}	47
Figure 47: Normalized σ_x Distribution for 1 mm Channel Diameter through Point B to Point A under Transverse Compression	48
Figure 48: Normalized σ_x Distribution for 1 mm Channel Diameter through Point C to Point A under Transverse Compression	49
Figure 49: Longitudinal Stress Distributions for Present Model under Transverse Tensile for a) UD0 b) UD90 c) [0/90] _{3s} d) [90/0] _{3s}	50
Figure 50: Normalized σ_x Distribution for 1 mm Vasculature Diameter through Point B to Point A under Transverse Tension	51
Figure 51: Normalized σ_x Distribution for 1 mm Vasculature Diameter through Point C to Point A under Transverse Tension	52
Figure 52: Investigation of 3-Point Bending Model’s Cross Section a) y-plane b) z-plane	52
Figure 53: S,Max, Principal Stress Contours for the 3-Point Bending Model with [90/0] _{3s} Stacking Configuration for y-plane Cut (a) with (b) without Microchannel..	55
Figure 54: S,Max, Principal Stress Contours for the 3-Point Bending Model with [90/0] _{3s} Stacking Configuration for z-plane Cut (a) with (b) without Microchannel ..	55
Figure 55: S,Max,Principal Stress Contours for the 3-Point Bending Model with [0/90] _{3s} Stacking Configuration for y-plane cut for (a) with Microchannel (b) without Microchannel	56

Figure 56: S,Max,Principal Stress Contours for the 3-Point Bending Model with [0/90] _{3s} Stacking Configuration for z-plane cut for (a) with Microchannel (b) without Microchannel.....	57
Figure 57: S, Max, Principal Stress Contours for the 3-Point Bending Model with UD0 Stacking Configuration for y-plane Cut (a) with Microchannel (b) without Microchannel.....	58
Figure 58: S,Max, Principal Stress Contours for the 3-Point Bending Model with UD0 Stacking Configuration for z-plane Cut (a) with Microchannel (b) without Microchannel.....	58
Figure 59: S,Max, Principal Stress Contours for the 3-Point Bending model with of UD90 Stacking Configuration for y-plane Cut for (a) with Microchannel (b) without Microchannel.....	59
Figure 60: S,Max,Principal Stress Contours for the 3-Point Bending Model with of UD90 Stacking Configuration for z-plane cut for (a) with Microchannel (b) without Microchannel.....	60

SYMBOLS AND ABBREVIATIONS

Symbols

C	Stiffness matrix
h_d	Disturbance Height
E	Modulus of Elasticity
ϵ_{xx}°	Midplane normal strains in the laminate in x direction
ϵ_{yy}°	Midplane normal strains in the laminate in y direction
G	Shear Modulus
(h_{j-1})	The distance from the midplane to the top of the j^{th} lamina,
(h_j)	The distance from the midplane to the bottoms of the j^{th} lamina,
K	Bulk Modulus
k_{xx}	The bending curvatures of the laminate in x direction
k_{yy}	The bending curvatures of the laminate in y direction
k_{xy}	The twisting curvatures of the laminate in xy-plane
L_{RP}	Resin Pocket Length
M	Resultant moment
M_{xx}	The resultant bending moment per unit width in the yz plane
M_{yy}	The resultant bending moment per unit width in the xz plane
M_{xy}	The resultant twisting (or torsion) force per unit length width
N	Resultant force
N_{xx}	The resultant normal force per unit width in the x direction
N_{yy}	The resultant normal force per unit width in the y direction
N_{xy}	The shear resultant force per unit length width

s	Symmetry
S	Compliance Matrix
T	Transformation Matrix
α	Thermal coefficient
ν	Poisson's Ratio
σ	Normal Stress
τ	Shear Stress
ε	Strain
γ	Shear Strain
θ	Fiber orientation angle
γ_{xy}°	Midplane shear strain in the laminate in xy-plane

Abbreviations

BC	Boundary Condition
CFRP	Carbon Fiber Reinforced Polymer
DOF	Degree of Freedom
FEA	Finite Element Analysis
FEM	Finite Element Method
FRP	Fiber Reinforced Polymer
GFRP	Glass Fiber Reinforced Polymer
HGF	Hollow Glass Fiber
HGT	Hollow Glass Tube
IGFEM	Interface Enriched Generalized Finite Element Method
LCM	Liquid composite molding
Pa	Pascal

PLA	Poly lactide acid
RVE	Representative Volume Element
RTM	Resin Transfer Molding
SCRIP	Seemann's Composite Resin Infusion Molding Process
SRIM	Structural Reaction Injection Molding
UD	Unidirectional
UV	Ultraviolet
VARTM	Vacuum Assisted Resin Transfer Molding

1. INTRODUCTION

Composites basically consists of mixing of two different materials which are not soluble with each other in order to have better material properties compared to the constituents that form the composite. The type of composite that will be investigated is GFRP composite.

The application of FRP composite materials have a long history starting from utilization of clay bricks and reinforced straw but with the discovery of new fibers like boron and aramids the utilization of composite materials have greatly increased. The FRP composites have many applications in different fields. For instances, defense industry, aerospace, automotive industries, marine, infrastructure etc. These materials have important material properties such as high strength, durability, lightness and cost efficiency. In order to further increase these functionality of FRP composites channels in the magnitude of micrometers are introduced. These channels are called microchannels. There are various studies for increasing the functionality of the composite materials. For instance, implementations of optical fibers [1], [2], piezoelectric materials and sensors [2][3] making use of shape memory polymer and its alloys [4], [5] using nanoparticles [6], [7], [2]. To further enhance these multi-functionalities self-healing [8]–[13], active thermal management [14], [15], electromagnetic management of composite materials [6], better damage visibility [16], [17] and sensing [18], [19].

In the scope of the study a glass fiber-reinforced polymer (GRFP) composite material that is embedded with microvascular channel is researched for its stress distribution under transverse and bending loads. Despite having these multi-functionality advantages there are some disadvantages that results in reducing the mechanical strength where the microvascular channels are introduced. Huang et al. [20]'s studies show that in the application of circular microvascular channels in carbon fiber reinforced polymer composites, there is 13% - 70% reduction in compressive strength around the vasculs. In Al-Shawk et al. [21] studied about glass fiber-reinforced polymer composite material's stress distribution, stress concentration and failure assessment under tensile loading for different stacking configurations and vasculs sizes via finite element method. As the

result of their study [21], UD0 stacking configuration, is strongest against resin failure, sensitive for vasculature diameters change, comparing to the rest and using elliptical vasculatures for microchannels resulted in reduction in stress concentrations.

1.1 Aim and Objectives of the Thesis

The first and foremost aim of this study is to provide insight about stress distributions within the microchannels in GRFP composites and identify the most suitable stacking configuration under transverse and bending loads.

In the study, developing a computational modelling method to examine the stress distributions and concentrations in a GRFP composite material with microvascular channels is elaborated. Under transverse compression, transverse tensile and bending loads, the effect of stacking sequence is studied. The geometry and dimension of the model near vascular channel were captured by micro-CT analysis of the GRFP laminates with vascular channel diameter of 1 mm. The model's material properties are obtained from the sample that is produced, tested in University of Turkish Aeronautical Association's Laboratory and the analyses are made on this model are presented accordingly. In order to develop the model, a FEA is applied by ABAQUS/Standard software. The results obtained for the longitudinal transverse compression and transverse tensile loads focused on microchannels are presented.

1.2 Research Methodology

The thesis starts with the brief information about the fiber reinforced composite materials which later on focuses on GFRP composite materials. A literature review on vascularized composites is then presented by focusing on studies on mechanical behaviors of vascularized composites. Therefore, laminates with a vascular channel and various stacking configurations are modeled. The model is validated with respect to the presented results in literature. Further analyses are done on the validated model under various loading conditions. The modelling is done based on the previous studies on the literature, creating the validation model in order to facilitate the analysis. A validation model is created by Huang et al. [21]'s study. Same dimensions and material properties are used for validation purposes. However, there is distinct difference. Unlike Huang et al. [21]'s

study which is 2-D, the validation model generated as both 2-D and 3-D model. This enables studying for various laminate angles and makes the analysis suitable for different types of load like bending.

After validating this model, the steps taken for validation model are used to create present model. In the 3-Point Bending analysis, a model without microchannel and with microchannel with 1mm diameter is created. The results for validation and present model that includes transverse and bending loads, are afterwards stated. In the conclusion part, the evaluations are presented about the studies that are presented within the thesis.

1.3 Main Frames of the Study

The thesis mainly consists of five parts excluding this part. Summary of these parts are given below:

1. General Information about Fiber Reinforced Composite Materials

Definitions, types of composite materials, the manufacturing techniques of GRFPs and classical laminate theory are presented in this section.

2. Microvascular Channels in Composite Materials

Definition, manufacturing methods and mechanical behavior of vascularized composites are given.

3. Finite Element Analysis of Vascularized Laminate

A laminate with a microvascular channel is modelled in this part. The studies regarding the validation model and present model is given.

4. Results and Discussions

The results obtained from the validation model and present model are stated in this part.

5. Conclusions

The brief summary and results of the studies presented within thesis is given in this part. In addition, studies that may be done in the future is also given.

2. COMPOSITE MATERIALS

2.1. Definitions of Composite Materials

Composites comprise of two or more materials. These materials that form the composite don't form solution, and combine at a macroscopic level. Constituents are called reinforcing phase and matrix. The reinforcing phase is embedded in matrix phase. The reinforcing phase material's shape may vary such as fibers, particles or flakes. As for matrix phase, they are mostly continuous.

Actually, composite materials are not fully man-made at all. There are some good examples of naturally found composite as well such as wood and bone.

2.2 History of Composite Materials

If we look through the history, earliest examples of the composite materials start with Israelites who used clay bricks and reinforced straw. They discovered that if those materials used together they can serve the purpose rather than used solely. There are many cases that composite materials are used. For instance, in 1500 B. C's, reinforcing the mud walls of the houses are reinforced via bamboo shoots. Around 1800s, laminated metals are used for forging swords. In recent years, carbon, boron and aramids (aromatic compounds of C, H, O and N) are developed quite fast. Due to this development, implementation of composites are increasing day by day. [21]

2.3. Fiber Reinforced Composite Materials

Fiber reinforced composites materials comprise of high strength fibers which have good load bearing capacity and a matrix that protects and keeps the structure in the desired orientation by acting as load transfer function between the fibers and also protects against severe environment condition like high temperature and humidity [22].

The general form of fiber reinforced composite materials are called laminate that is formed by stacking a certain number of thin layers of fibers and matrix to achieve a desired thickness. By changing the order of these stacking and fiber orientation different physical and mechanical properties can be achieved. [23]

2.3.1 Area of Utilization

Fiber reinforced polymer composites has many applications in various fields. For instance, defense industries, aircraft, space, automotive, sporting goods, marine and infrastructure are the major areas. The reason that composite used in these areas may vary but the most common reason may be weight reduction. [24]

2.3.2 Manufacturing

In order to transform the fiber-reinforced thermoset polymers into a composite part, the material must be cured to an elevated temperature and pressure for a predetermined timeframe. These polymers may be uncured or partially cured. The high curing temperature is required for initiating and sustaining the chemical reaction. There are two reason for using high pressure. The first reason overcoming the resin's high viscosity. The second one is, plies needs much pressure for bonding together to form laminate.

2.3.2.1 Bag-molding process

In this process, pressure, which can be applied by a bag or diaphragm, is applied before the curing of the laminate to improve consolidation of the fibers and removal of the excess air, resin and volatiles from the matrix. [25] The laminae are laid in the mold and impregnated with resin. Preventing the laminae sticking to mold is important. For this a release film or agent is used. In some cases, a peel-ply is used to leave a pattern on the surface to enhance adhesive bonding later on. The breather/bleeder combination is used for distribution of the vacuum and letting out the excess air, resin and volatiles to vacuum port. Then, the laminate is covered with the flexible bag and vacuum and heat is applied. After curing, the vacuum extracts the excess components (air etc.) in the resin. Finally, the materials turn to a desired configuration of the molded shape. A schematic for vacuum bagging is given in Figure 1.

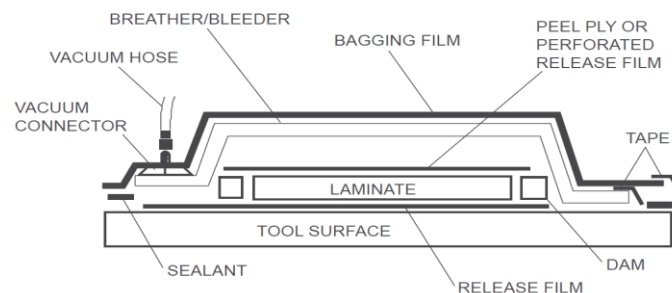


Figure 1: A Schematic for Vacuum Bagging [25]

2.3.2.2. Compression molding

SMC's are turned into finished products in matched molds. Primary benefit of this process is being able to manufacture complex parts in short amount of time. Considering this advantage, the compression molding is quite suitable for serial production. Ribs, bosses, flanges, can be produced with this method of manufacturing. In Figure 2, a schematic for compression molding is presented. With compression molding a secondary finishing operation like welding, drilling, forming etc. is not needed. Having simplicity for production, this process can be automated easily. It can be easily said that; this is quite convenient for high-volume production. [23]

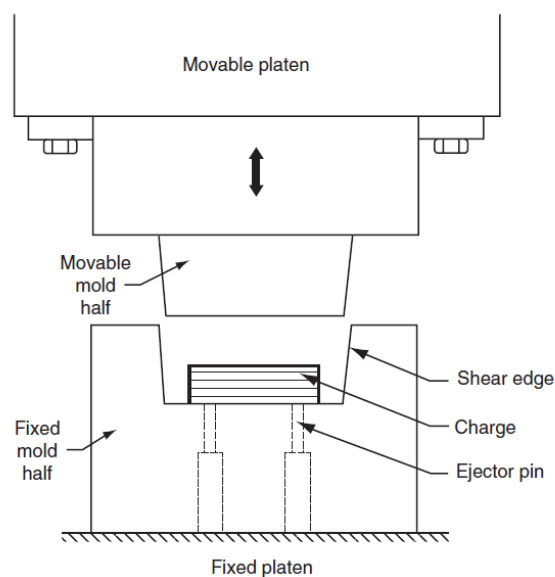


Figure 2: A Schematic for Compression Molding [23]

2.3.2.3. Pultrusion

The pultrusion process allows a continuous, automated, quality controlled and cost-effective way of production of different profile geometries for series production. Beams, frame constructions, car bumpers can be given an example for parts that can be produced via pultrusion. The reinforcing fiber materials are provided by creel and the fibers are pulled from end of the production line in one way. In order not to have a misalignment in the fibers pre-stress can be applied. The fibers then go through the resin impregnation either with a resin bath tank or with drawing chamber injection system. During impregnation, air the air and moisture inside the fibers are let out. Fibers need to consolidate, formed, calibrated and cured. For this a heated and cooled forming die is

needed. Finally, the profiles are cut for arbitrarily. A schematic for typical pultrusion line is presented in Figure 3. [26]

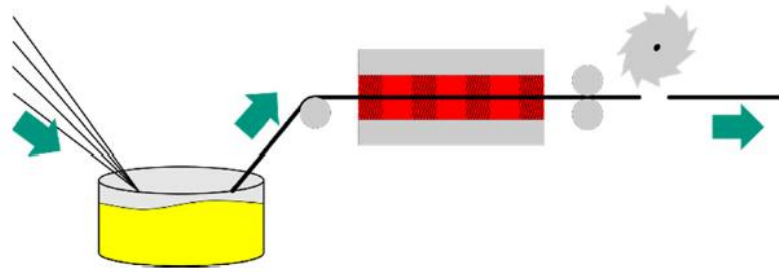


Figure 3: A Typical Pultrusion Line [26]

2.3.2.4 Filament winding

This production method is an automatic manufacturing process to create axisymmetric and some of the non-axisymmetric parts. In this process, two ways of winding exist. For wet winding, dry fibers pass through a resin bath and for dry winding, prepreg materials are used. [27] The filament winding process can be summarized as following: the rovings are gathered together from creels, then pulled into resin and catalyst bath. The excess resin is wiped form the rovings. Then, rovings merged to form a flat band. With this, they got positioned on the mandrel. Lastly, the band travelling back and forth on a carriage forms that forms a helical winding pattern on a part. A schematic for filament winding is presented in Figure 4.

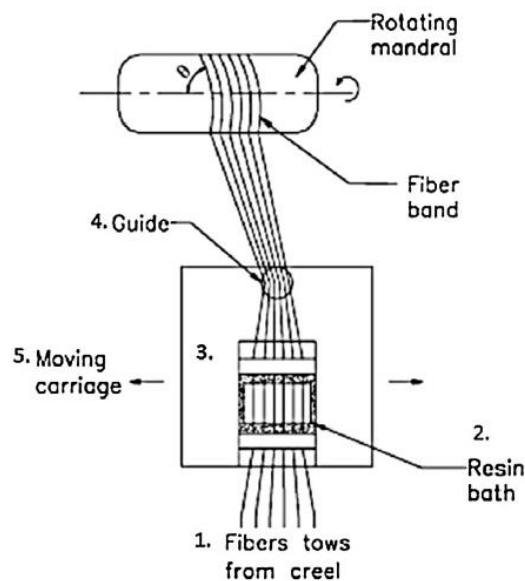


Figure 4: Filament Winding Schematic [27]

2.3.2.5. Liquid Composite Molding Processes

The process takes place in a closed mold. The dry fiber preform is injected with premixed liquid thermoset resin. The liquid thermoset resin is spreads and coats the fibers, expelling the air and by curing this mixture turns into a matrix. There are two methods for Liquid Composite Molding, the first one is Resin Transfer Molding (RTM) and the other one is Structural Reaction Injection Molding (SRIM).

2.3.2.5.1. Resin Transfer Molding

In this molding process, a number of dry continuous strand mat, cloth or a woven roving are placed in the bottom part of the two-part mold and as the mold closes, a catalyzed liquid is injected from sprue and resin spreads in the mold and fills the space in the fibers via injection pressure that removes the entrapped air out of the fibers from air vents. [23] After curing to the desired temperature and then cooling off, the outer edges of the part is needed to match the desired dimensions. Besides the flat reinforcing layers like continuous strand mat, the preforms that are already in the desired shape of the product can be used. Some examples of schematics for this RTM process are presented in Figure 5.

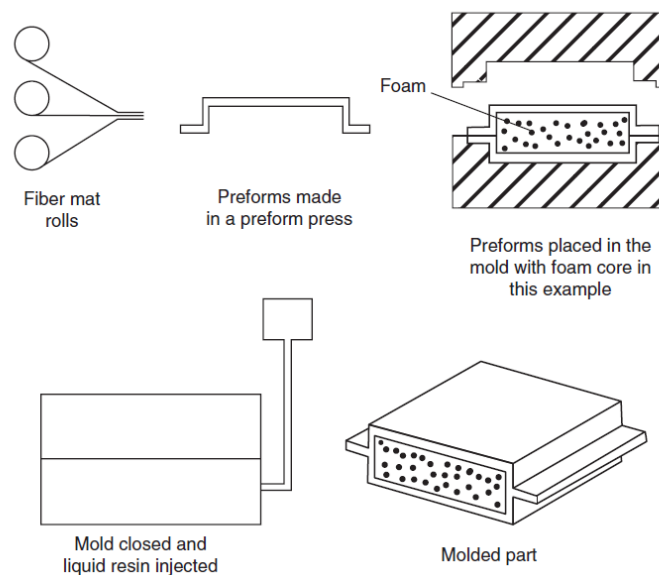


Figure 5: Schematics for RTM Process for Desired Shapes of the Product [23]

There are various ways for RTM processes. One of the most common method is vacuum VARTM. In this method, vacuum pulls resin into preform along with resin injection

system. Schematic for VARTM is presented in Figure 6. Another method is called SCRIMP. In this method, vacuum is also used for pulling liquid resin into the resin. However, the main difference from VARTM is, using a porous layer. The layer has low resistance to flow. With this, liquid resin easily flows. [2]

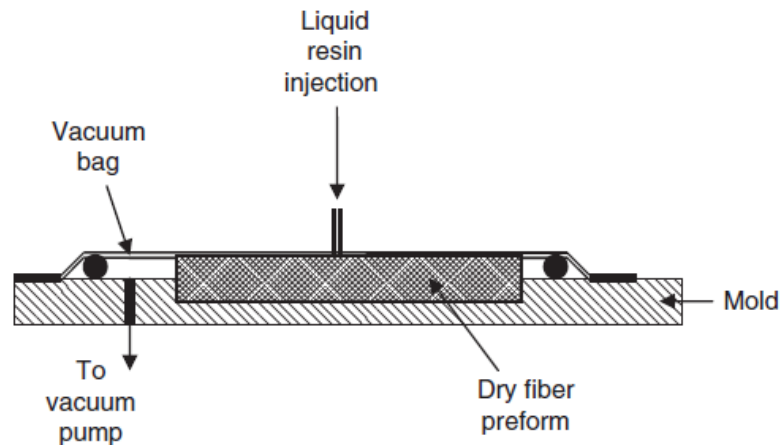


Figure 6: Schematics for VARTM Process [23]

2.3.2.5.2. Structural Reaction Injection Molding

Inside the mold there is a dry preform. The resin and initiator are in separate tanks due to their high chemical activity. First, the mixture of resin and initiator are injected to the mixing chamber and then mixture is pumped to the mold, where it is cured at high speed.

2.3.2.6. Other manufacturing processes

The most common methods for producing the fiber reinforced polymer composites are presented till this part. In addition to these method, there numerous processes like “resin film infusion”, “elastic reservoir molding”, “tube rolling” which will not be covered by this study.

2.3.2.7. Manufacturing Processes for Thermoplastic Matrix Composites

Previous processes are generally for thermoset matrix composites but they can also be applied for thermoplastic matrices as well. However, due to the thermoplastic matrices’ material properties, the molding characteristics has to be different for some cases. For instance, the thermoplastic prepregs lacks stickiness. Therefore, the prepregs need to be

spot-welded from their outer edges.[23] Also, the thermoplastic matrix needs higher temperatures to be cured. So, the mold needs to be heat-resistance even more comparing to the thermoset ones. Another difference is, having no chemical reaction in the process to form thermoplastic matrix composites. Despite that, individual plies still needs to be consolidated. Therefore time and high temperature is needed. Schematics for forming thermoplastic matrix composites for different methods are presented in Figure 7. [23]

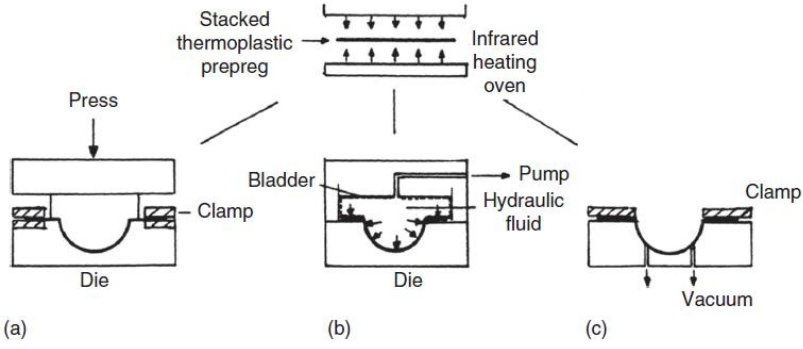


Figure 7: Forming Methods of Thermoplastic Matrix Components for a) Matched Die Forming b) Hydroforming c) Thermoforming [23]

2.4. Macromechanical Analysis for Lamina

The word “lamina”, “ply” or “layer” corresponds to a thin layer of composite which is formed by arranging the unidirectional or multidirectional fibers in a matrix and “laminates” corresponds to a stack of laminae bonded together to form a multilayered sheet of composite. [28] The stacking direction is always in the lamina thickness. The structures consisting of these laminae are subjected to a number of loads. To analyze the stress-strain behavior that corresponds to these loads on these laminates, one must understand lamina first. If lamina which are not isotropic homogeneous material, are mechanically modeled, it would be very complicated. Thus, to make a macromechanical analysis, a lamina is assumed to be homogeneous. Also, average properties for lamina are accepted.

2.4.1 Hooke’s Law for Isotropic Materials

Isotropic materials mean that the materials properties are same for all directions. The stiffness matrix comprise of E, G, K, ν . In addition, two of these constants are dependent on each other two.

$$G = \frac{E}{2(1+\nu)} \tag{2.1}$$

$$K = \frac{E}{3(1-2\nu)} \quad (2.2)$$

For anisotropic materials the general stress-strain relationship for 3-D body for Cartesian coordinate system is given in Figure 8.

$$\begin{bmatrix} \sigma_1 \\ \sigma_2 \\ \sigma_3 \\ \tau_{23} \\ \tau_{31} \\ \tau_{12} \end{bmatrix} = \begin{bmatrix} C_{11} & C_{12} & C_{13} & C_{14} & C_{15} & C_{16} \\ C_{21} & C_{22} & C_{23} & C_{24} & C_{25} & C_{26} \\ C_{31} & C_{32} & C_{33} & C_{34} & C_{35} & C_{36} \\ C_{41} & C_{42} & C_{43} & C_{44} & C_{45} & C_{46} \\ C_{51} & C_{52} & C_{53} & C_{54} & C_{55} & C_{56} \\ C_{61} & C_{62} & C_{63} & C_{64} & C_{65} & C_{66} \end{bmatrix} \begin{bmatrix} \varepsilon_{11} \\ \varepsilon_{22} \\ \varepsilon_{33} \\ \gamma_{23} \\ \gamma_{31} \\ \gamma_{12} \end{bmatrix}$$

$$\begin{bmatrix} \varepsilon_{11} \\ \varepsilon_{22} \\ \varepsilon_{33} \\ \gamma_{23} \\ \gamma_{31} \\ \gamma_{12} \end{bmatrix} = \begin{bmatrix} S_{11} & S_{12} & S_{13} & S_{14} & S_{15} & S_{16} \\ S_{21} & S_{22} & S_{23} & S_{24} & S_{25} & S_{26} \\ S_{31} & S_{32} & S_{33} & S_{34} & S_{35} & S_{36} \\ S_{41} & S_{42} & S_{43} & S_{44} & S_{45} & S_{46} \\ S_{51} & S_{52} & S_{53} & S_{54} & S_{55} & S_{56} \\ S_{61} & S_{62} & S_{63} & S_{64} & S_{65} & S_{66} \end{bmatrix} \begin{bmatrix} \sigma_1 \\ \sigma_2 \\ \sigma_3 \\ \tau_{23} \\ \tau_{31} \\ \tau_{12} \end{bmatrix}$$

Figure 8: Stiffness Matrix (C) and Compliance Matrix (S) for Anisotropic Materials [29]

$$S_{11} = \frac{1}{E} = S_{22} = S_{33} \quad (2.3)$$

$$S_{12} = -\frac{\nu}{E} = S_{13} = S_{21} = S_{23} = S_{31} = S_{32} \quad (2.4)$$

$$S_{44} = \frac{1}{G} = S_{55} = S_{66} \quad (2.5)$$

For isotropic materials, due the principals of symmetry:

$$C_{11} = C_{22}, \quad (2.6)$$

$$C_{12} = C_{23}, \quad (2.7)$$

$$C_{66} = \frac{C_{22} - C_{23}}{2} = \frac{C_{11} - C_{12}}{2} \quad (2.8)$$

Thus, stiffness matrix and compliance matrix for isotropic material reduces to the forms that are presented in Figure 9.

$$[C] = \begin{bmatrix} C_{11} & C_{12} & C_{13} & 0 & 0 & 0 \\ C_{21} & C_{22} & C_{23} & 0 & 0 & 0 \\ C_{31} & C_{32} & C_{33} & 0 & 0 & 0 \\ 0 & 0 & 0 & \frac{C_{11}-C_{12}}{2} & 0 & 0 \\ 0 & 0 & 0 & 0 & \frac{C_{11}-C_{12}}{2} & 0 \\ 0 & 0 & 0 & 0 & 0 & \frac{C_{11}-C_{12}}{2} \end{bmatrix}$$

$$[S] = \begin{bmatrix} S_{11} & S_{12} & S_{13} & 0 & 0 & 0 \\ S_{21} & S_{22} & S_{23} & 0 & 0 & 0 \\ S_{31} & S_{32} & S_{33} & 0 & 0 & 0 \\ 0 & 0 & 0 & \frac{S_{11}-S_{12}}{2} & 0 & 0 \\ 0 & 0 & 0 & 0 & \frac{S_{11}-S_{12}}{2} & 0 \\ 0 & 0 & 0 & 0 & 0 & \frac{S_{11}-S_{12}}{2} \end{bmatrix}$$

Figure 9: Stiffness Matrix (C) and Compliance Matrix (S) for Isotropic Materials [29]

2.4.2 Hooke's Law for Orthotropic Materials

For orthotropic materials' planes are symmetric in a way that all of them are perpendicular to each other which creates nine independent elastic constants. With these constants at hand, the stiffness matrix and compliance matrix for orthotropic materials are reduced to the form that are presented in Figure 10.

$$[C] = \begin{bmatrix} C_{11} & C_{12} & C_{13} & 0 & 0 & 0 \\ C_{21} & C_{22} & C_{23} & 0 & 0 & 0 \\ C_{31} & C_{32} & C_{33} & 0 & 0 & 0 \\ 0 & 0 & 0 & C_{44} & 0 & 0 \\ 0 & 0 & 0 & 0 & C_{55} & 0 \\ 0 & 0 & 0 & 0 & 0 & C_{66} \end{bmatrix}$$

$$[S] = \begin{bmatrix} S_{11} & S_{12} & S_{13} & 0 & 0 & 0 \\ S_{21} & S_{22} & S_{23} & 0 & 0 & 0 \\ S_{31} & S_{32} & S_{33} & 0 & 0 & 0 \\ 0 & 0 & 0 & S_{44} & 0 & 0 \\ 0 & 0 & 0 & 0 & S_{55} & 0 \\ 0 & 0 & 0 & 0 & 0 & S_{66} \end{bmatrix}$$

Figure 10: Stiffness Matrix (C) and Compliance Matrix (S) for Isotropic Materials [29]

2.5. Macromechanical Analysis for Laminate

The stress-strain relations for single lamina are presented in section 2.4. To achieve laminate structure, laminae need to be stacked together in the thickness direction. The first reason for the stacking operation is, not failing under realistic loads. The second one is, enhancing the mechanical properties in transverse direction. On the other hand, the laminates should be stacked with different layer angles in order to compensate complex

loading and stiffness requirements. Since too many laminates would increase the cost the optimum amount and ply angles should be considered. The strength and stiffness and hygrothermal properties of the laminate depends on elastic moduli, stacking position, thickness, angle of orientation, coefficient of thermal expansion and coefficient of moisture expansion. In order to facilitate the analysis, some assumption will be done neglecting some of these parameters. So, only the parameters that will be used in the FEA will be covered afterwards.

2.5.1 Stacking Position

As previously mentioned, single layers are bonded through thickness direction. To identify a layer some parameter has to be known. These parameters are location, material and angle of orientation. An example drawing of a laminate is presented in Figure 11.

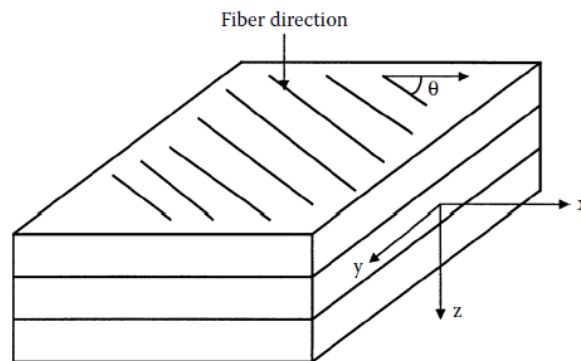


Figure 11: A Drawing of a Laminate [29]

Each lamina is represented by angle of ply and separated by each other with a slash sign. The sequence of the plies goes from top to the bottom. Some special notations can be used. Some examples are provided below:

$[0/-45/90/60/30]$ is the code for a laminate that involves five plies. Each ply has different angles to reference x-axis. It also shows plies are of same material and with same thickness. The laminate can also be showed with $[0/-45/90/60/30]_T$. Here subscript show “total laminate”.

Another example is presented to show how the symmetry in the laminates are. If we examine the $[0/-45/60]_s$ laminate, it involves six piles with $[0/-45/60/60/-45/0]$ configuration.

It can be interpreted that, the material orientation, material and thickness are same which makes the laminate symmetric. So. “s” written as subscript denotes written plies are repeated in reverse order.

2.5.2 The Relations for Stress and Strain

Before driving the equations for stress and strain for laminates, “Lamination Theory” should be presented. This theory has four basic assumptions that are:

- Laminate is thin and wide (can be interpreted as its width is much more than the thickness)
- Many of the laminas has perfect interlaminar bonds between them
- Strain distribution for transverse direction is laminar
- All laminas are macroscopically homogeneous, and they all show linearly elastic behavior

A laminate geometry is presented in Figure 12. Referring to strain distribution in the thickness direction being laminar, the equation below can be derived:

$$\epsilon_{xx} = \epsilon_{xx}^{\circ} + zk_{xx} \tag{2.9}$$

$$\epsilon_{yy} = \epsilon_{yy}^{\circ} + zk_{yy} \tag{2.10}$$

$$\gamma_{xy} = \gamma_{xy}^{\circ} + zk_{xy} \tag{2.11}$$

Where z denotes the distance from the midplane in the thickness direction

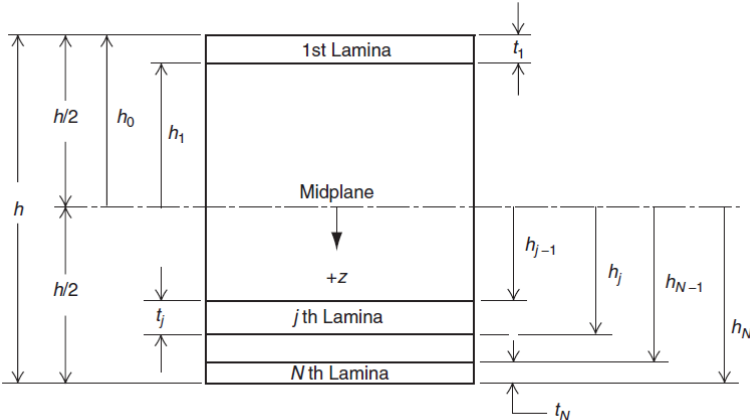


Figure 12: A Laminate Geometry [23]

2.5.3 The Relations for Forces and Moments in the Laminates

A schematic for the laminate resultant forces and moments acting on a laminate is given in Figure 13. These resultant forces and moments are related to the strains and curvatures by the equations below:

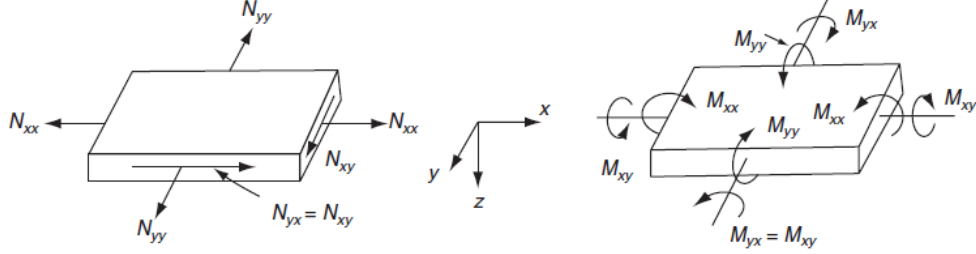


Figure 13: Schematic for the Laminate Resultant Forces and Moments Acting on a Laminate [23]

$$\begin{Bmatrix} N_{xx} \\ N_{yy} \\ N_{xy} \end{Bmatrix} = [A] \begin{Bmatrix} \varepsilon_{xx} \\ \varepsilon_{yy} \\ \gamma_{xy} \end{Bmatrix} + [B] \begin{Bmatrix} k_{xx} \\ k_{yy} \\ k_{xy} \end{Bmatrix} \quad (2.12)$$

and

$$\begin{Bmatrix} M_{xx} \\ M_{yy} \\ M_{xy} \end{Bmatrix} = [B] \begin{Bmatrix} \varepsilon_{xx} \\ \varepsilon_{yy} \\ \gamma_{xy} \end{Bmatrix} + [D] \begin{Bmatrix} k_{xx} \\ k_{yy} \\ k_{xy} \end{Bmatrix} \quad (2.13)$$

The elements in the matrix [A], [B] and [C] are calculated from the equation below:

$$A_{mn} = \sum_{j=1}^n (\bar{Q}_{mn})_j (h_j - h_{j-1}) \quad (2.14)$$

$$B_{mn} = \frac{1}{2} \sum_{j=1}^n (\bar{Q}_{mn})_j (h_j^2 - h_{j-1}^2) \quad (2.15)$$

$$D_{mn} = \frac{1}{2} \sum_{j=1}^n (\bar{Q}_{mn})_j (h_j^3 - h_{j-1}^3) \quad (2.16)$$

Here, n denotes the total number of laminas.

3. MICROVASCULAR CHANNELS IN COMPOSITE MATERIALS

3.1. Area of Utilization

As mentioned in the previous chapters, from defense industry, aerospace etc. the composite materials are frequently utilized. To enhance capabilities of composites various studies have been going on. [30]–[32] In recent years, functionalizing the composite materials via implementations of optical fibers [1], [33], using shape memory polymers and its alloys [4], [5], [34] incorporation of piezoelectric materials and sensors [35], [3], using nanoparticles have been studying [6], [7], [36]. In addition to these implementations, to augment utilization and functionality of the composite materials, several studies have been done in this field recently. One way to increase the functionality is, introducing fluid into the microchannel. The fluid in the microchannel can be selected to according to the aim to be achieved. Functionalities previously mentioned, may be sorted as self-healing [8]–[13], active cooling [14], [15] and better damage visibility [16], [17] and sensing [18], [19].

3.2. Manufacturing

There are three main manufacturing methods to obtain microvascular channels in composites, which are vaporization of sacrificial components, removable solid cores and non-removable hollow cores.

3.2.1 Vaporization of Sacrificial Components

VaSC in short, is commonly used for 3D woven materials. In this manufacturing process, portion of the fiber tows that are in the woven preform, are replaced by catalyst-impregnated polylactide acid (PLA) sacrificial fibers. Then the impregnated preforms infiltrates epoxy. During heating, sacrificial fibers evaporates and evacuates to form hollow microchannels. The advantages of this manufacturing method are, offering different size, shape and microvascular structures, providing smoothness at the surfaces and providing good control on size of the microvascular channel that is aimed. On the other hand, the disadvantage of this method is, needing operator skill to form the microvascular channels and also the requirement for the high temperature resin. The diameter of the microchannel that can be obtained with this method has a range of 20 μm to 500 μm .

The microchannels that are produced by this method can be used for active-cooling, biotechnology, micro-electro-mechanical systems, chemical reactors [37]–[47].

3.2.2 Removable Solid Cores

In this process, metal or polymer removable cores positioned on dry fabric layers. Then, resin curing and permeation are done to form laminate. After removing the cores, the hollow channels are obtained. The microchannel diameter can vary for wires made of different materials. For instance, for straight non-woven polymer wire is used, the diameter ranges from 280 μm to 1.2 mm and if metallic wire is used the range varies between 80 μm to 710 μm . The advantage of this method is, reduction the effects of the microchannel to improve mechanical strength. A disadvantage for this method is, not being suitable for thermal applications. Another one is being limited to straight channels. This method of production can be used only for self-healing as of now. [20], [48]–[55]

3.2.3 Non-Removable Hollow Cores

In this method, a metal bundle, glass, polymer hollow tubes can be used. These materials can be introduced center of the fabric layers. During the curing, these tubes works as microchannels. The most common non-removable hollow cores are hollow glass tubes (HGT) and hollow glass fibers (HGF).

3.2.3.1 Hollow Glass Tubes

The hollow glass tubes' diameters range between 0.3 mm to 3 mm. The benefits of HGTs are being compatible with various composite types, easy positioning, obtaining smooth surfaces and higher structural strength. Respect to these advantages some researchers use this type of microchannels. [56]–[62]. The disadvantages of this process are reducing the mechanical properties of the composite when applying a large tube dimension. Also, similar to solid cores, only straight alignment can be used and not convenient for heat transfer applications. These tubes can be used for self-sensing and self-healing applications.

3.2.3.2 Hollow Glass Fibers

The hollow glass tubes' diameters range between 5 μm to 60 μm . The advantages of this method are: enabling the utilization in woven laminates, being compatible to most of the composites, effecting the mechanical properties less. The disadvantages of this methods are like hollow glass tubes: being limited to size and shape of microchannels, not being convenient for heat transfer applications. Hollow glass tubes used composites are most commonly used for better visuals for internal damage applications and self-healing. [63]–[66]

3.2.4 Manufacturing of Sample Specimen

The analyses were performed for cross-ply glass-fiber composites with two configurations, $[0/90]_{3s}$ and $[90/0]_{3s}$. 12 plies for both configurations are prepared with glass fabric of areal weight, 350 gr/m^2 . The thickness of each ply was 4.5 mm. Taking the density of glass as 2.5 gr/cm^3 , the fiber volume fraction was calculated as approximately 37%. The diameter of micro-channel to be manufactured was determined as 1 mm based on the maximum channel diameter with respect to the laminate thickness suggested in order not to encounter manufacturing issues.

The specimens were manufactured via removable solid wires technique. First, fabrics were cut and placed in an aluminum mold. The specimen length is 280mm, height is 205 mm and thickness is 4 mm. As for solid steel wires the diameter is 1 mm and the length is 290 mm. Four solid steel wires are used to introduce the microvascular channel to the laminae.

Wires were coated with a thin layer of mold release and then located in the middle layer with the distance of 50 mm from one another. In order not to have any axial runout, the both ends of the wire is attached tightly to the mold surface. After the mold is closed, epoxy resin were introduced to the mold by VARTM. The epoxy's properties and curing cycles are given in Figure 14.

Epoxy composition	Curing Temperature	Curing Time
Aradur 564: Araldite 2954, 100:37 wt.%, Huntsman	80 °C	1 hour
	160 °C	4 hours

Figure 14: Epoxy Composition and Curing Information

Following the cure, solid cores (wires) were pulled out and then composite plate was trimmed around the edges. Finally, the specimens were cut to the dimensions suitable for micro CT scanning (10 mm × 4 mm).

3.3. Mechanical Behavior

Since being inserted into composite laminates, the microvascular channels create stress concentration fields. For this reason, this application effects the mechanical strength of the structure. Inserting a HGT into the laminates, creates resin rich pockets/regions. In this region, ply undulations occurs and volume fractions increases as a natural consequence. To analyze the effects of microchannels on the composite structure, the composite structure with HGT is researched and it is found that the microchannels effect the compression and tension moduli, tension and compression strength, fiber volume content inside the structure. [66]

There are numerous tensile, compression, impact, fatigue short beam shear and cantilever beam tests are done. [1], [2], [30], [35], [56], [67], [68] Coppola et al, found that for GFRP with microchannels created VasC method, for in plain and tensile moduli are less than 10% for longitudinal and transverse tensile load. Huang et al. [20] researched the influence of microchannels applied to CFRP composites. The obtained results show a reduction in compression strength 13% to 70 % varying according to the diameter of the microchannels. The main cause of this reduction in compression strength is fiber waviness and resin rich regions.

4. FINITE ELEMENT ANALYSIS OF VASCULARIZED LAMINATE

It is found out that various researchers used FEM to study the effects of microchannels for the structures of composite materials. And among the researchers some of them used plane strain model [20] and orthogonal stacking configuration [69].

Huang et al.[20], researched a FEA for crack initiation and failure under load. Instead of using whole length, just a quarter of the geometry is used due to geometric symmetry. The meshing areas are divided into zones. Each zones has different mesh density. Plain strain model is assumed. The dimensions are specified in a parametric manner to make the comparison of the results easier. The curing effect is also introduced to the FEA. First, the curing stresses and then the mechanical loads are analyzed. Three different number of elements and nodes are tried and the optimum element and node number are assigned for the model. Results obtained by the FEA is validated through mechanical testing with high-speed photography [20].

Soghрати et al, used a method called IGFEM to model and design for actively cooled microvascular specimen to minimize the temperature in the thermal fin, to optimize the flow efficiency in the microchannel [40].

Hartl et al. [70], researched parallel and periodic microchannels. The impacts of channel orientation, spacing and cross-sectional aspect ratio of channel are quantified for laminate sequence for the aerospace structures that are commonly used. The primary aim of the study is guiding the design of composite with microvascular channels by based on this analysis. A general Representative Volume Element is analyzed with FEA for damage approach.

Al-Shawk et al. [21], studied about GFRP composite materials with microvascular channels to investigate stress concentration and failure behavior around resin rich region. Different stacking configuration and vasculature sizes are used in the study. The most noticeable change observed is in UD 0 stacking configuration for changing microchannel diameter. The elliptical channels are also studied and the effect of this parameter

comparing to the circular ones results in reducing the stress concentrations. Stacking configuration effects the failure in the resin pocket rather than the area around laminates.

Khargani et al. [71] studied the behavior of the butt-joints under 3-Point Bending. The joints are made of steel and GFRP. Bolted and non-bolted joint connections are used. Numerical calculations and experiments are done within the study. Strain gauges are used to measure deflection and strain values. These values are also numerically calculated. 3D FEM analysis is done via ANSYS software. Within numerical analysis, the input for the 3-point bending is specified. For steel, maximum first principal stress theory is used to determine the failure. However, it is also stated that maximum normal stress or von-Mises may be the other options for stress theory. Relation of load vs displacement and load vs strain are sorted. The maximum strain value obtained is 0.47%. It is found that bolted connections does not give too much effect on capacity and stiffness to the joint as a result. [71]

Fan et al., [72] researched through static and fatigue aspects of 3D orthogonal Carbon/Glass fiber hybrid composites. Two different hybrid composites are used, 3D orthogonal and laminated ones. Failure and fracture propagation are observed via 3D microscope. It is found that 3D orthogonal model shown better results comparing to the laminated one. The main reason for this is 3D orthogonal one has threads in z-direction (direction of the applied load). 3-point bending tests are done to analyze static test and fatigue test. After the tests, images of fractures are captured by 3D microscope. [72]

Wu et al. [73] reserached the fatigue response of 3D braided composite under three-point low cyclic bending. An FEM model is created (via CATIA software) to analyze (ABAQUS software) bending fatigue behavior deformation and failure. To capture the essence of the failure, stress distributions, stress hysteresis failure of the fibers and resins among the composite are observed. Within the FEA, fiber yarns roller and these yarns are hexahedral and since the resin has irregular curves tetrahedral elements are used. Different mesh sizes are tried and mesh size is optimized. In addition, surface to surface contact model is used. Tie contact is used between the support roller and resin. Master surface is chosen as fiber that contacts the resin and slave surface is chosen as resin. The supporting rollers are chosen as rigid bodies without DOF. It is found out that yarns at the surface burden more load comparing to the inner ones. It is implied that crack forming

and fatigue damages starts at early stages within the composite and afterwards this leads to crack propagation. Finally, Wu et al, states that by changing the fiber tows orientation angles, the mechanical properties of this type of composites may be enhanced even more. [73]

Jia et al, [74] investigated the deformation and damage aspects of 3D orthogonal woven composite materials. Composite is subjected to the 3-point bending analysis that is analyzed via FEA. Crack failure modes and longitudinal and transverse ultimate strength of the materials are obtained. Beam's responses under 3-point bending, damage initiation and propagation values are obtained. Afterwards, these values are compared with the experimental ones. It is assumed that materials have maximum principal stress failure. Micro, meso and macro scale analysis are done by different element sizes with C3D8 elements. 3-point bending analysis macro-scale cells are used. It is stated that, with the obtained FEM may further developed to make deformation and damage analysis that can be used in textile composites. [74]

4.1. About the Model

In this chapter, the models that are developed for the thesis are introduced. Huang et al. [20]'s model is selected as reference due its similarity in configuration for validation purposes. Huang et al. [20]'s model is re-drawn both with 2-D and 3-D geometry with an assumed width and same loadings and all other configuration as kept same. After obtaining the 2-D and 3-D analysis results, 3-D model approach is considered. The reason to choose the final geometry as 3-D instead of 2-D is, with 2-D geometry different angles for laminates cannot be studied and with 3-D model it is more flexible to study the loading cases such as bending [21]. After validating the model, the model is generated with different dimensions and loading. The model's material properties are obtained from the sampled that is produced, tested in UTAA's Laboratory and the analysis are made on this model are presented accordingly.

4.1.1. Finite Element Model Development of the Validation Model

4.1.1.1. Defining the Geometry

Huang et. al. [20] selected the vasculature diameter as 80 μm , 150 μm , 200 μm , 310 μm , 400 μm , 560 μm and 710 μm . In order to have a result that is compliant with the test results,

400 μm circular vascule are presented. According to Huang et. al. [20]'s study, there are four important feature that effects stress, Resin pocket length (L_{RP}), fiber disturbance angle (θ_d), fiber disturbance height (h_d) and resin pocket are (A). A schematic the geometrical parameters are presented in Figure 15.

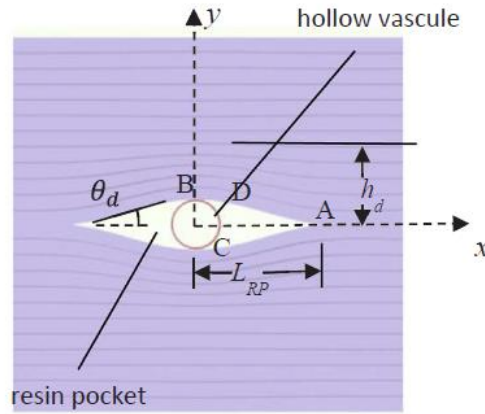


Figure 15: Schematic for Geometrical Parameters [21]

The model and load that applied to the model are symmetric. Due this, instead of analyzing the whole model, which will consume computational time, just the quarter is modelled that can be seen in Figure 16.

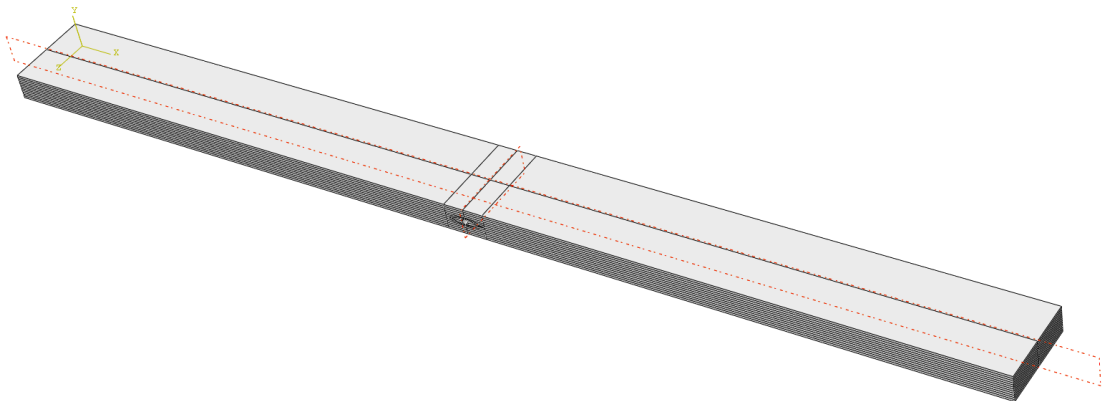


Figure 16: Cutting Planes of the 3D Validation Model

Instead of using specimen length Huang et al. assumed the model length as $50r$.

Into the length, thickness, length of resin pocket (L_{RP}), disturbance height is depends on vascule diameter (r). The calculations for this parametric value are given below:

The vascule diameter = $400\mu\text{m}$ ($2*r$)

Length = $X = 50 \times r = 10 \text{ mm}$ (due to symmetry, $x = 5 \text{ mm}$)

Thickness = $y = 3 \text{ mm}$ (due to symmetry, $y = 1.5 \text{ mm}$)

$$L_{RP} = 5.08 \times r = 5.08 \times 0.2 \text{ mm} = 1.016 \text{ mm}$$

$$h_d = 3.71 \times r = 3.71 \times 0.2 \text{ mm} = 0.742 \text{ mm}$$

$$\text{Lamina thickness} = 3 \text{ mm} \div 24 = 0.125 \text{ mm}$$

Since Huang et. al. [20] have researched a 2-D plain strain model, there is no width value.

Therefore a width with 4 mm is assumed similar to study done by Al-Shawk et al. [21].

4.1.1.2. Defining the Materials

The materials and elastic and thermal material properties of Huang et al. [20]'s study are given in Table 1.

Table 1: The Elastic and Thermal Properties of IM7/8552 Composite Laminates and Hexcel 8552 Neat Epoxy [20]

Material Properties of IM7/8552 Composite Laminates & Hexcel 8552 Neat Epoxy	
IM7/8552 elastic properties	
E_{11T}	165 GPa
E_{11C}	145 GPa
E_{22T}	11.38 GPa
E_{22C}	10.20 GPa
E_{33T}	11.38 GPa
E_{33C}	10.20 GPa
G_{12}	5.12 GPa
G_{23}	5.12 GPa
G_{13}	3.92 GPa
ν_{12}	0.3
ν_{23}	0.487
ν_{13}	0.3
Hexcel 8552 neat epoxy elastic properties	
E	4.67 GPa
ν_{12}	0.35
IM7/8552 thermal properties	
α_{11}	$6 \times 10^{-7} \text{ K}^{-1}$
α_{22}	$2.86 \times 10^{-5} \text{ K}^{-1}$
α_{33}	$2.86 \times 10^{-5} \text{ K}^{-1}$
α (neat resin)	$5.0 \times 10^{-5} \text{ K}^{-1}$

4.1.1.3. Defining the Boundary Conditions and Load

Symmetric boundary conditions are assumed for x (y-z plane) and y (x-z plane) directions. The pressure applied, σ_0 , is 1.65 GPa, which is applied on the y-z plane at the

edge of the model. The curing effect is applied for the model. The curing temperature is selected as 150 °C and then the material is cooled down to 20 °C. The boundary conditions and load that is applied to the 2-D and 3-D models are presented in Figure 17 and Figure 18.

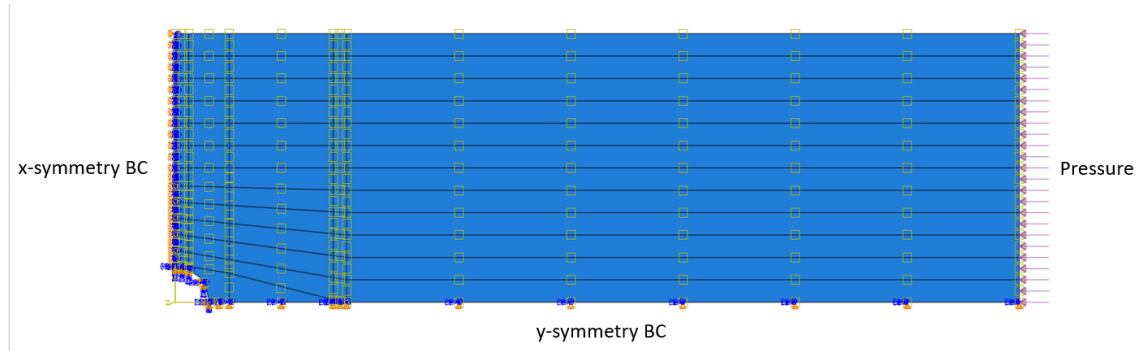


Figure 17: Boundary Conditions and Loads for 2-D Validation Model

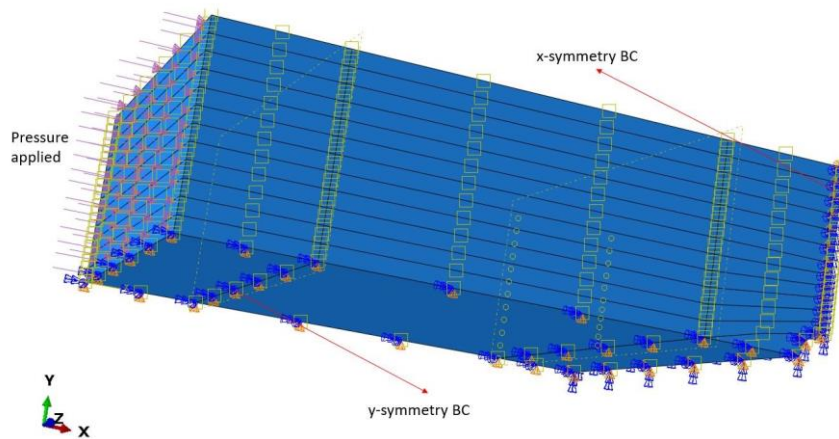


Figure 18: Boundary Conditions and Loads for 3-D Validation Model

4.1.1.4 Defining the Mesh and Element Types

In Huang et al.’s study [20] along with 2-D validation model, the mesh type that is used is “plain strain quadrilateral elements (CPE8)”. The number of elements and number of nodes that are used for these models are presented in Table 2. The validation model is however 3-D and has the 8-node linear 3D elements (C3D8) in ABAQUS/Standard. Due to be the area of interest, the region around microvascular channel is meshed more tightly as it can be seen in Figure 19 to Figure 21.

Table 2: Comparison of Number of Elements and Number of Nodes in Huang et al. [20] and 2-D Validation Model

	Number of Elements	Number of Nodes
Huang et al.	3975	12240
2-D Validation Model	4034	12423

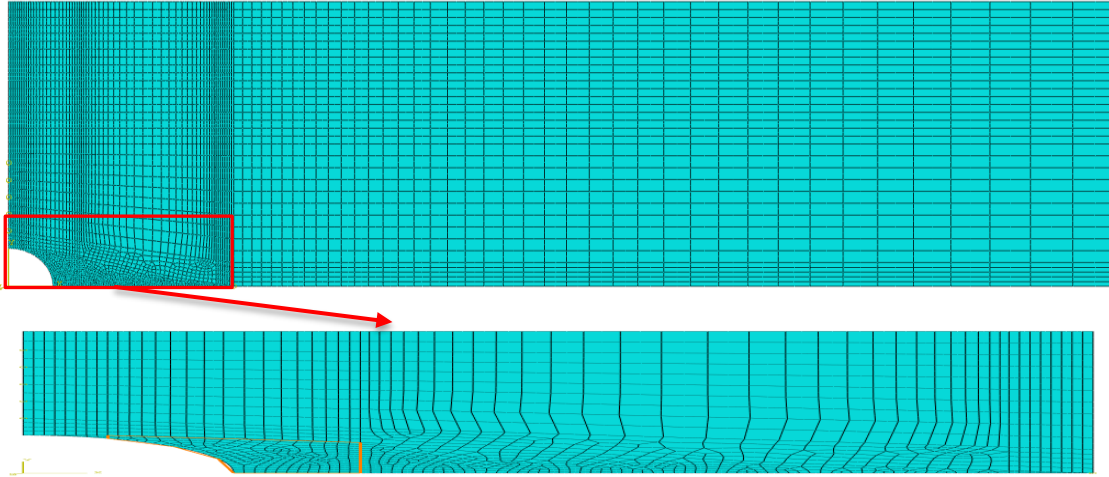


Figure 19: A Display for the Resin Rich Portion of the 2-D Validation Model

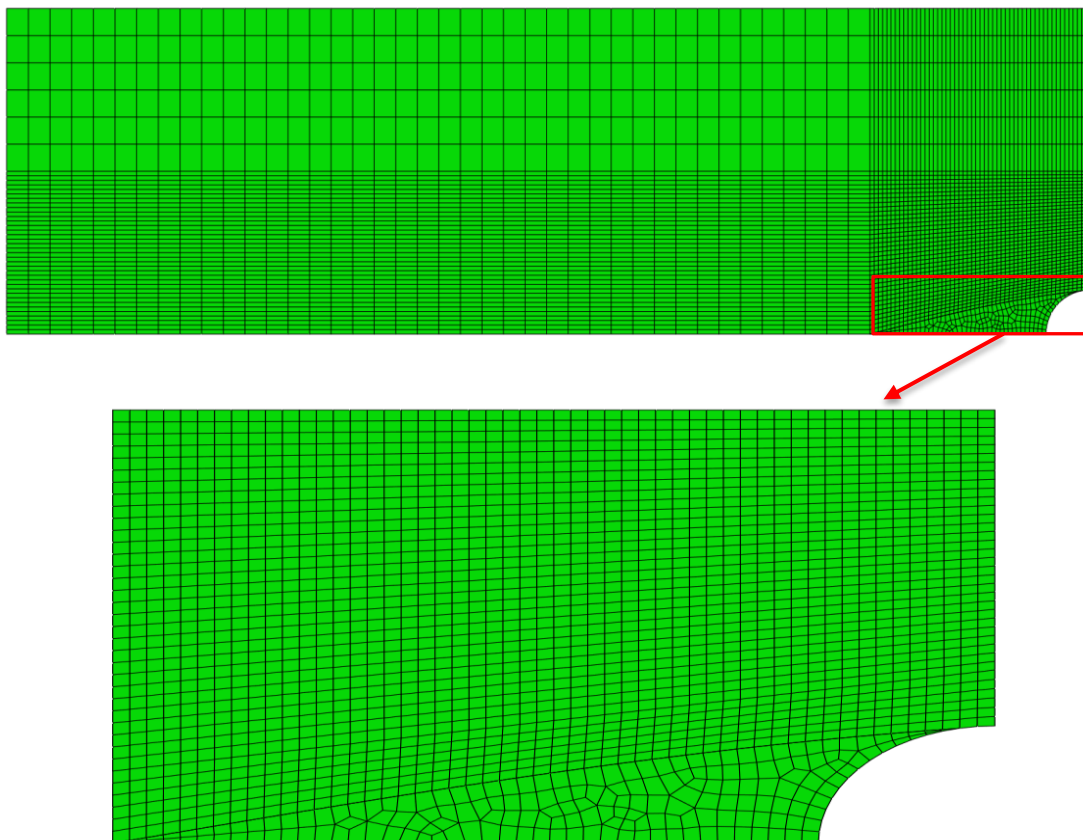


Figure 20: A Display for the Resin Rich Portion of the 3-D Validation Model

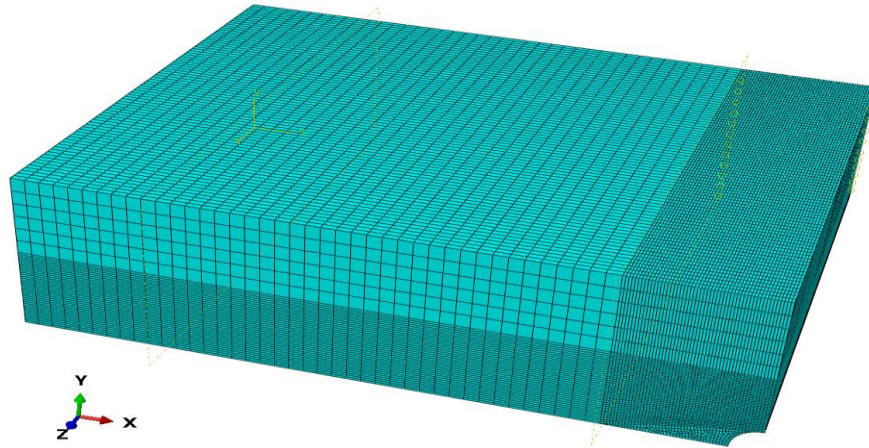


Figure 21: A Display for the Mesh of the 3D Validation Model

4.1.2. Finite Element Model Development of the Present Model

As explained in the section 3.2.4, prepared specimens are to be analyzed via FEM under transverse tension, compression load and bending loads are investigated.

4.1.2.1 Defining the Geometry

Two samples are prepared in the stacking sequence of $[0/90]_{3s}$ and $[90/0]_{3s}$. Micro-CT analysis was used to investigate the internal architecture of the laminates. Then the required dimensions for generating the model were captured through these images. The micro-images that are taking via micro-CT is given in Figure 22. As it can be clearly seen, the area of resin-rich pocket in $[0/90]_{3s}$ stacking configuration has much more comparing to $[90/0]_{3s}$ configuration. Similar outcomes are also obtained by [21], [51], [69]. Comparing to the studies in the literature, similar waviness trends are also obtained. [20], [21], [58]. The dimensions for present model is presented in Figure 23. The width is 20 mm.

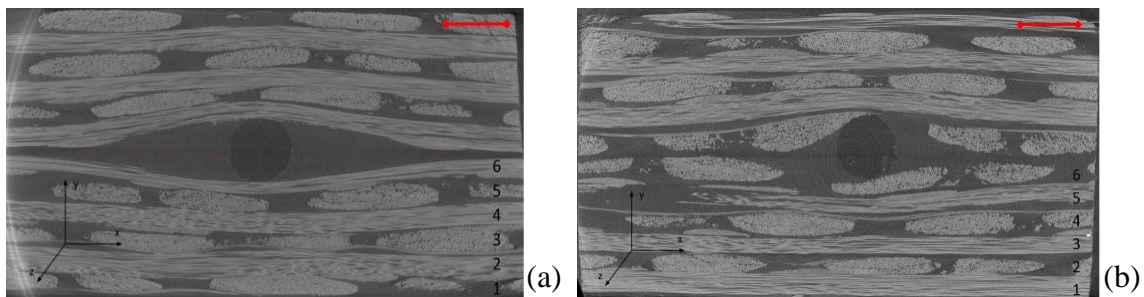


Figure 22: Micro-pictures of GFRP samples with 1 mm diameter for: a) $[0/90]_{3s}$ and b) $[90/0]_{3s}$

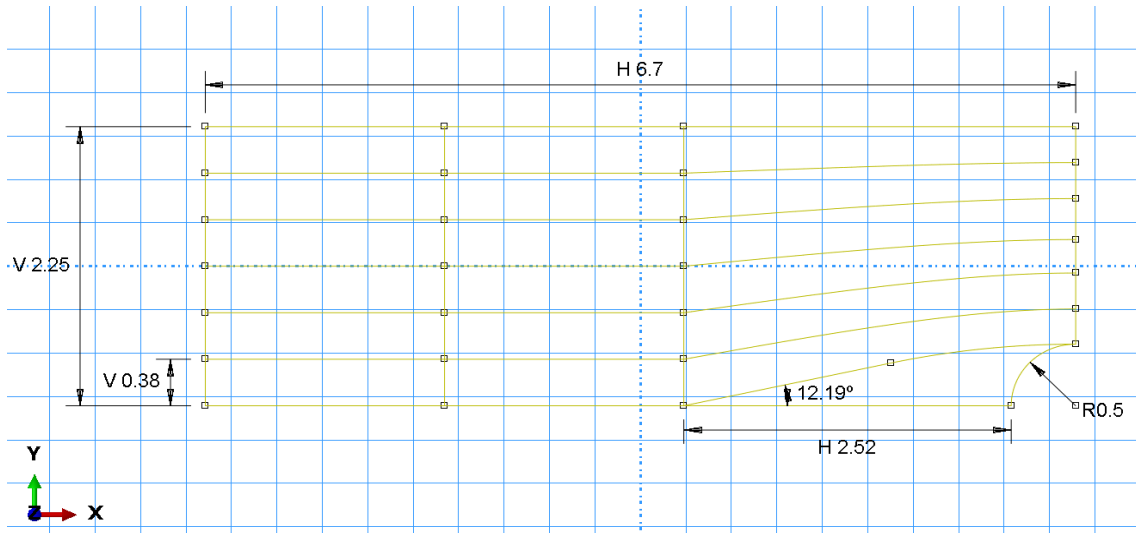


Figure 23: The Dimensions of the Present Model for Transverse Loads

As for 3-Point Bending analysis, the dimensions of the specimen differs from the transverse compression and transverse tensile analyses. The specimen dimensions are specified accordingly to D7264/D7264 M 15 Standard [75]. The specimen dimensions are presented in Figure 24. The load roller diameter 5 mm and the span length is 128 mm.

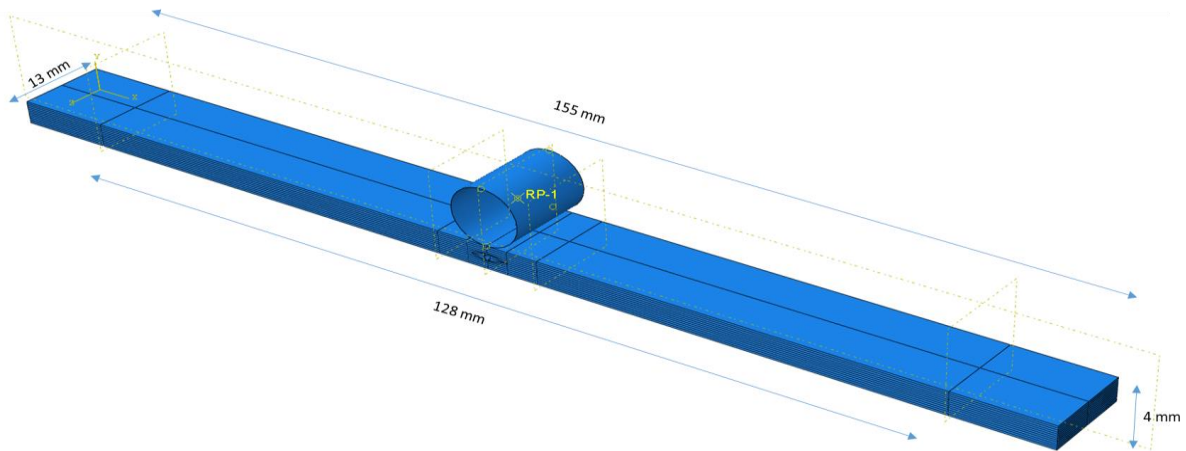


Figure 24: The Dimension of Specimen for 3-Point Bending

4.1.2.2 Defining the Materials

The material used in this study is presented in Table 3. The material properties for lamina 0 and lamina 90 are calculated via study of Tanabi et. al. [76] and presented in Table 4.

Table 3: Material properties for E-Glass fiber and Aradur-564: Araldite 2954 with 37% volume fraction

Material Properties of E-Glass fiber [25]	
E (GPa)	73.35
ν	0.22
Material Properties of Aradur-564 : Araldite 2954 [77]	
E (GPa)	2.5
ν	0.35

Table 4: The Material Properties Lamina 0 and Lamina 90 [76]

	Lamina 0	Lamina 90
E_1 (GPa)	40.9276	15.0309
E_2 (GPa)	14.7607	42.6922
E_3 (GPa)	13.3642	13.8058
ν_{12}	0.0918	0.2688
ν_{13}	0.0935	0.3078
ν_{23}	0.3429	0.2818
G_{12} (GPa)	5.0676	5.3205
G_{13} (GPa)	4.99	5.1303
G_{23} (GPa)	5.0571	5.16

4.1.2.3 Defining the Boundary Conditions and Load

For transverse loads, symmetric boundary conditions are assumed for x (y-z plane) and y (x-z plane) directions. The pressure applied, σ_0 , is 50 MPa which is applied on the y-z plane at the edge of the model. The display for boundary conditions are presented in Figure 25 to Figure 27.

For 3 Point Bending analysis, according to ASTM D7264/D7264 M-15 [75] standard, the displacement value is calculated through Maximum Strain Procedure A, assuming there is a 0.5% displacement.

$$\delta = \frac{\epsilon \cdot L^2}{6h}$$

$$L = 128 \text{ mm}$$

$$\epsilon = 0.005 \text{ (0.5\%)}$$

$$h = 4 \text{ mm}$$

$$\delta = \frac{0.005 (128\text{mm})^2}{(6)(4\text{mm})}$$

$$\delta = 3.41 \text{ mm}$$

In the above equation δ denotes deflection; L denotes sport span, ϵ maximum strain at outer surface and h denotes thickness of the beam.

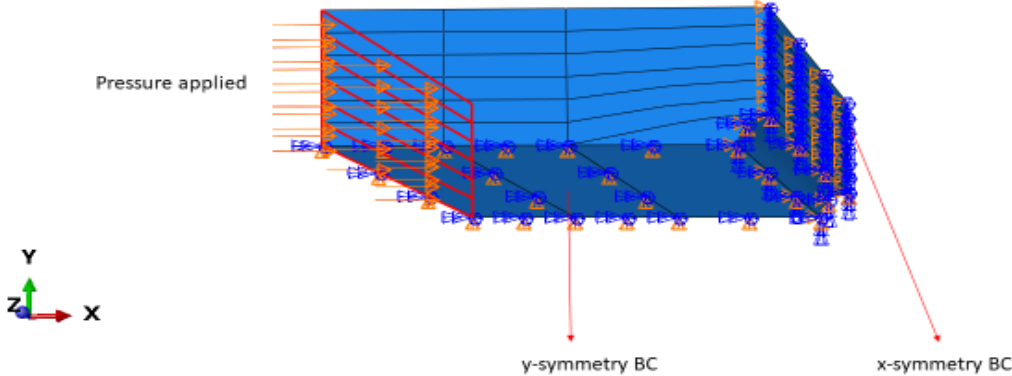


Figure 25: The Boundary Condition and Load for Present Model under Transverse Compression

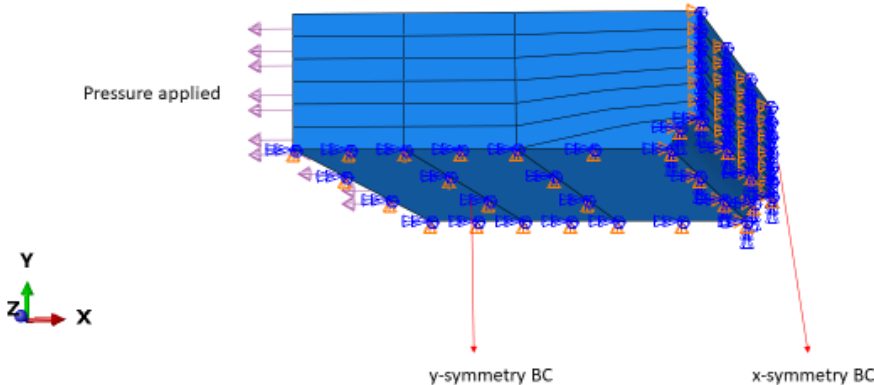


Figure 26: The Boundary Condition and Load for Present Model under Transverse Tensile

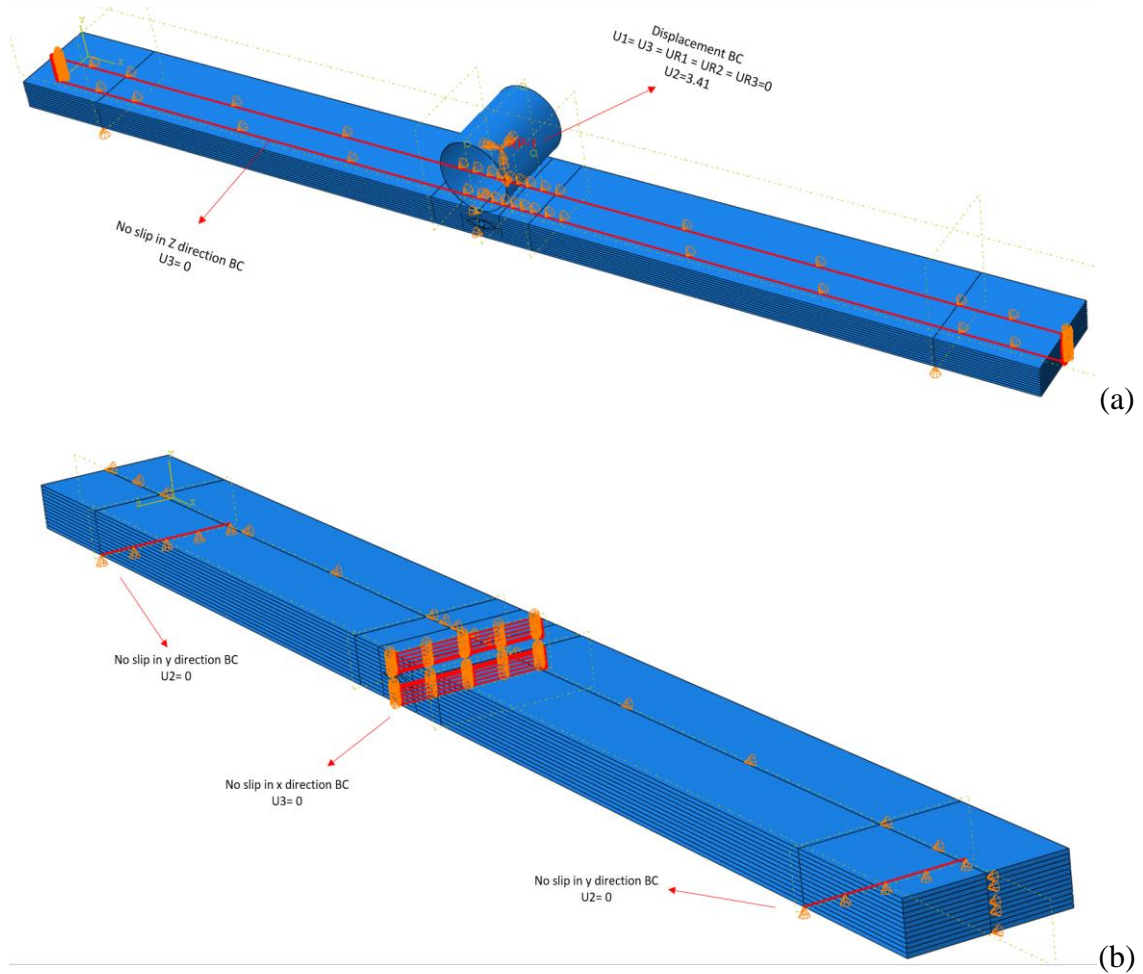


Figure 27: The Boundary Condition Present Model under 3-Point Bending a) Displacement and No slip in z-Direction BC b) No slip in x-Direction and y-Direction BC

4.1.2.3 Defining the Mesh and Element Types

The approach towards the meshing is quite similar to the validation model. The resin-pocket region is meshed more tightly comparing the other regions of the model. In order to define the number of elements for the mesh, analyses with different number of meshes are done. The number of nodes, elements and the aspect ratio effect are studied. A comparison of the number elements and number of nodes for finer meshes are presented in Table 5 and Figure 28. After this study is the mesh is assigned. The number of elements and number of nodes for the transverse loads and bending load are presented in Table 6. The mesh for the whole model and the area of interest for the present model is presented in Figure 29 to Figure 33. Mesh type that is used is for Present Model for Transverse Loads is 8-node linear 3D elements (C3D8) in ABAQUS/Standard while Present Model

for Bending Loads is 8-node linear brick and 8-node linear brick, reduced integration, hourglass control (C3D8R). Due to the complexity of the vascular area mesh type of C3D8R is used.

Table 5: Number of Elements and Number of Nodes in Present Model for Transverse Loads

Present Model under Transverse Loads	Number of Elements	Number of Nodes
Attempt 1	12768 (C3D8R)	10880
Attempt 2	33900 (C3D8R)	37968
Attempt 3	61488 (C3D8R)	55700

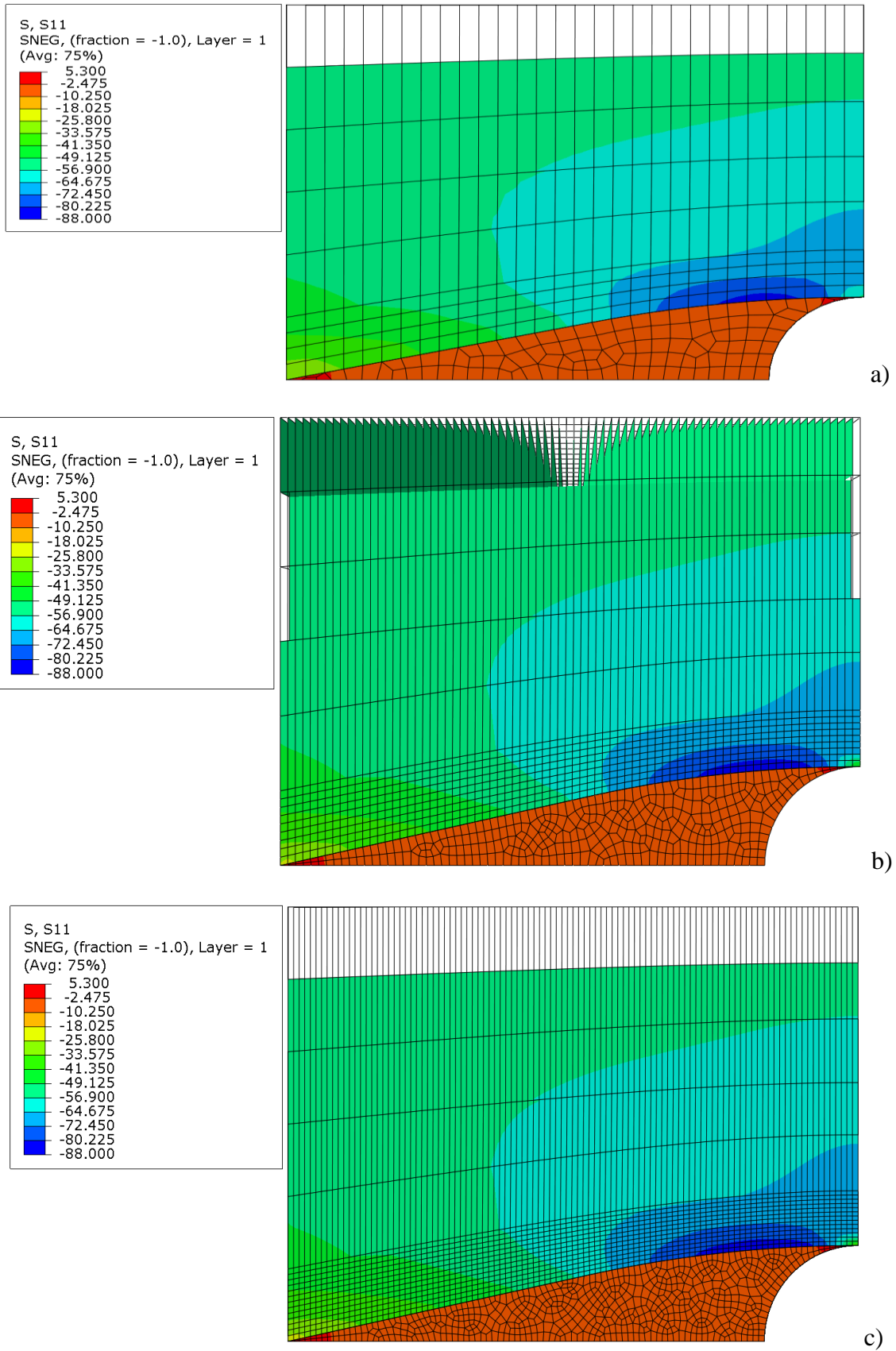


Figure 28: Comparison of S11 Contours with Different Number of Meshes for the Present Mesh in UD0 Stacking Configuration for a) Attempt 1 b) Attempt 2 c) Attempt 3

Table 6: Number of Elements and Number of Nodes in Present Model for Transverse Loads and Bending Load

Present Model	Number of Elements	Number of Nodes
Transverse Loads	33900 (C3D8R)	37968
Bending Load	601510 (C3D8R)	628800

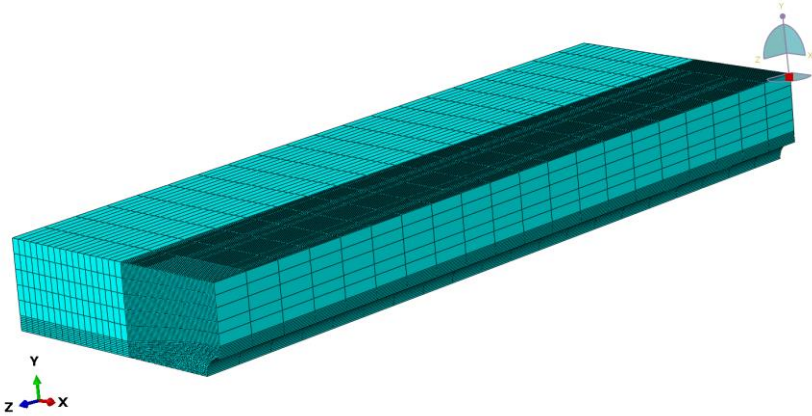


Figure 29: The Meshing of the Whole Model for the Present Model under Transverse Loads

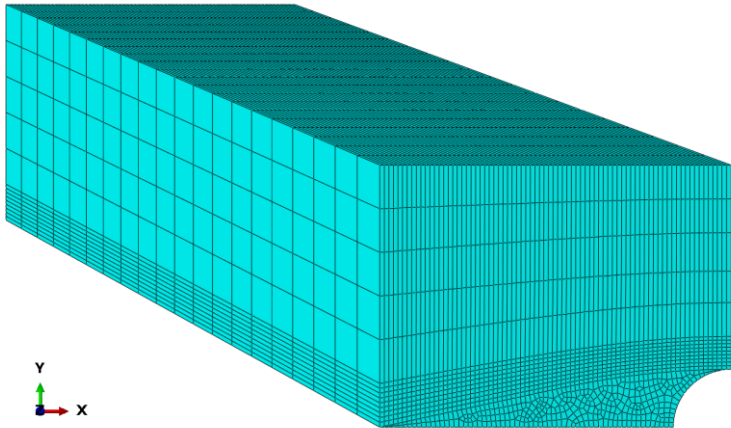


Figure 30: The Meshing of the Area of Interest for the Present Model for Transverse Loads

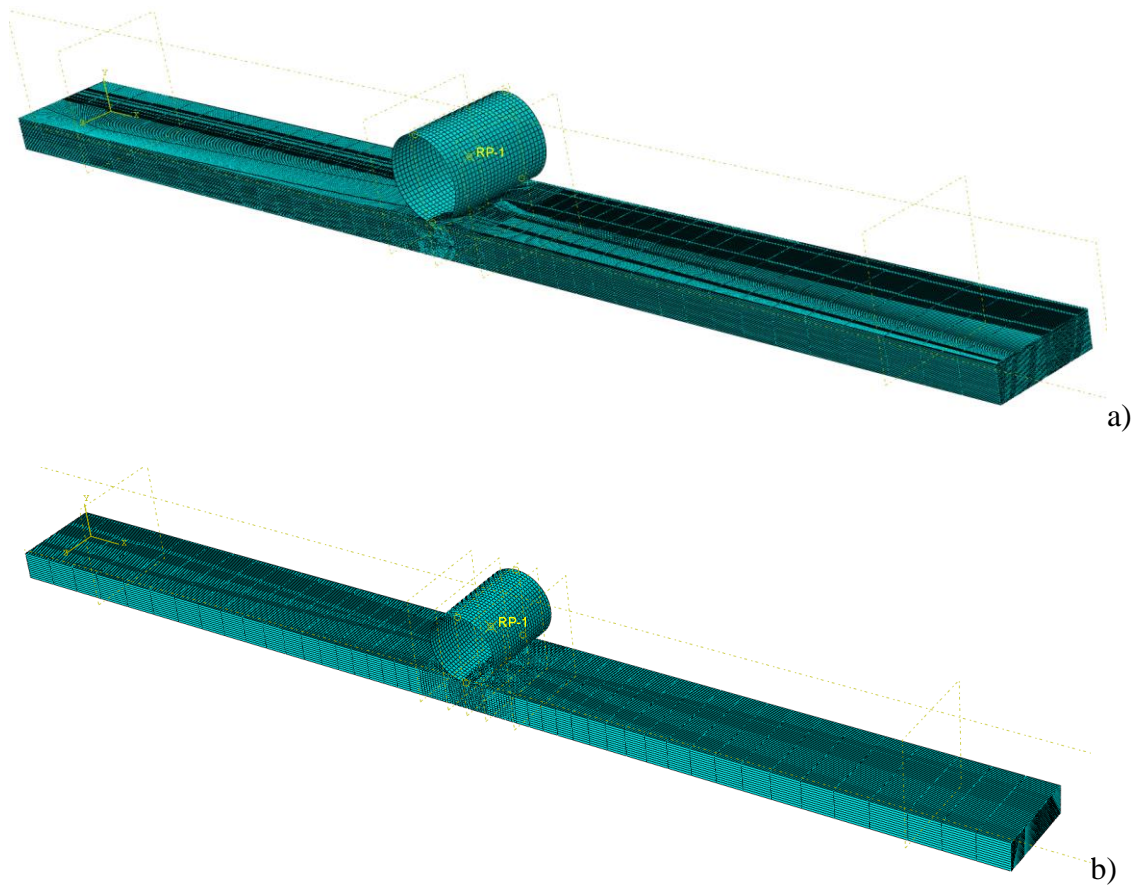


Figure 31: The Meshing of the Present Model for 3-Point Bending a) with Microchannel
b) without Microchannel

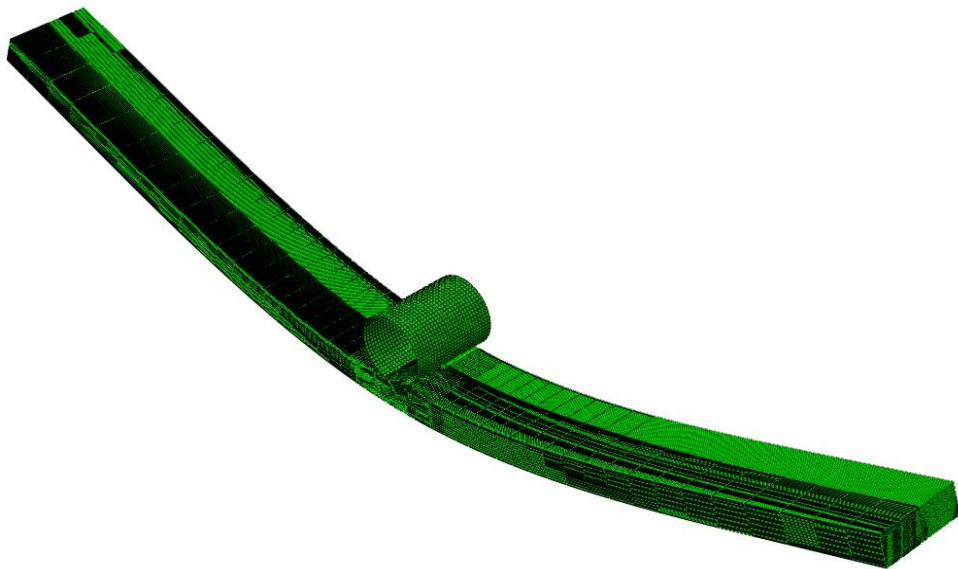


Figure 32: An Illustration of the Bent Model

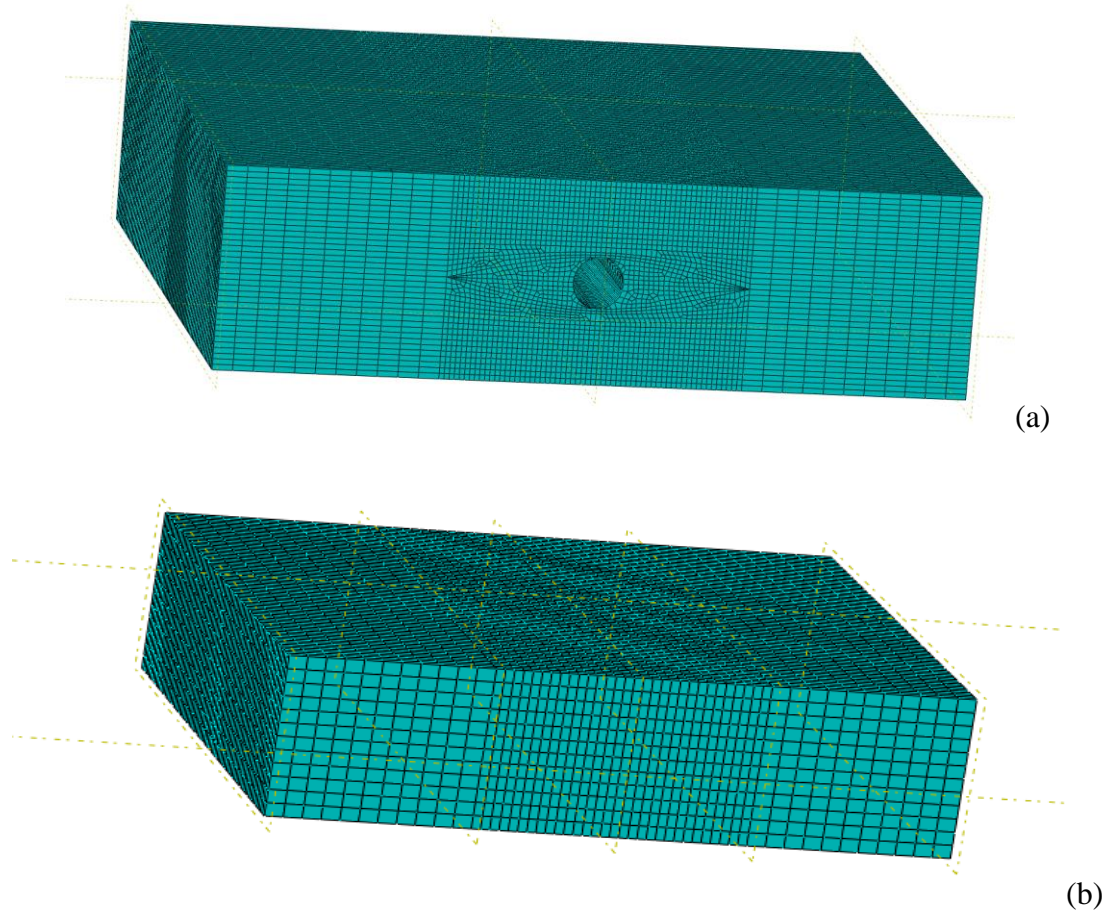


Figure 33: The Meshing of the Area of Interest for the Present Model for 3-Point Bending
a) with Microchannel b) without Microchannel

5. RESULTS AND DISCUSSIONS

The results of the thesis study are summarized in two major headlines. In this manner, i) Results of the validation model ii) the developed model. In the results of the validation model, 2-D and 3-D generated models are compared to the Huang et al. [20]'s results. After this part, results of the developed model, which is called present model, are presented. The present model results start with transverse stress that is applied according to ASTM 3039-D and continues with application of bending load according to ASTM D7264/D7264 M-15. In the analysis, the stress contours that varies with distance and stacking orders are given.

5.1. The Validation Model Results

Within the section, results of the validation model are given. The stress distributions along resin rich region are presented in Figure 34 to Figure 45. A, B, C and D points are illustrated in Figure 15 (in Chapter 4). In Figure 34 and Figure 35, the x-axis represents normalized distance that is obtained by the dividing the x values by the total length and the y-axis represents normalized stress are obtained by the average applied stress (1.65 GPa). The graph that are shown in Figure 36 and Figure 37, the normalized distance are calculated from vascule center points (from point A) to the end of the model (point C). Apart from Figure 34 to Figure 37, in Figure 38 and Figure 39 the normalized distance is calculated from points B-D-A.

In Figure 34 and Figure 35, the normalized stress in the x-direction (σ_x) is shown, while from Figure 36 to Figure 39, the normalized stress in the y-direction (σ_y) is shown. As it can be seen, the trends of these graphs in Figure 34, Figure 35, Figure 37 and Figure 39 seem to be in line with Huang et. al. [20]'s solutions. In Figure 34 and Figure 35, the longitudinal stress at resin pocket region are very low. And in composite region we can see the increasing stress due to its material stiffness, and at the end of the model it reaches to its maximum value, because the stress is applied at that point.

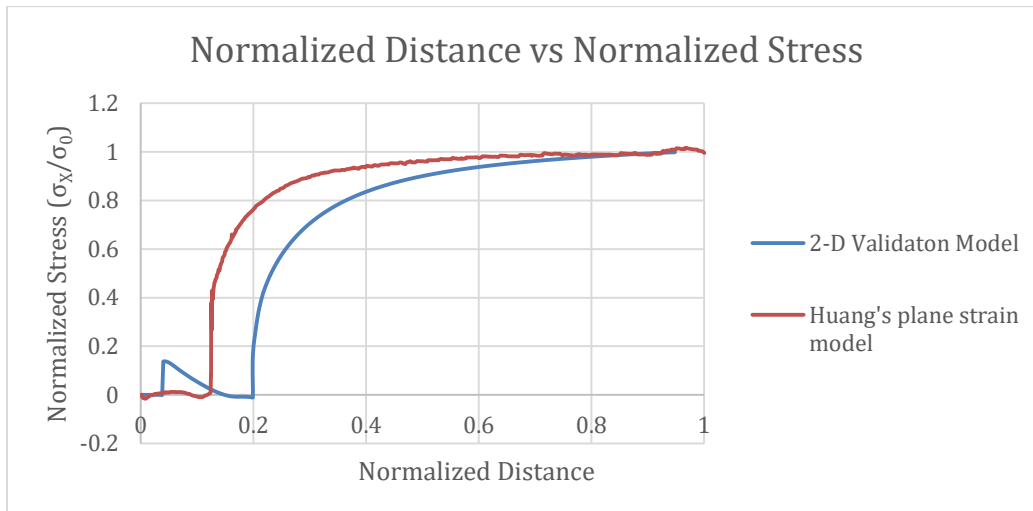


Figure 34: Comparison of Normalized σ_x along the x-axis for 2-D Validation Model and Huang’s Plane Strain Model

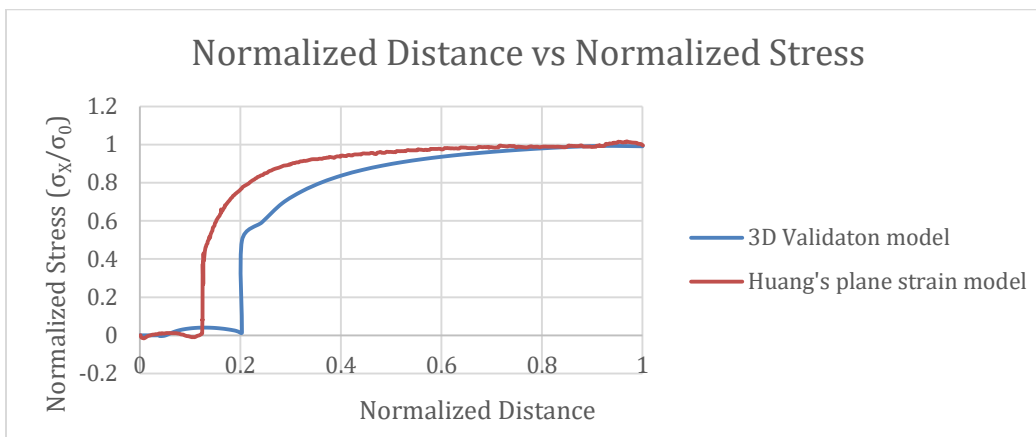


Figure 35: Comparison of Normalized σ_x along x-axis for 3-D Validation Model and Huang’s Plane Strain Model

Normalized stress distributions for σ_y is observed in Figure 36 and Figure 37. There is a peak in plane strain model, which validation model does not have. This point is the separation point, where the resin pocket regions is over and where lamina starts. As Al-Shawk et. al. [21]’s also imply in their study, extremely distorted triangular elements are present there. For that reason, the stress values at this point are not realistic and may vary for different models. In addition, comparing to plane strain model which is a 2-D model, validation model, which is a 3-D model, has different characteristics including mesh numbers and element types that may result in varying results. The reason the normalized stress does not reach to 1 from Figure 36 to Figure 39 is, the observed stress is being the

transverse stress. And this results in, lower stress values comparing to Figure 34 and Figure 35. Despite that, we can see that the trend is in with plane strain model. The results are also in line with Shivakumar and Bhargava [78] as well.

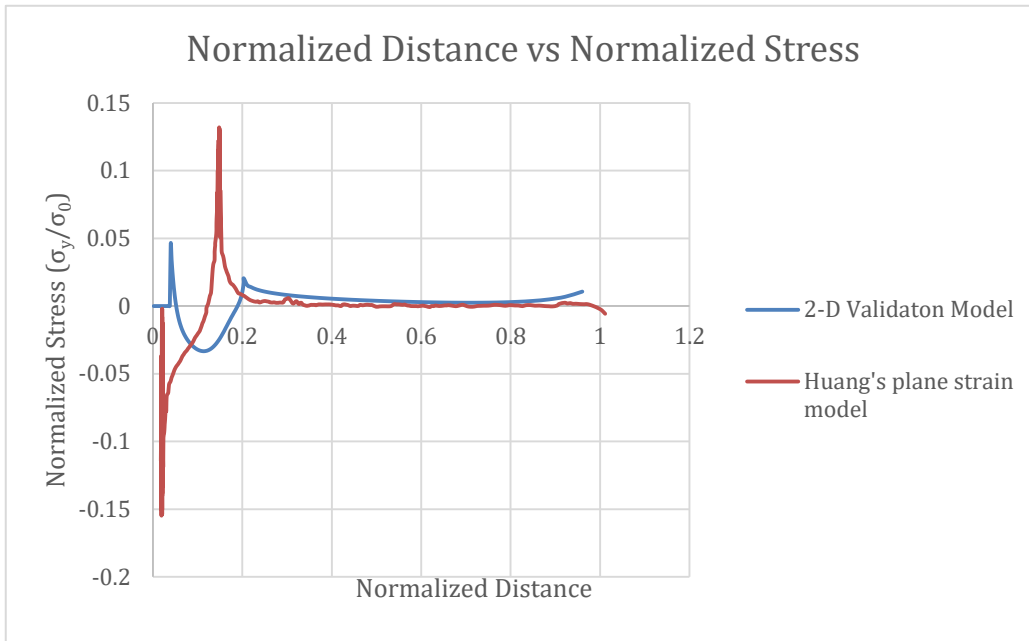


Figure 36: Comparison of Normalized σ_y along the x-axis for 2-D Validation Model and Huang's Plane Strain Model for Point C to Point A

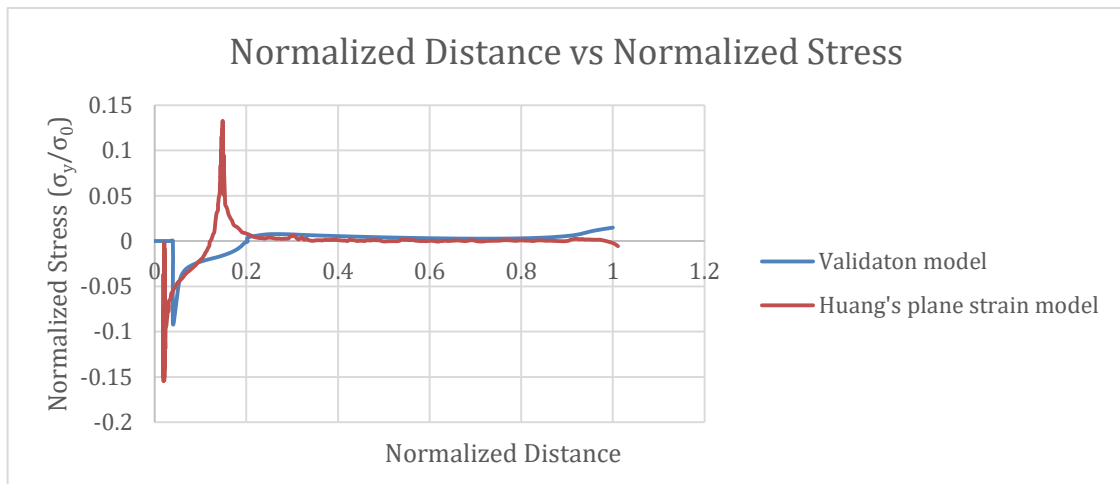


Figure 37: Comparison of Normalized σ_y along x-axis for 3-D Validation Model and Huang's Plane Strain Model for Point C to Point A

In Figure 38 and Figure 39, the normalized transverse stress according to normalized distance in BDA region are observed. At the end of the model we can see a gap in point A, and this is because of point A being the separation point for resin pocket region and

lamina causing different stress concentrations for different models as previously discussed explaining Figure 35 and Figure 36.

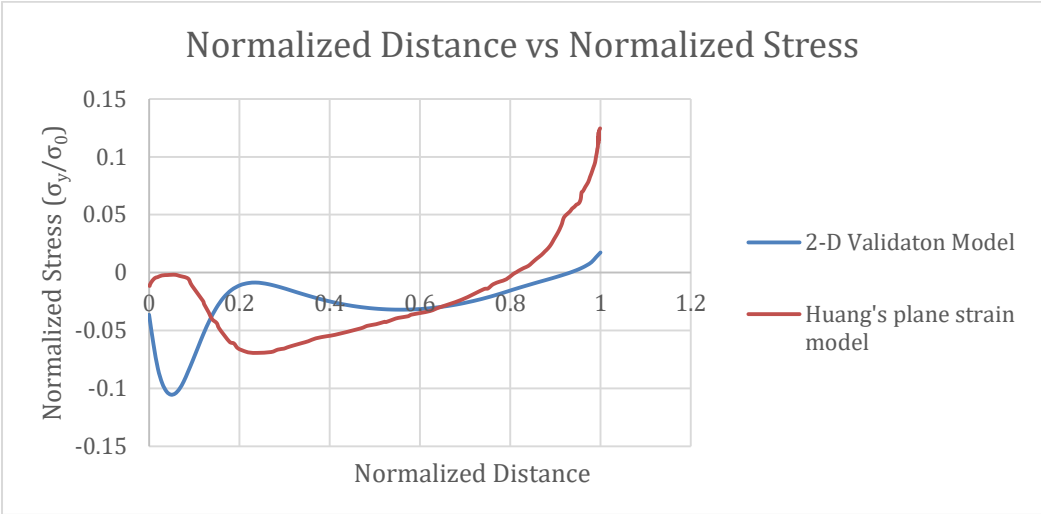


Figure 38: Comparison of Normalized σ_y along the BDA for 2-D Validation Model and Huang's Plane Strain Model for B-D-A Points

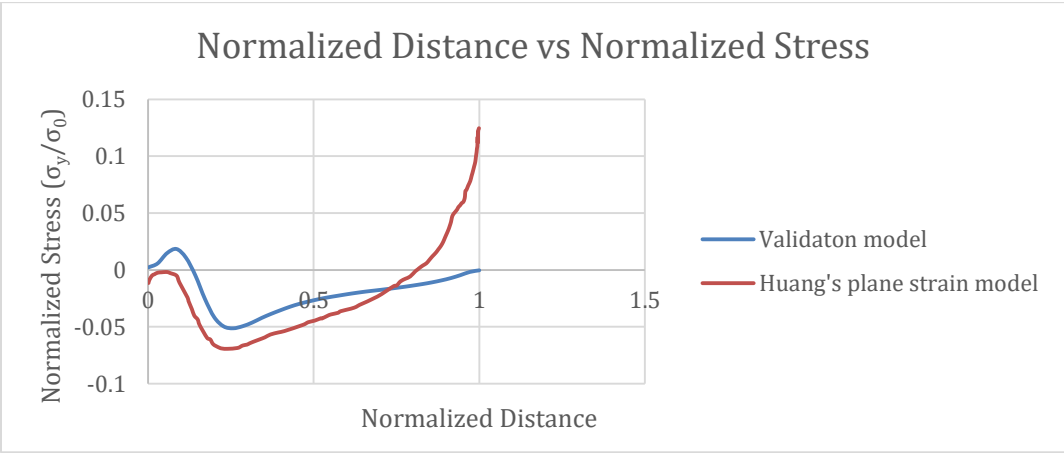


Figure 39: Comparison of Normalized σ_y along the BDA for 3-D Validation Model and Huang's Plane Strain Model for B-D-A Points

From Figure 40 to Figure 43, the stress and strain contours from Huang's plane strain model and validation model are presented. The results of the models show that, the maximum longitudinal tensile stress and the maximum longitudinal tensile strain are develop at point close to point B. While, the maximum transverse tensile stress and the maximum transverse tensile strain are developed at a point that is close to point C.

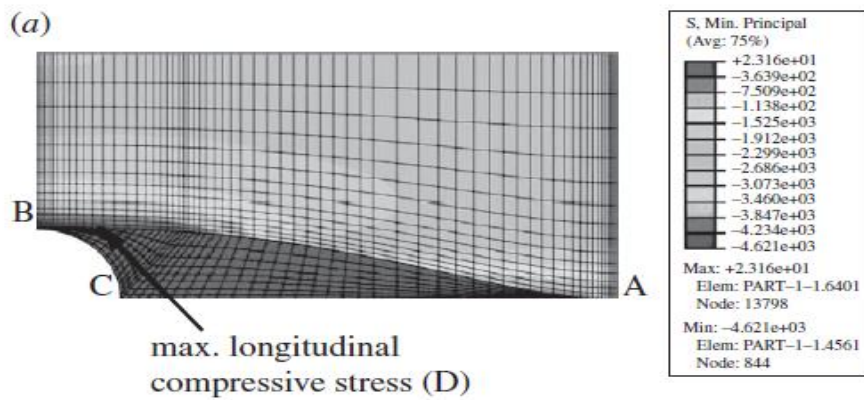
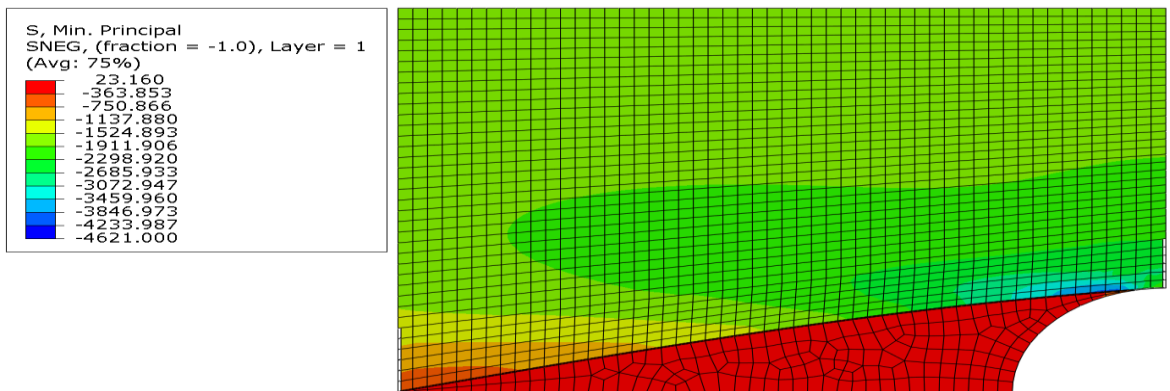
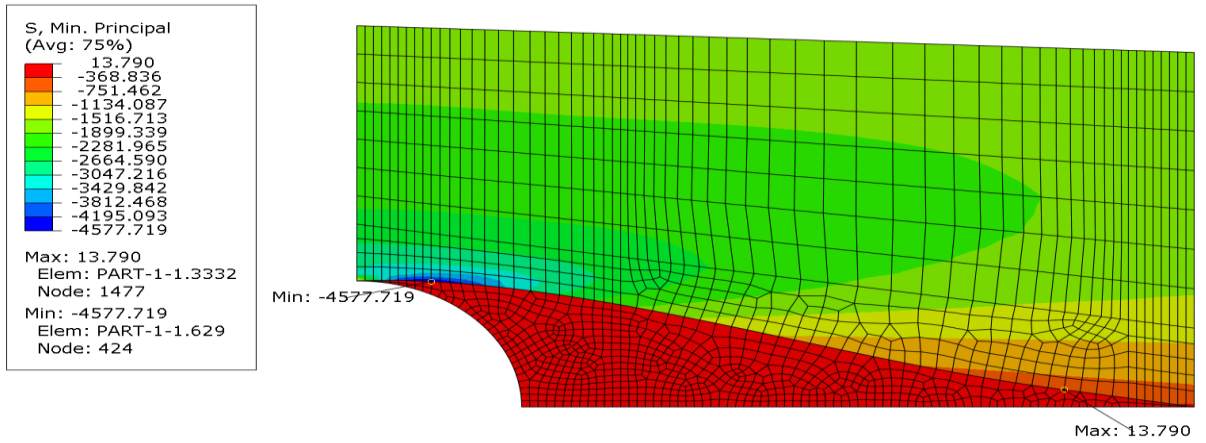


Figure 40: Comparison of S,Min, Principal Values of 2-D Validation Model, 3-D Validation Model and Huang's Plane Strain Model

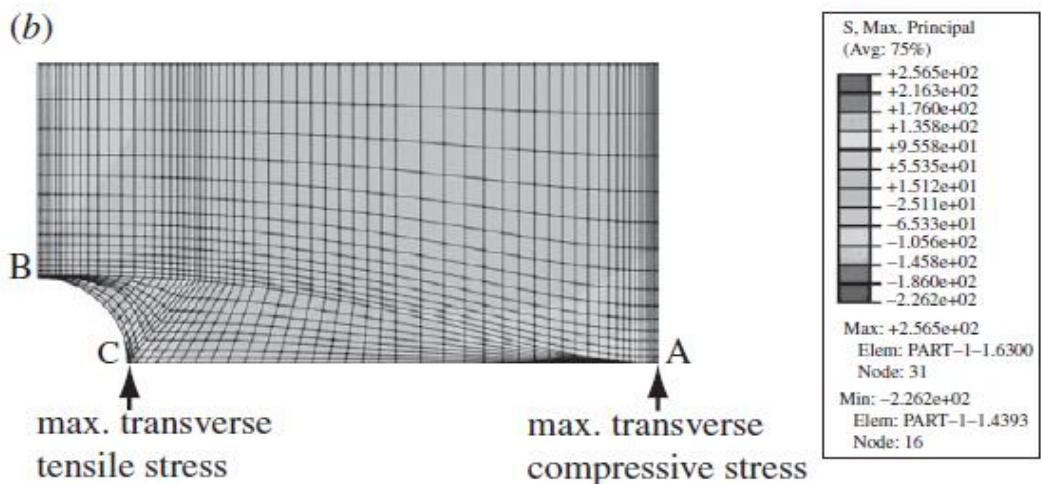
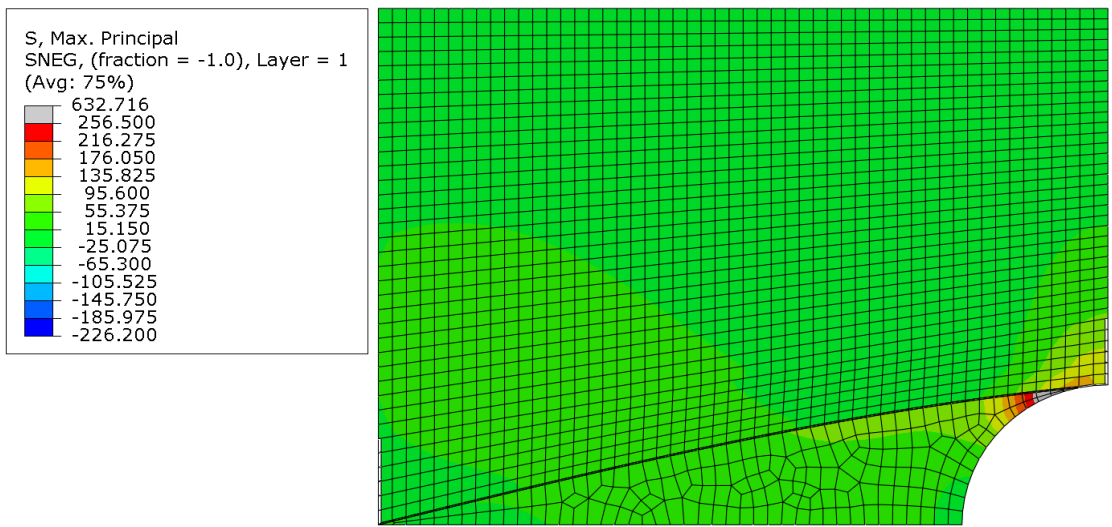
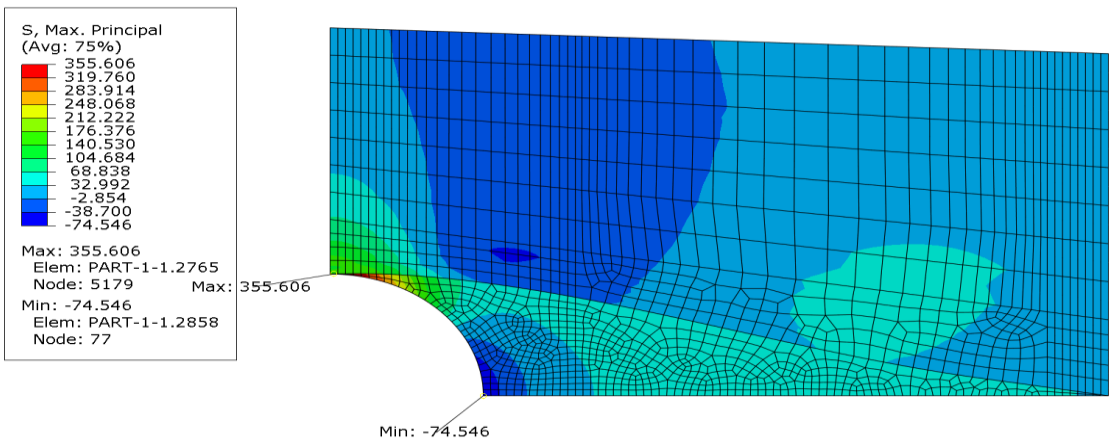


Figure 41: Comparison of S,Max, Principal Values of 2-D Validation Model, 3-D Validation Model and Huang's Plane Strain Model

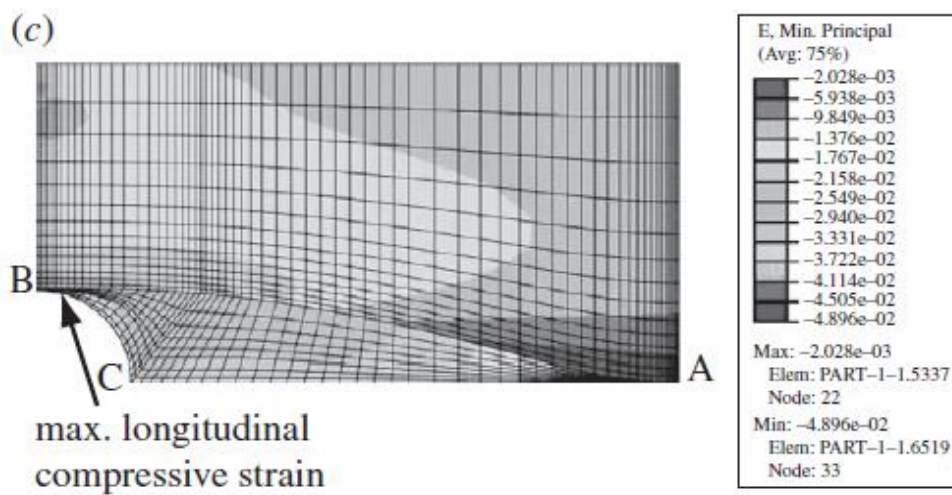
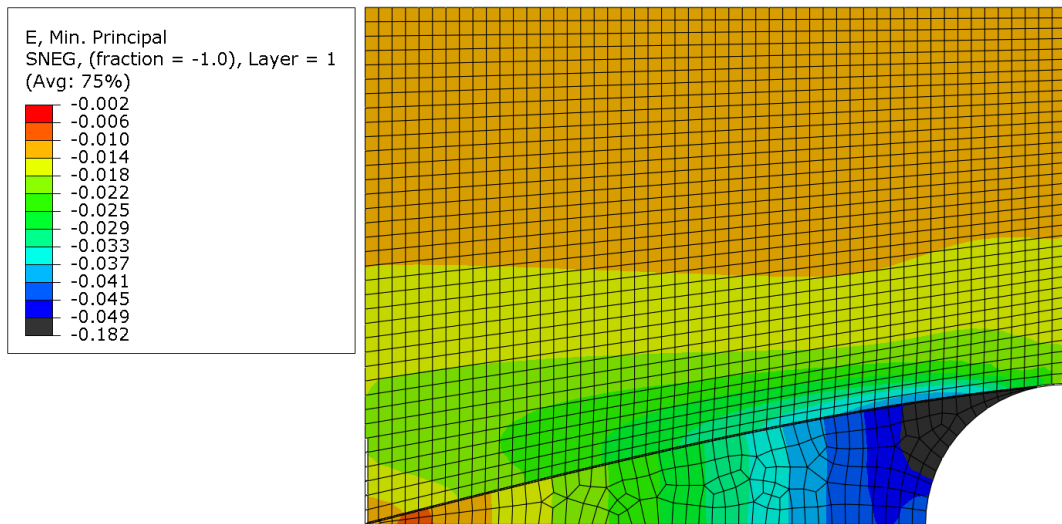
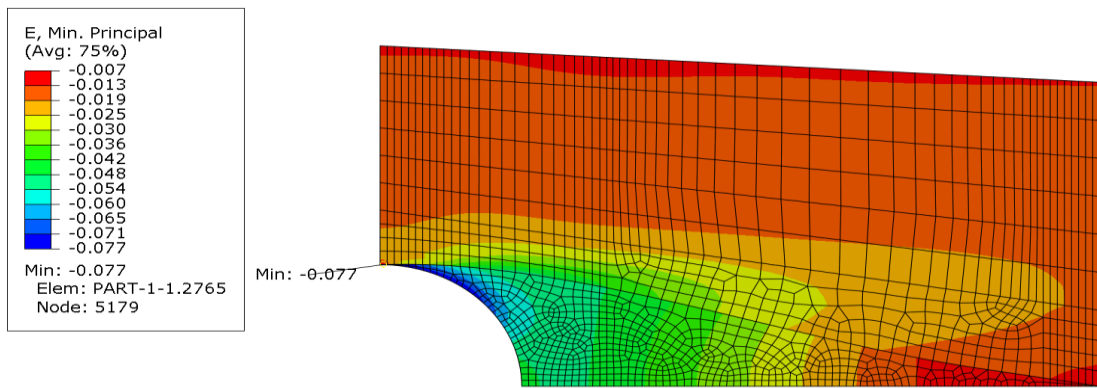


Figure 42: Comparison of E,Min, Principal Values of 2-D Validation Model, 3-D Validation Model and Huang's Plane Strain Model

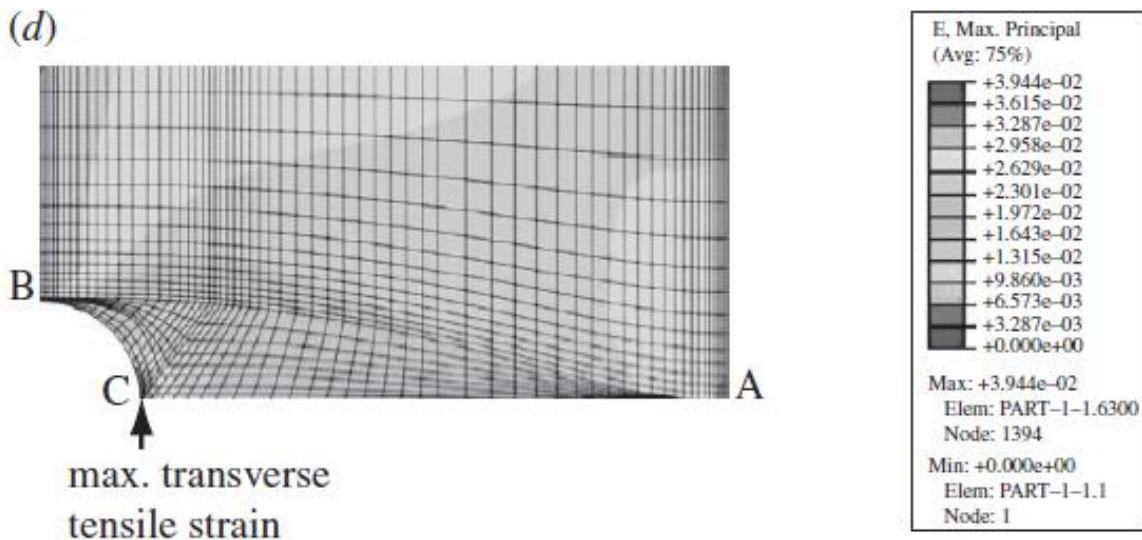
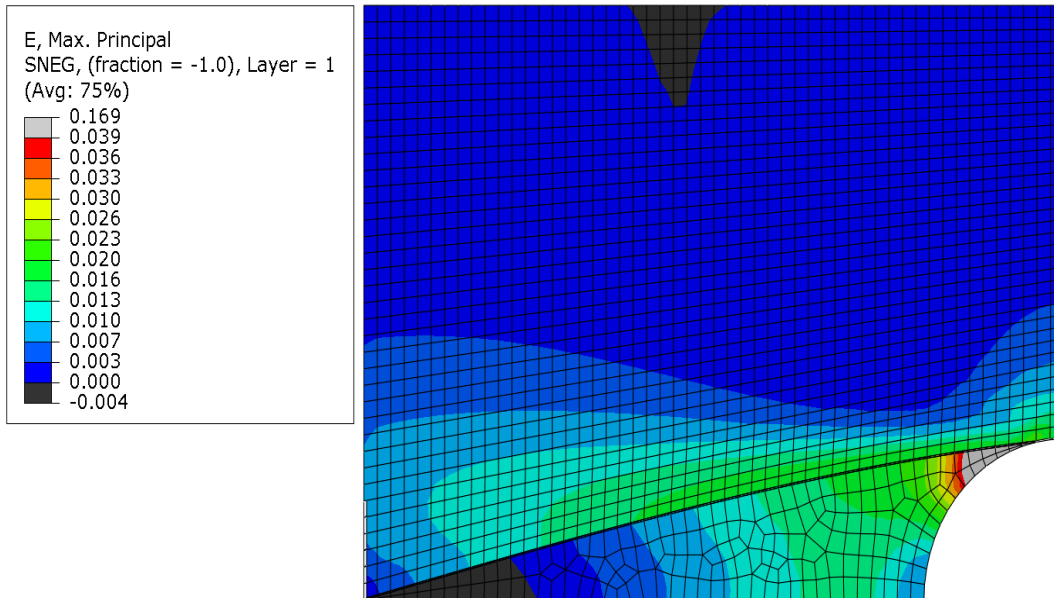
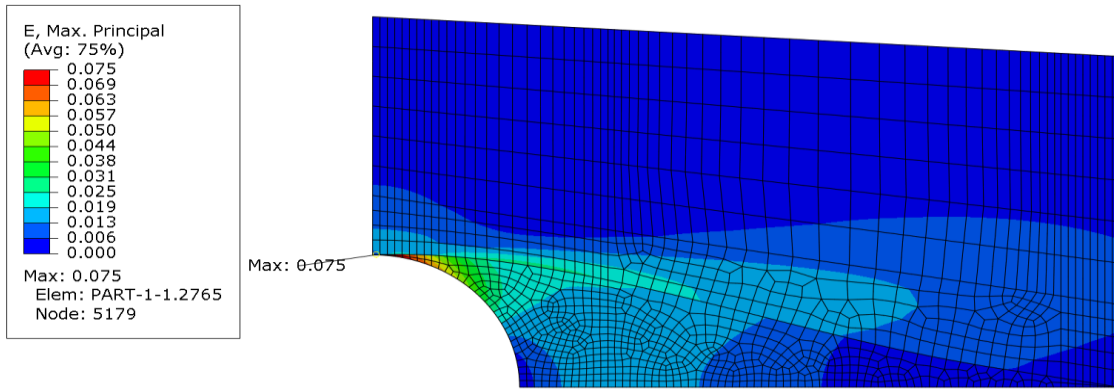


Figure 43: Comparison of E,Max, Principal Values of 2-D Validation Model, 3-D Validation Model and Huang's Plane Strain Model

According to the results presented above, the validation model and plane strain model give similar outputs. Thus, validation model is validated and can be used for different stacking configurations with different loads and boundary conditions.

In the previous chapters, Huang's et. al. [20]'s study the curing effects was studied. In the validation model, curing is studied as well. First, the curing temperature is selected as 150°C and then the material is cooled down to 20°C. The results for longitudinal and transverse stress contours with and without curing cases are presented. As it can be deduced from the Figure 44 and Figure 45, the curing effects the longitudinal and transverse stress distribution for the area of interest with an insignificant amount. Henceforth, in the present model the curing effect will not be included. In addition, by excluding the curing effect, effects of the other parameters will be observed solely and thus the coupling effects will be avoided.

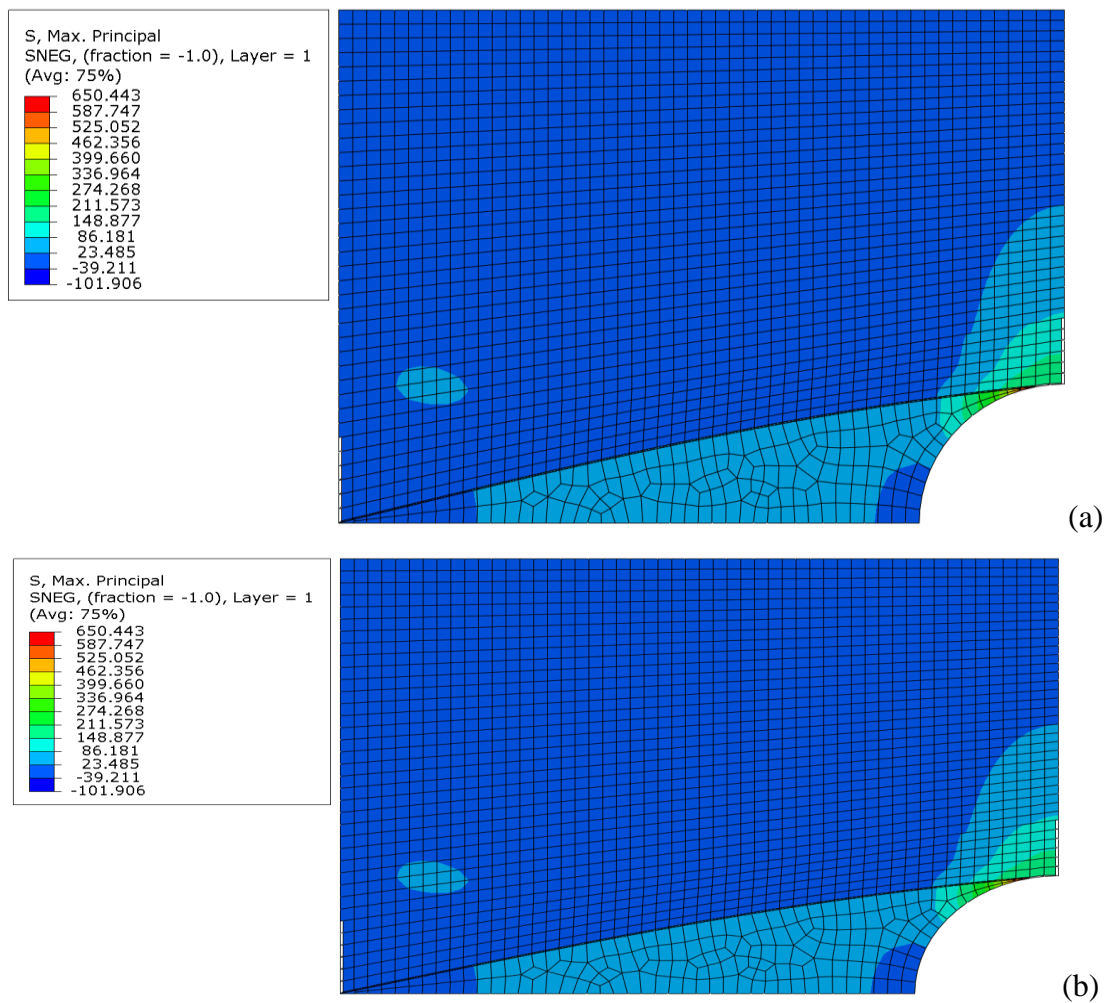


Figure 44: Longitudinal Stress Contours for the Validation Model (a) with Curing Effects, (b) without Curing Effects

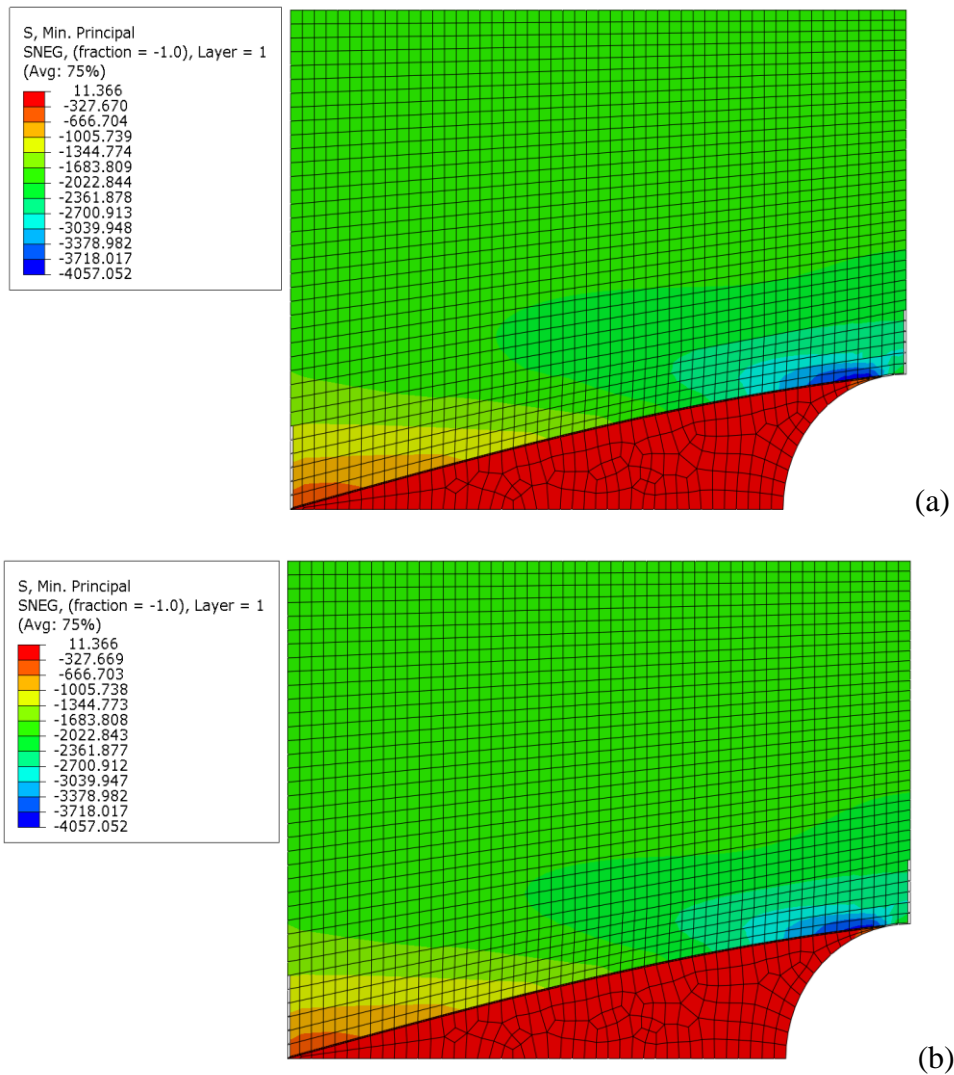


Figure 45: Transverse Stress Contours for the Validation Model (a) with Curing Effects, (b) without Curing Effects

5.2 Present Study Results

In this chapter, the effect of different stacking sequences under transverse compression and tension are presented.

5.2.1 Longitudinal Stress Distributions for Transverse Compression:

The longitudinal stress distributions for transverse compression are presented in Figure 46. The stacking configuration of UD90 has the highest compressive stress concentration comparing to the other configuration and UD0 has the lowest, whereas $[0/90]_{3s}$ and $[90/0]_{3s}$ have stress concentration values that has in between those UD0 and UD90. For all the configurations, it can be deduced that, the stress concentration are focused on the area between point B and point C.

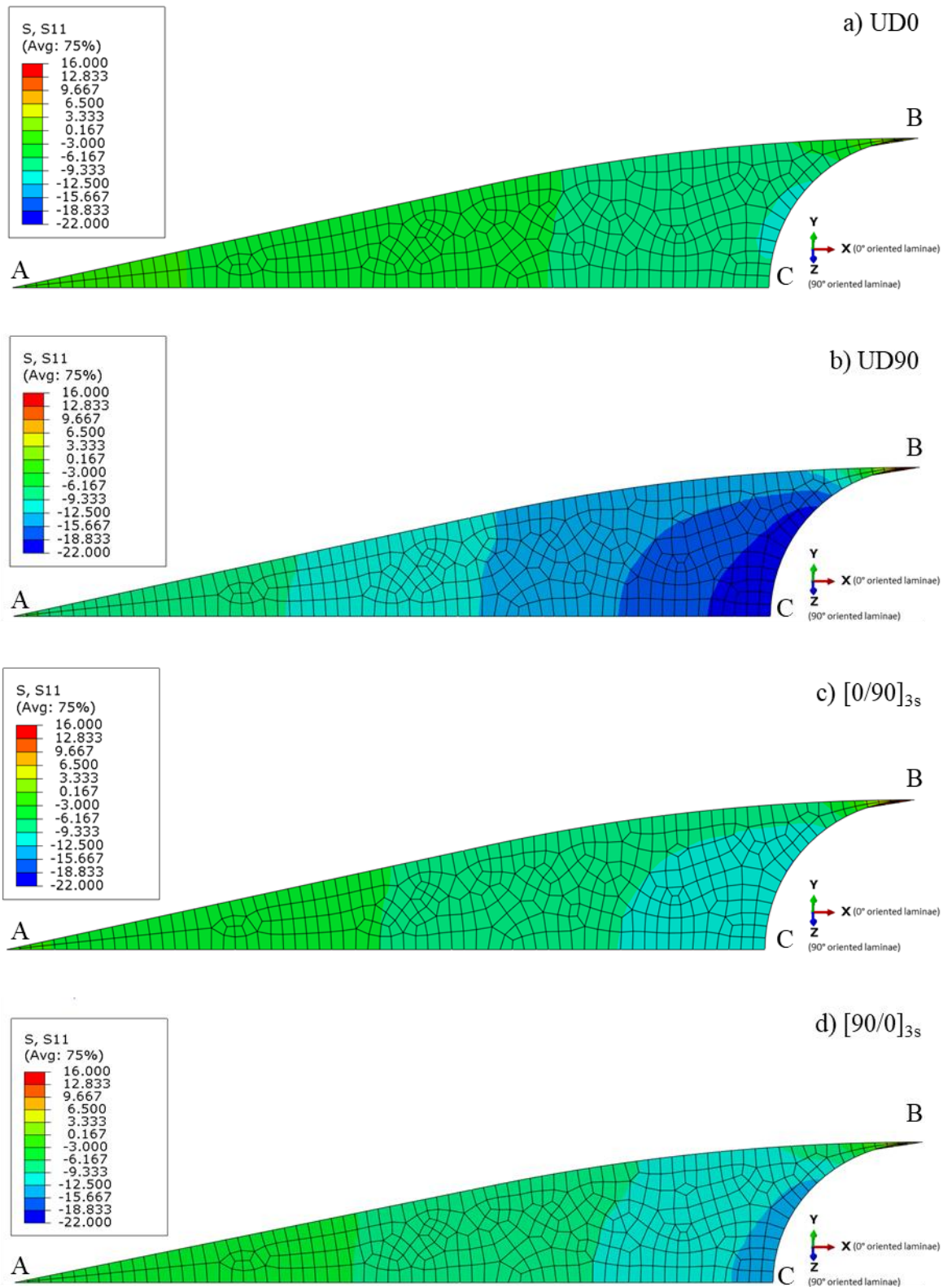


Figure 46: Longitudinal Stress Distributions for Present Model under Transverse Compression for a) UD0 b) UD90 c) [0/90]_{3s} d) [90/0]_{3s}

If we take a look at the Figure 47 and Figure 48, it seems that, UD90 has the largest normalized stress value in transverse compression and transverse tension through point B- point A and point C to point A. UD0 has the minimum transverse loads, whereas [0/90] stacking configurations have quite similar values, ranging in between UD90 and UD0 stress distributions. In Figure 47, the largest stress occurs at point B and in Figure 48, the largest stress occurs at point C. In both figures stress values decrease towards point A. The volume of resin around point B or point C is much more comparing to the point A. In other words, around point A, the compression loads are compensated by the lamina.

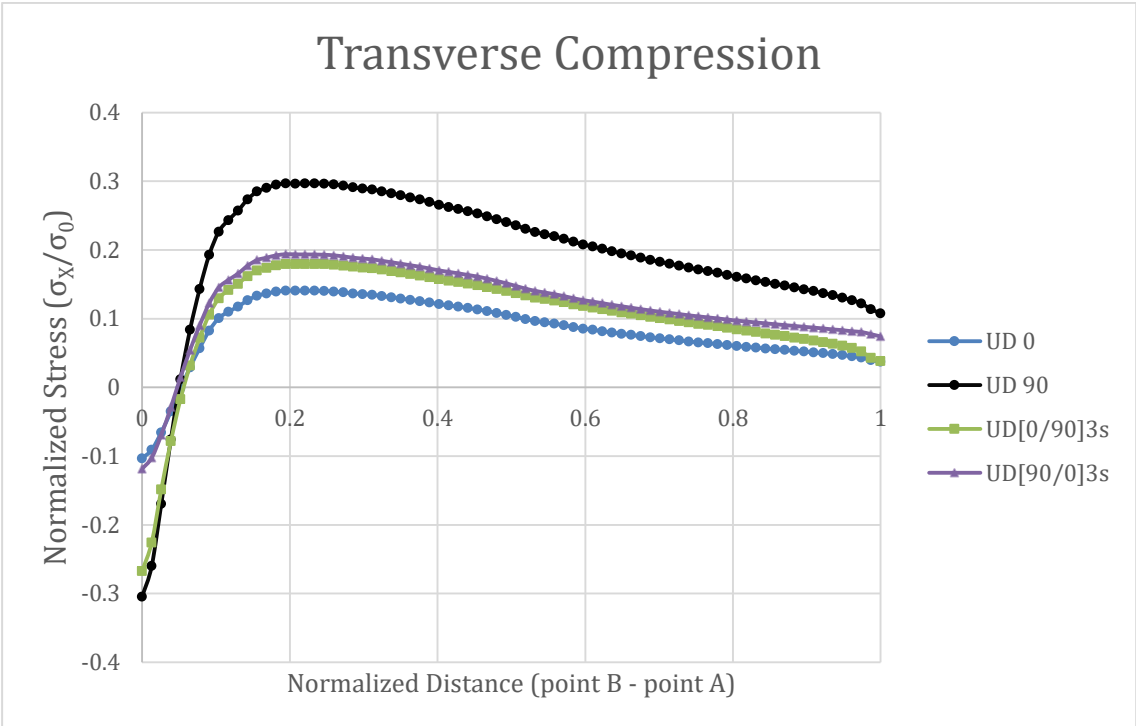


Figure 47: Normalized σ_x Distribution for 1 mm Channel Diameter through Point B to Point A under Transverse Compression

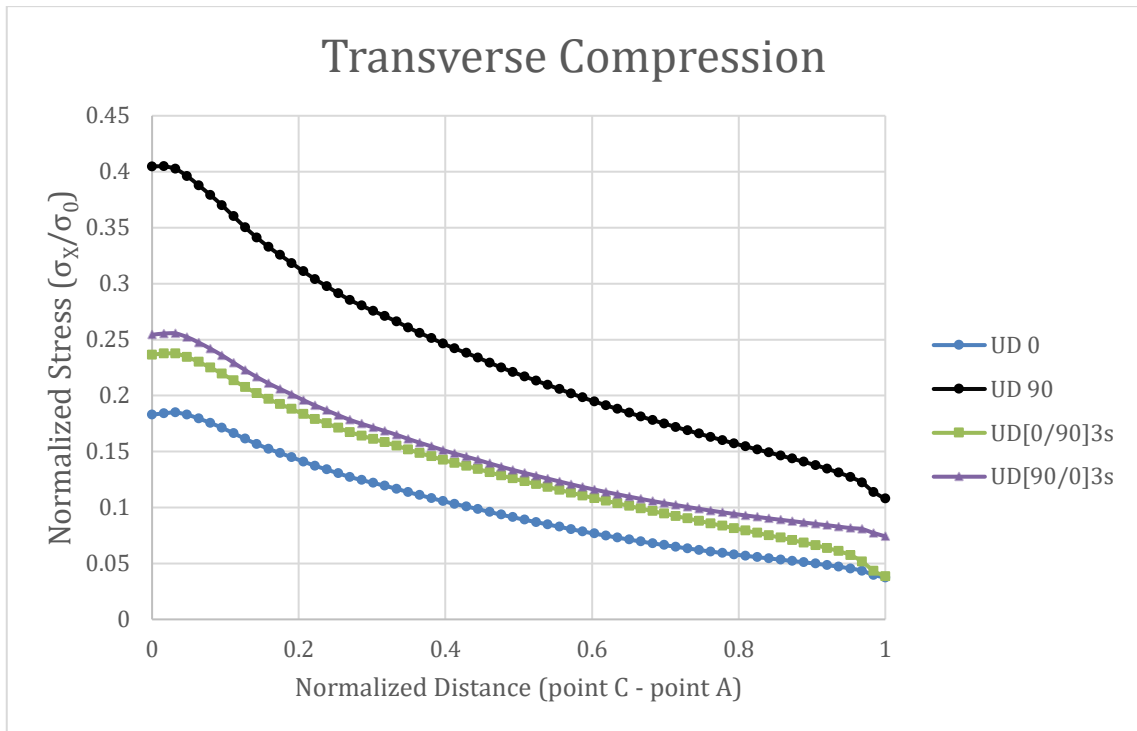


Figure 48: Normalized σ_x Distribution for 1 mm Channel Diameter through Point C to Point A under Transverse Compression

5.2.2 Longitudinal Stress Distributions for Transverse Tension:

The longitudinal stress distributions for transverse tension are presented in Figure 49. The stacking configuration of UD90 has the highest tensile stress concentration comparing to the other configuration and UD0 has the lowest, whereas [0/90]3s and [90/0]3s have stress concentration values that has in between those UD0 and UD90. For all the configurations, it can be deduced that, the stress concentration are focused on the area between point B and point C.

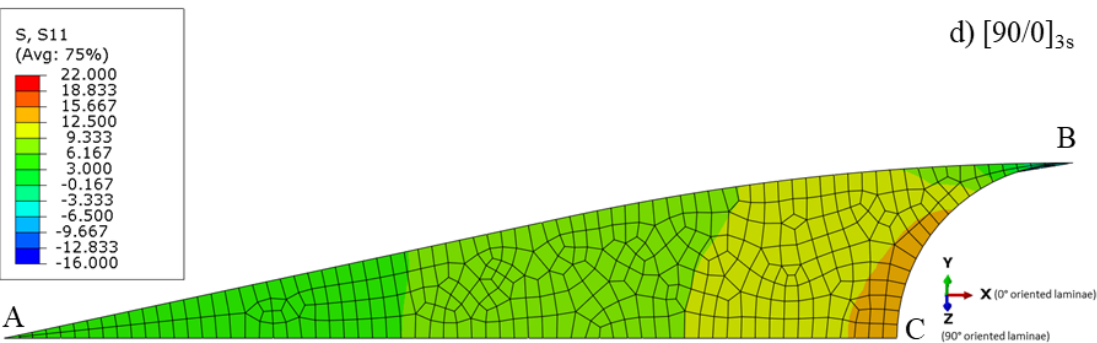
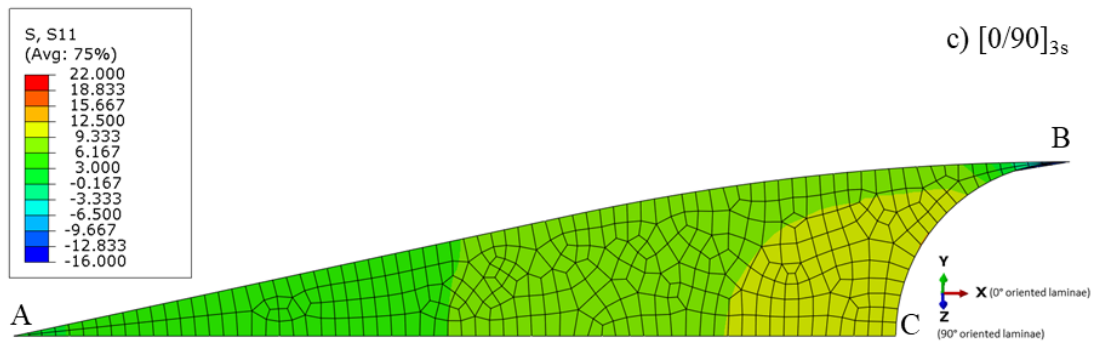
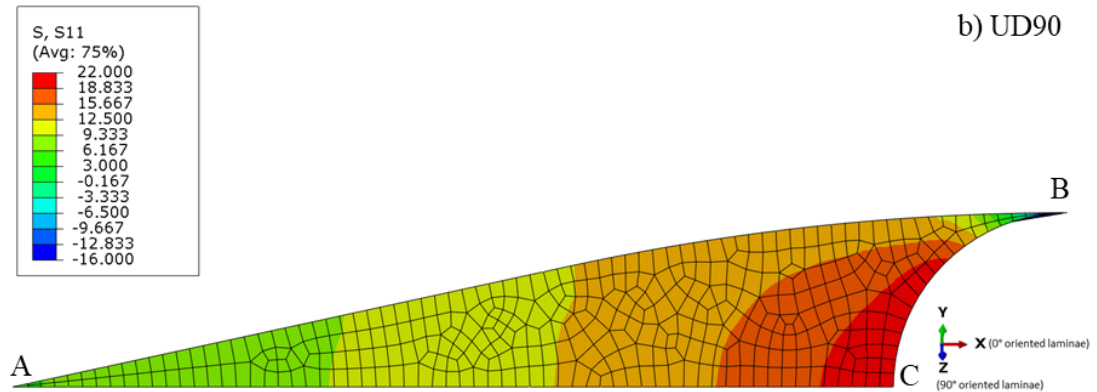
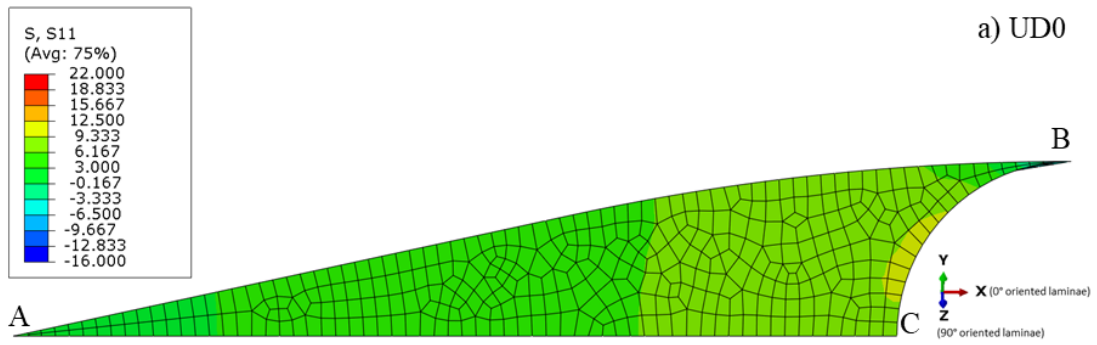


Figure 49: Longitudinal Stress Distributions for Present Model under Transverse Tensile for a) UD0 b) UD90 c) [0/90]_{3s} d) [90/0]_{3s}

If we take a look at the Figure 50 and Figure 51, it seems that, UD90 has the largest normalized stress value in transverse compression and transverse tension through point B- point A and point C to point A. UD0 has the minimum transverse loads, whereas [0/90] [90/0] stacking configurations have quite similar values, ranging in between UD90 and UD0 stress distributions. In Figure 50, the largest stress occurs at point B and in Figure 51, the largest stress occurs at point C. In both figures stress values decrease towards point A which is basically same reason with the transverse compression case.

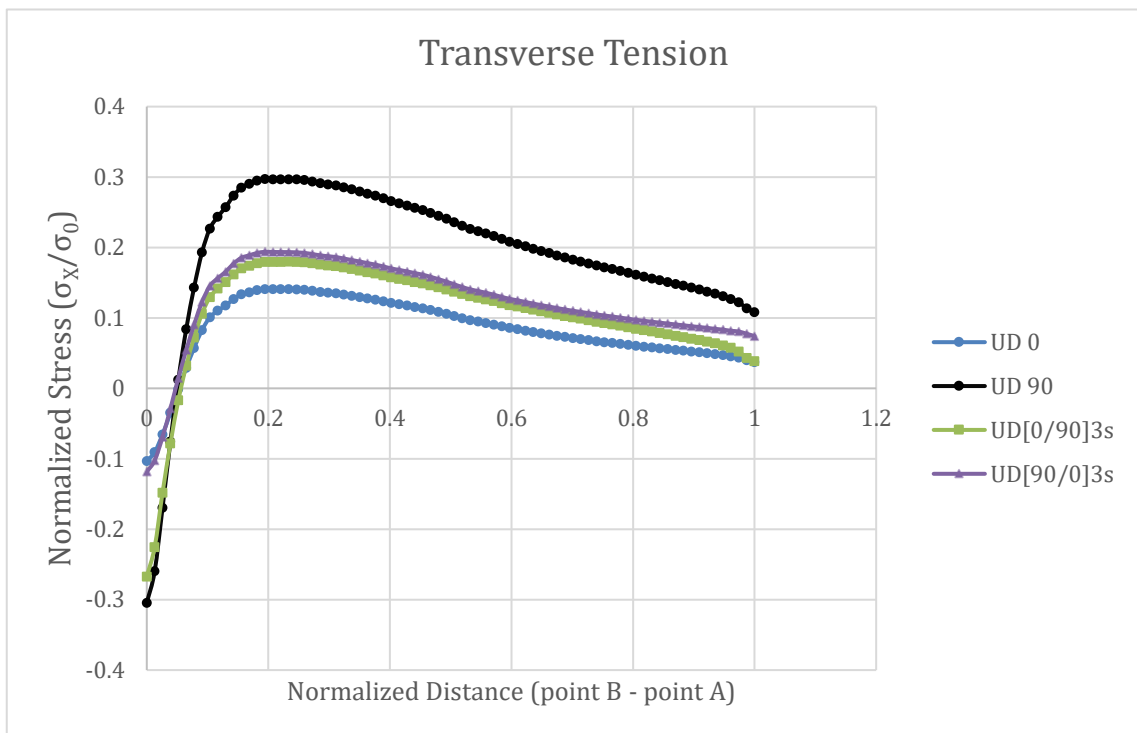


Figure 50: Normalized σ_x Distribution for 1 mm Vasculature Diameter through Point B to Point A under Transverse Tension

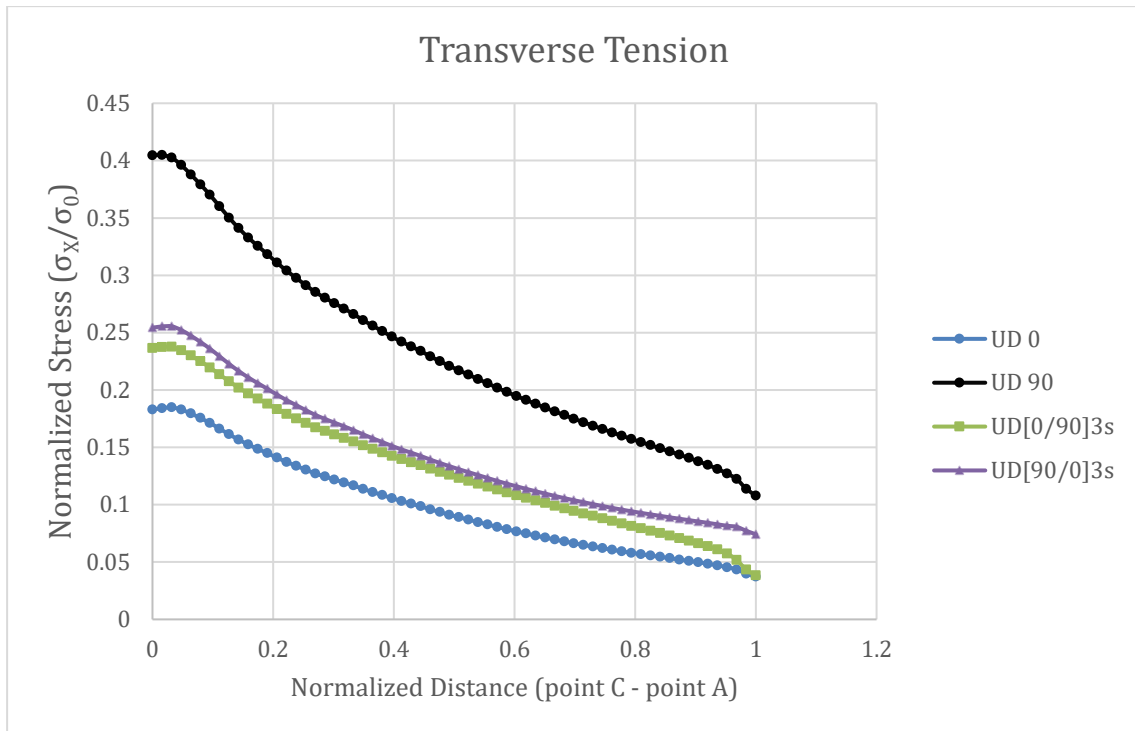


Figure 51: Normalized σ_x Distribution for 1 mm Vasculature Diameter through Point C to Point A under Transverse Tension

5.2.3 3-Point Bending:

In order to compare the results of 3-Point Bending results of model with microchannel and without microchannel, owing to there are many stacking configurations, only stress contours for in S,Max, Principal is selected. In order to better see the results, y and z planes are cut in the middle as shown in Figure 52.

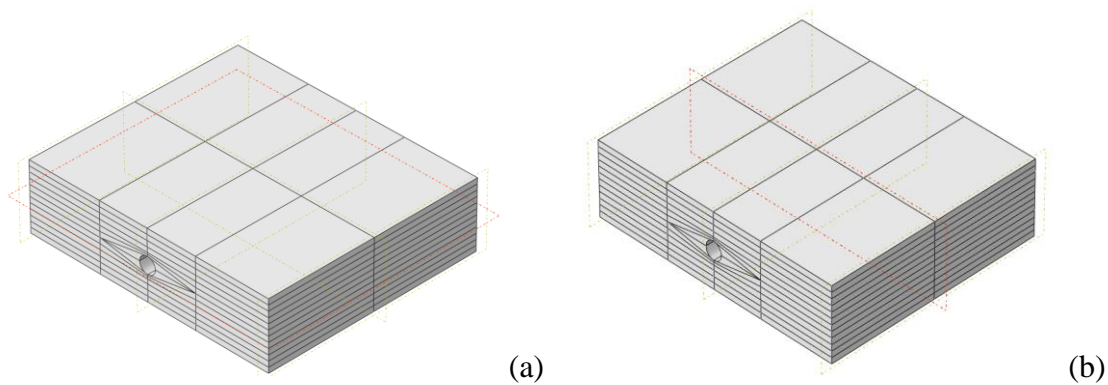


Figure 52: Investigation of 3-Point Bending Model's Cross Section a) y-plane b) z-plane

From Figure 53 to Figure 60, it can be deduced that there are no major changes in the resin rich region's stress distributions comparing to the model without microchannel. Considering all the stacking configuration's compression load distribution, the maximum

compression load in z-plane is always more than the maximum compression load in the y plane. The main reason behind this is, for y plane analysis, the model is cut in half of its height (2 mm), which gets less effected from load roller's compression loads. As for z plane the model height is whole (4 mm) and the biggest stress contours appears to be on the surface where the load roller applies compression loads. As for the y-plane and z-plane in general, the difference in stress magnitudes and rates are presented in Table 7 and Table 8 respectively.

Table 7: The Difference in Maximum and Minimum Stresses of the Model with Microchannel and without Microchannel for 3 Point Bending Loads with y-Plane and z-Plane

Stacking Configuration	y-Plane				z-Plane			
	With Microchannel		Without Microchannel		With Microchannel		Without Microchannel	
	Maximum Tensile Stress (MPa)	Maximum Compression Stress (MPa)	Maximum Tensile Stress (MPa)	Maximum Compression Stress (MPa)	Maximum Tensile Stress (MPa)	Maximum Compression Stress (MPa)	Maximum Tensile Stress (MPa)	Maximum Compression Stress (MPa)
[90/0] _{3s}	170.5	-1.4	175.6	-2.6	170.5	-39.8	162.7	-26.4
[0/90] _{3s}	204.4	-1.4	190.4	-3.5	204.3	-31	190.4	-19.2
UD0	200.9	-1.4	182.3	-4.5	200.9	-34	182.3	-20.2
UD90	81.5	-1.1	75.6	-3.2	81.5	-30.8	75.6	-19.2

Table 8: The Difference in Maximum and Minimum Stress Rates of Model with Microchannel and Without Microchannel for 3 Point Bending Loads with y-Plane and z-Plane

Stacking Configuration	y-Plane		z-Plane	
	Difference in Maximum Tensile Stress (%)	Difference in Maximum Compression Stress (%)	Difference in Maximum Tensile Stress (%)	Difference in Maximum Compression Stress (%)
[90/0] _{3s}	-2.9	-46.2	4.8	50.8
[0/90] _{3s}	7.4	-60.0	7.3	61.5
UD0	10.2	-68.9	10.2	68.3
UD90	7.8	-65.6	7.8	60.4

Figure 53 presents that, the model with microchannel for [90/0]_{3s} stacking configuration’s highest tensile loads are not located at the bottom part (the last stack) of the model but in a lamina which is above the last stack. And this stack is Lamina 0 which is more fragile in this direction comparing to Lamina 90. This statement is both valid for the model with microchannel and without microchannel in y-plane and z-plane. Figure 54 denotes that in the z-plane the resin rich region stress contours shows that the area around the microchannel spread the compression loads comparing to the model without microchannel. This is due to resin’s mechanical response to the compressive loads that are created by bending. According to the Table 7 and Table 8, [90/0]_{3s} stacking configuration has 2.9% decrease in maximum tension stress and 46.2% decrease maximum compression stress in y-plane. As for z-plane there is 48.8% increase in tension and 50.8% increase in compression. This result is pretty good except for the increase stress compressive load in the z-plane.

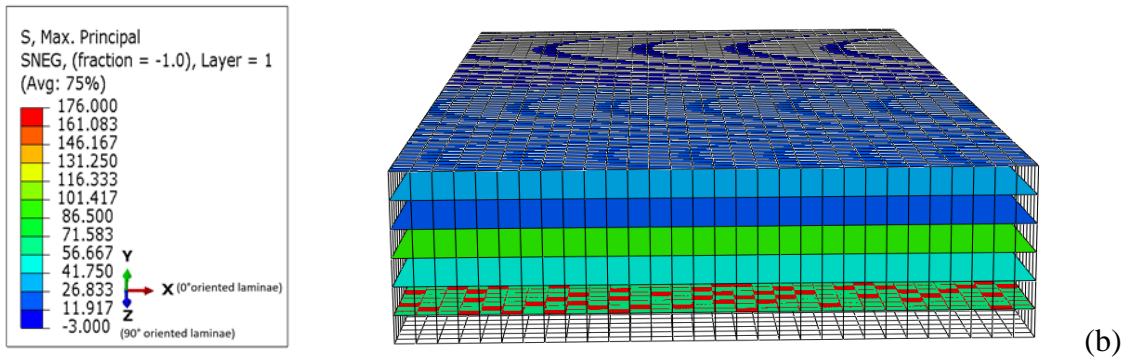
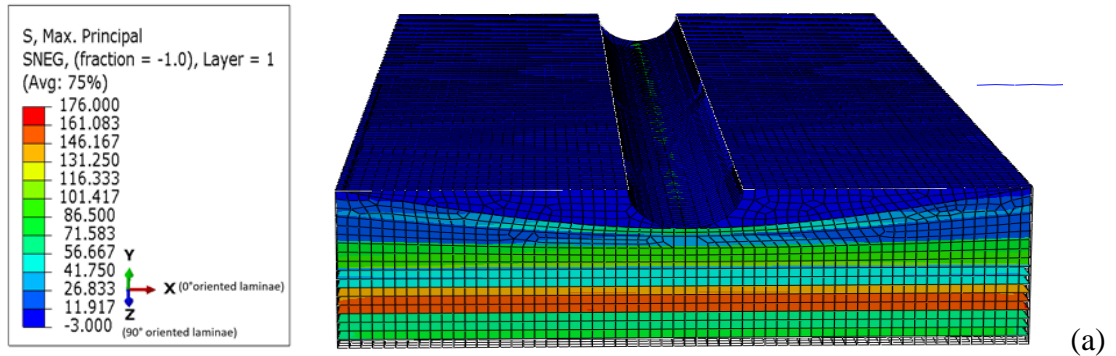


Figure 53: S,Max, Principal Stress Contours for the 3-Point Bending Model with $[90/0]_{3s}$ Stacking Configuration for y-plane Cut (a) with (b) without Microchannel

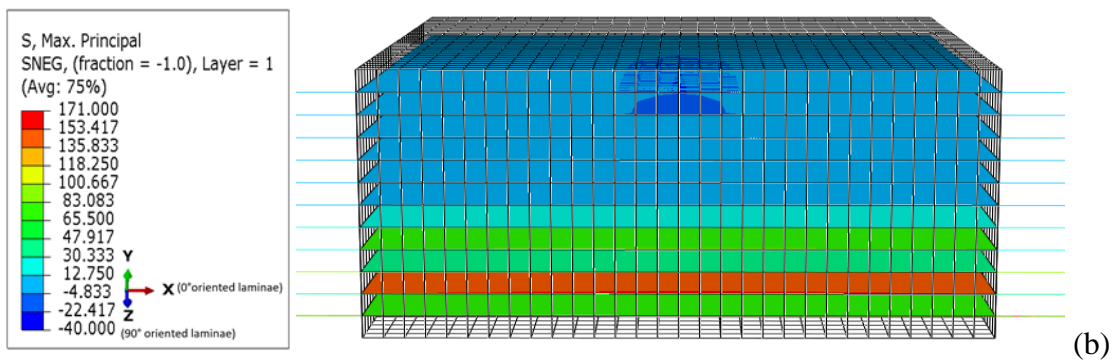
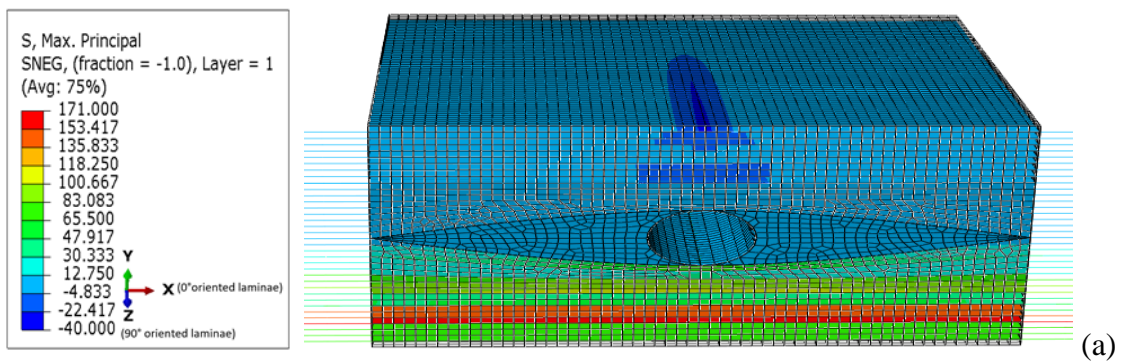


Figure 54: S,Max, Principal Stress Contours for the 3-Point Bending Model with $[90/0]_{3s}$ Stacking Configuration for z-plane Cut (a) with (b) without Microchannel

Figure 55 shows that, the model with microchannel for $[0/90]_{3s}$ stacking configuration's stress distribution for the y-plane seems to be negligible. Figure 56 indicates that, for the z plane, the stress distribution around the resin has more compression loads comparing to the model without channel and below this resin rich region the laminate seems to have lower stress values comparing to the model without channel. According to the Table 7 and Table 8, $[0/90]_{3s}$ stacking configuration has 7.4% increase in maximum tensile stress and 60% decrease in maximum compression stress which are tension and compression loads in y-plane. As for z-plane this values are 7.8% increase and 60.4% increase respectively.

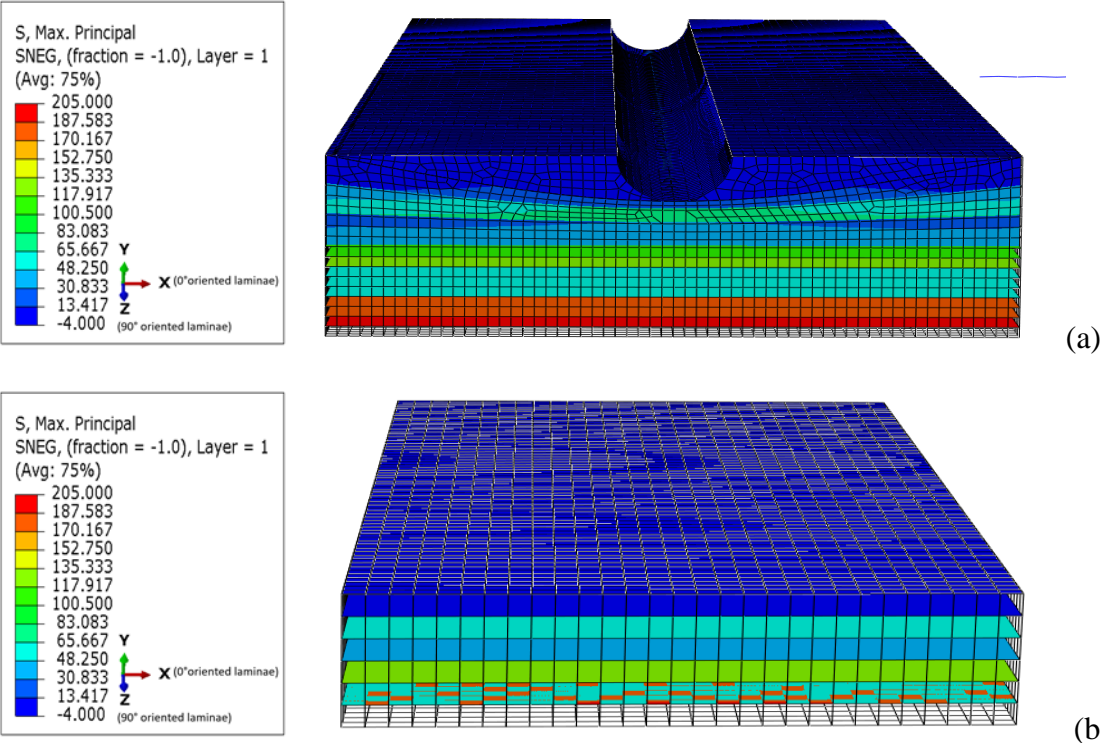


Figure 55: S,Max,Principal Stress Contours for the 3-Point Bending Model with $[0/90]_{3s}$ Stacking Configuration for y-plane Cut for (a) with Microchannel (b) without Microchannel

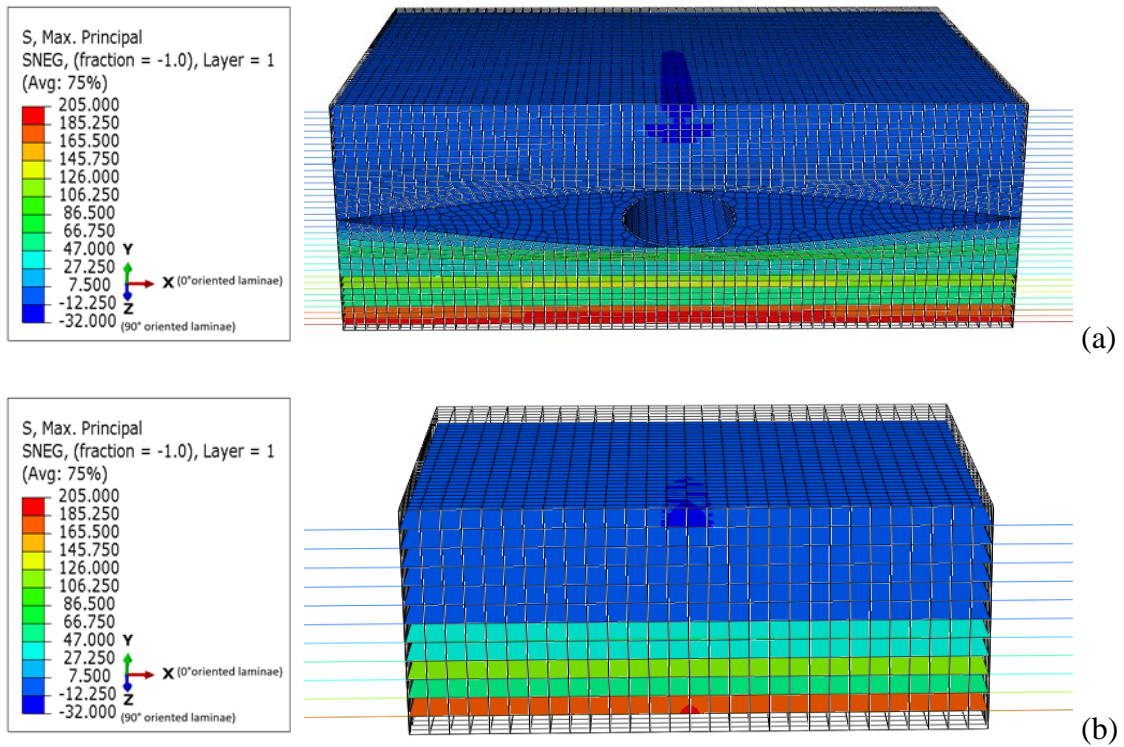


Figure 56: S,Max,Principal Stress Contours for the 3-Point Bending Model with $[0/90]_{3s}$ Stacking Configuration for z-plane Cut for (a) with Microchannel (b) without Microchannel

Figure 57 indicates that, the model with microchannel for UD0 stacking configuration's compression stress distribution around the resin region in the y-plane, has a slight difference in magnitude which can assumed to be negligible. If we examine Figure 58 however, both for y-plane and z-plane, the maximum stress that occurs on the bottom of the model has increased. The reason for this is, structural deformation of the UD0 laminates which has low strength due to its fiber alignment is in the transverse to its loading direction. According to the Table 7 and Table 8, UD0 stacking configuration has 10.2% increase in maximum stress and 68.9% decrease in minimum stress which are tension and compression loads in y-plane. As for z-plane this values are 10% and 68.3% increase respectively.

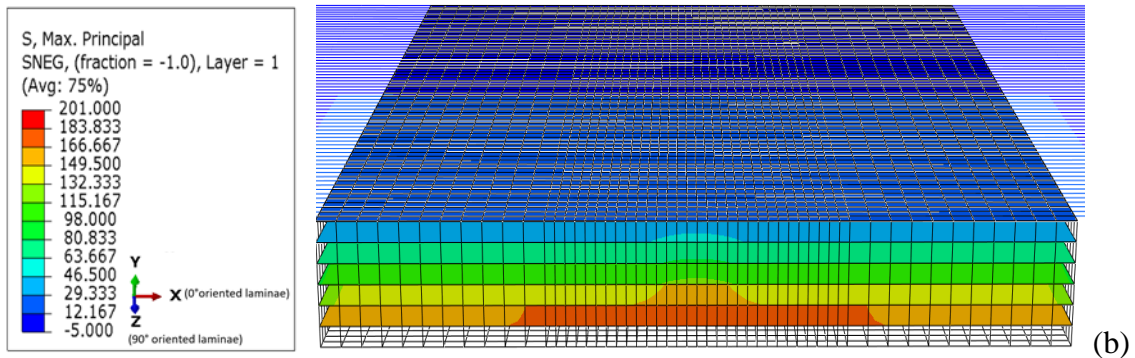
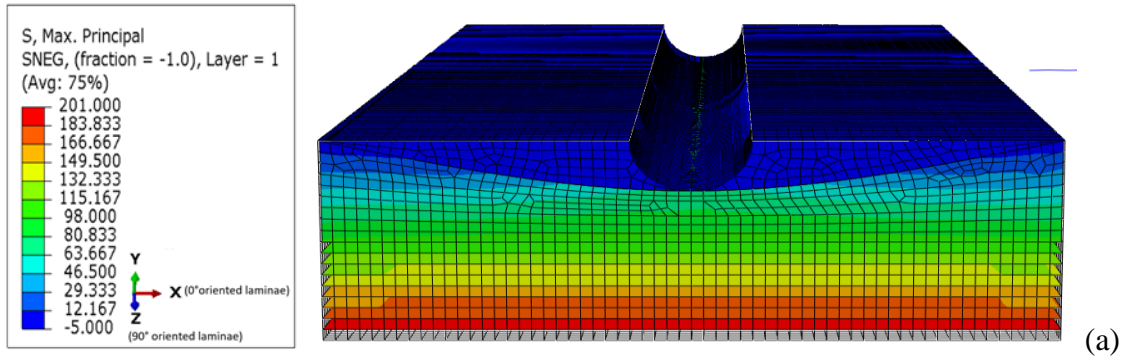


Figure 57: S, Max, Principal Stress Contours for the 3-Point Bending Model with UD0 Stacking Configuration for y-plane Cut (a) with Microchannel (b) without Microchannel

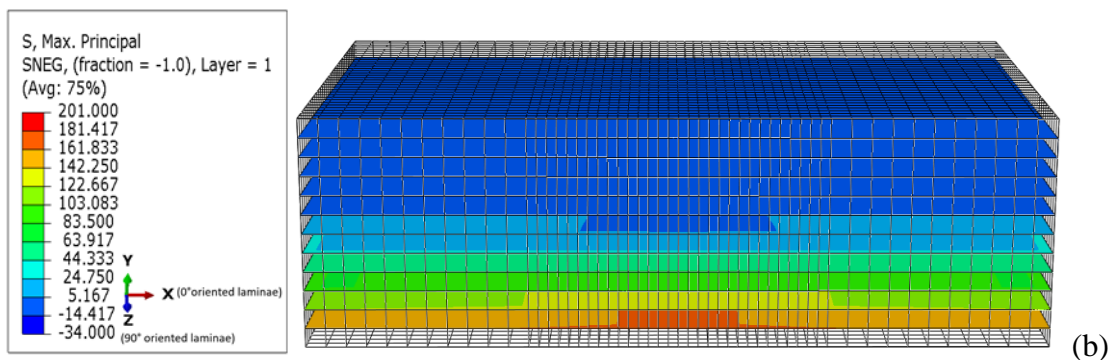
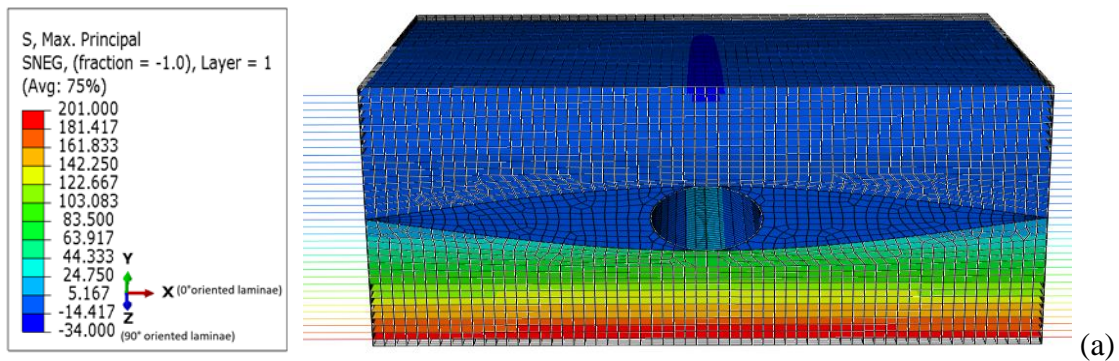


Figure 58: S,Max, Principal Stress Contours for the 3-Point Bending Model with UD0 Stacking Configuration for z-plane Cut (a) with Microchannel (b) without Microchannel

Figure 59 demonstrates that, the model with microchannel for UD90 stacking configuration's stress distributions around the resin region in the y-plane, has lowered the comparison load around microchannel but that difference may be neglected. If we examine Figure 60 however, both for y-plane and z-plane, the maximum stress that occurs on the bottom of the model has increased. According to the Table 6 and Table 7, $[90/0]_{3s}$ stacking configuration has 7.8% increase in maximum tensile stress and 65.6% decrease in maximum compression stress in y-plane. As for z-plane this values are 7.8% increase and 60.4% increase respectively.

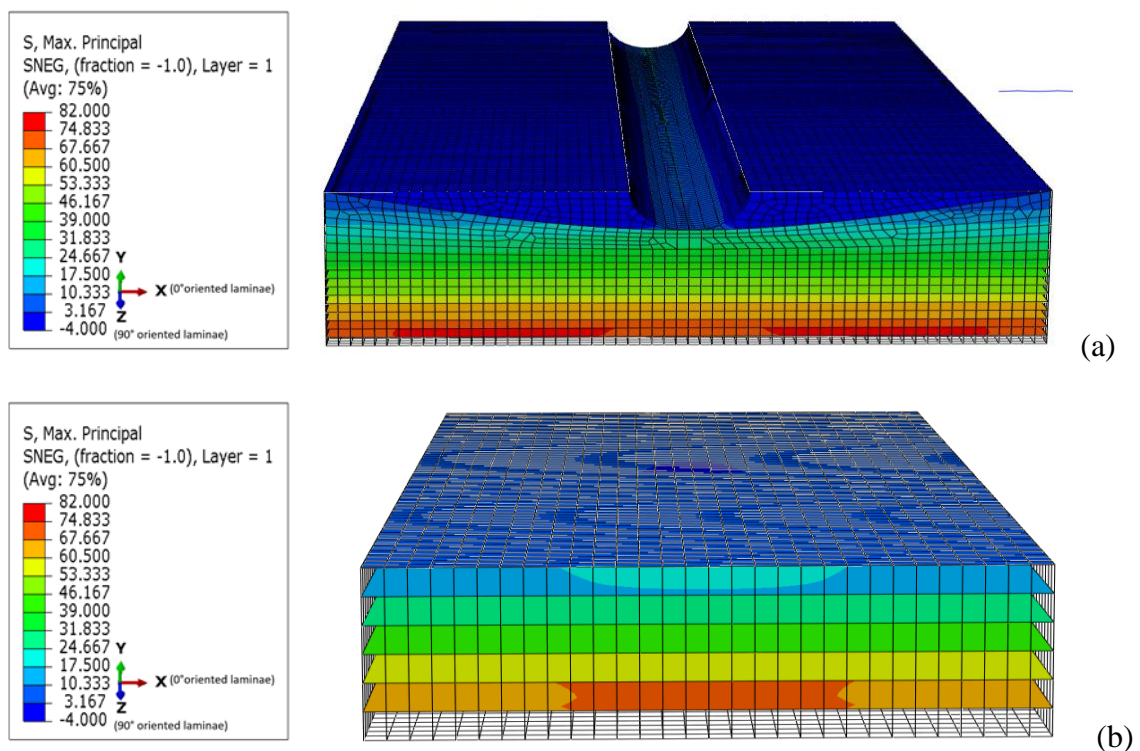


Figure 59: S,Max, Principal Stress Contours for the 3-Point Bending model with of UD90 Stacking Configuration for y-plane Cut for (a) with Microchannel (b) without Microchannel

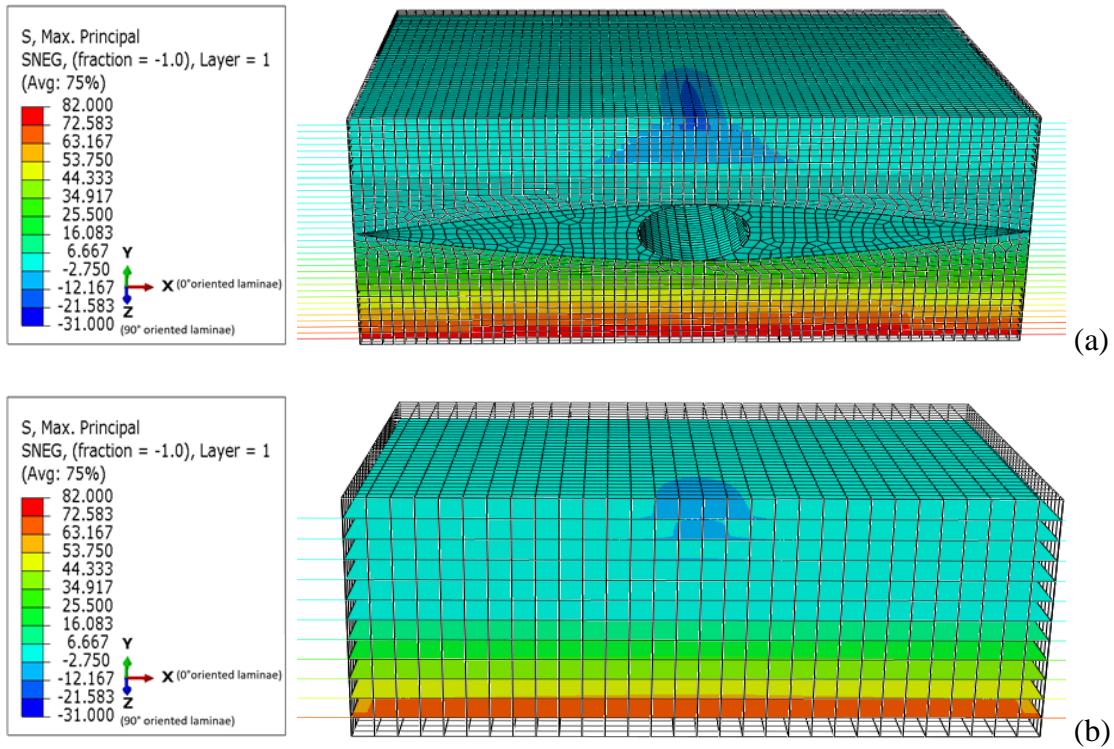


Figure 60: S,Max,Principal Stress Contours for the 3-Point Bending Model with of UD90 Stacking Configuration for z-plane cut for (a) with Microchannel (b) without Microchannel

6. CONCLUSIONS

6.1 Summary

FEM is an impressive tool that a designer use to understand the physics and mechanical behavior of the designed part before the part goes into production reducing the cost of manufacture. In this thesis, a comprehensive literature scanning is done to review the previous studies. Then, in order to research the stress concentration in the microvascular channel diameter of 1 mm. is analyzed with various stacking configurations by the use of ABAQUS/Standard FEM software.

The model geometry is obtained from the micro-pictures that is taken by micro-camera. The thesis presents brief information about composite materials later narrowed down to fiber reinforced composites. After this part, microvascular channels' area of utilization, manufacturing, mechanical behavior and modelling with FEM is presented. The numerical model that is developed with FEM the results that is obtained from this model is given.

6.2 Key Findings and Outcomes

The key findings and outcomes of the thesis may be given as the following:

- A 2D and 3D validation model has been developed for 3-D microvascular channels implemented to laminates. The results obtained are compared with Huang et al.[20]'s findings. And as a result, the validation model has validated successfully.
- The longitudinal stress distributions for transverse compression and tension, UD90 has the highest stress concentration. This is due to UD90's fiber orientation being transverse to the loading direction, which makes it weaker
- The longitudinal stress distributions for transverse compression and tension, all stacking configurations have the highest stress concentration located between point B and point C. The main reason behind this may be because of the point B is standing between the void and the adjacent lamina.
- $[0/90]_{3s}$ has lower stress concentration comparing to $[90/0]_{3s}$ configuration under transverse loads.
- The normalized stress distribution for transverse tension is expected to somehow differ from the results obtained from the transverse compression considering the

general material behavior under tension and compression. This may be related of the load approaches. The Al-Shawk et al [21] , used 1% displacement to create reaction forces and then made the analysis for stress distribution. Meanwhile in the thesis, 50 MPa of pressure value for tension (-50 MPa) and compression (+50 MPa) is used. Considering the normalization process and being operating in the elastic region the solution may turn out like this.

- In the 3-Point Bending the results obtained from models with microchannel and without microchannel are compared. It is found that $[90/0]_{3s}$ has the optimum stacking configuration for bending loads reducing the maximum tensile stress around 2.9% and maximum compression stress reduction around 46.2% in y-plane. As for the z-plane these values are found to be 4.8% increase in maximum tensile stress and 50.8% increase in maximum compression stress. The main reason behind this is, $[90/0]_{3s}$ has 0° oriented laminate surrounding the microchannel that can withstand the loads caused by the bending. Another reason is, due to the 3 Point Bending's nature, the largest stress concentrations mostly occur at the bottom of the laminate which is also 0° oriented laminate.

6.3 Future Studies

Considering the results obtained within the thesis, some topics regarding the future studies are proposed as following:

- Crack propagation under 3 Point Bending on FRP composites with microvascular channels can be researched through.
- Different size of diameters for microvascular channels can be investigated to see how the diameters of the vasculs effect the stress concentrations.

REFERENCES

- [1] J. Baur and E. Silverman, "Challenges and Opportunities in Multifunctional Nanocomposite Structures for Aerospace Applications," *MRS Bull.*, vol. 32, no. 4, pp. 328–334, 2007.
- [2] K. Njuguna, J. and Pielichowski, "Polymer Nanocomposites for Aerospace Applications: Properties, Advanced Engineering Materials," *Adv. Eng. Mater.*, vol. 5, no. 11, pp. 769–778, 2003.
- [3] E. J. Garcia, D. S. Saito, L. Megalini, A. J. Hart, R. G. De Villoria, and B. L. Wardle, "Fabrication and Multifunctional Properties of High Volume Fraction Aligned Carbon Nanotube Thermoset Composites," *J. Nano Syst. Technol.*, 2009.
- [4] Q. Meng and J. Hu, "A review of shape memory polymer composites and blends," *Compos. Part A Appl. Sci. Manuf.*, vol. 40, no. 11, pp. 1661–1672, 2009.
- [5] J. Leng and S. Du, Eds., *Shape-Memory Polymers and Multifunctional Composites*. CRC Press, 2010.
- [6] N. K. James, U. Lafont, S. Van Der Zwaag, and W. A. Groen, "Piezoelectric and mechanical properties of fatigue resistant, self-healing PZT-ionomer composites," *Smart Mater. Struct.*, vol. 23, no. 5, pp. 1–9, 2014.
- [7] S. Minakuchi and N. Takeda, "Recent advancement in optical fiber sensing for aerospace composite structures," *Photonic Sensors*, vol. 3, no. 4, pp. 345–354, 2013.
- [8] M. Q. Zhang and M. Z. Rong, "Basics of Self-Healing: State of the Art," in *Self-Healing Polymers and Polymer Composites*, 2011.
- [9] J. P. Youngblood and N. R. Sottos, "Bioinspired Materials for Self-Cleaning and Self-Healing," *MRS Bull.*, vol. 33, no. 8, pp. 732–741, 2008.
- [10] E. B. Murphy and F. Wudl, "The world of smart healable materials," *Prog. Polym. Sci.*, vol. 35, no. 1–2, pp. 223–251, 2010.
- [11] D. Y. Wu, S. Meure, and D. Solomon, "Self-healing polymeric materials: A review of recent developments," *Prog. Polym. Sci.*, vol. 33, no. 5, pp. 479–522, 2008.
- [12] R. S. Trask, G. J. Williams, and I. P. Bond, "Bioinspired self-healing of advanced composite structures using hollow glass fibres," *J. R. Soc. Interface*, vol. 4, no. 13, pp. 363–71, 2007.
- [13] N. Sottos, S. White, and I. Bond, "Introduction: self-healing polymers and composites," *J. R. Soc. Interface*, vol. 4, no. 13, pp. 347–348, 2007.
- [14] B. D. Kozola, L. A. Shipton, V. K. Natrajan, K. T. Christensen, and S. R. White, "Characterization of active cooling and flow distribution in microvascular polymers," *J. Intell. Mater. Syst. Struct.*, vol. 21, no. 12, pp. 1147–1156, 2010.
- [15] A. M. Aragón, C. J. Hansen, W. Wu, P. H. Geubelle, J. Lewis, and S. R. White, "Computational design and optimization of a biomimetic self-healing/cooling composite material," in *Behavior and Mechanics of Multifunctional and Composite Materials 2007*, 2007, p. 6526G.
- [16] J. W. C. Pang and I. P. Bond, "A hollow fibre reinforced polymer composite encompassing self-healing and enhanced damage visibility," *Compos. Sci. Technol.*, vol. 65, no. 11–12, pp. 1791–1799, 2005.
- [17] I. . Pang, J.W.C. and Bond, "Self-repair and enhanced damage visibility in

- a hollow fibre reinforced plastic," *11th Eur. Conf. Compos. Mater. Rhodes, Greece*, vol. B013, 2004.
- [18] S. Minakuchi, D. Sun, and N. Takeda, "Hierarchical system for autonomous sensing-healing of delamination in large-scale composite structures," *Smart Mater. Struct.*, vol. 23, no. 11, p. p115014, 2014.
- [19] T. J. Swait *et al.*, "Smart composite materials for self-sensing and self-healing," *Plast. Rubber Compos.*, vol. 41, no. 4–5, pp. 215–224, 2012.
- [20] C. Y. Huang, R. S. Trask, and I. P. Bond, "Characterization and analysis of carbon fibre-reinforced polymer composite laminates with embedded circular vasculature," *J. R. Soc. Interface*, vol. 7, no. 49, pp. 1229–1241, 2010.
- [21] A. Al-Shawk, H. Tanabi, and B. Sabuncuoglu, "Investigation of stress distributions in the resin rich region and failure behavior in glass fiber composites with microvascular channels under tensile loading," *Compos. Struct.*, vol. 192, pp. 101–114, 2018.
- [22] M. Altin Karataş and H. Gökkaya, "A review on machinability of carbon fiber reinforced polymer (CFRP) and glass fiber reinforced polymer (GFRP) composite materials," *Def. Technol.*, vol. 14, pp. 318–326, 2018.
- [23] P. K. MALLICK, *Fibre-reinforced composites: materials, manufacturing and design*, vol. 20, no. 2. 1989.
- [24] R. F. Gibson, *Principles of Composite Material Mechanics*, no. 205. 1994.
- [25] E. J. Barbero, *Introduction to Composite Materials Design*, 3rd ed. CRC Press, 2018.
- [26] J. Fleischer, R. Teti, G. Lanza, P. Mativenga, H. C. Möhring, and A. Caggiano, "Composite materials parts manufacturing," *CIRP Ann.*, vol. 67, pp. 603–626, 2018.
- [27] J. Frketic, T. Dickens, and S. Ramakrishnan, "Automated manufacturing and processing of fiber-reinforced polymer (FRP) composites: An additive review of contemporary and modern techniques for advanced materials manufacturing," *Addit. Manuf.*, vol. 14, pp. 69–87, 2017.
- [28] R. A. L. Gerdeen J.C., Rorrer, *Engineering Design with Polymers and Composites*, 2nd ed. CRC Press.
- [29] A. K. KAW, *Mechanics of Composite Materials. 2 ed. United States of America: CRC Press. 2006. 457 p. 2006.*
- [30] S. Rana. and R. Figueiro, *Advanced Composite Materials for Aerospace Engineering: Processing, Properties and Application. 2016.*
- [31] S. Rana, S. Parveen, and R. Figueiro, "Multiscale composites for aerospace engineering," in *Advanced Composite Materials for Aerospace Engineering*, 2016, pp. 1–15.
- [32] L. Ye, Y. Lu, Z. Su, and G. Meng, "Functionalized composite structures for new generation airframes: A review," *Compos. Sci. Technol.*, vol. 65, no. 9 SPEC. ISS., pp. 1436–1446, 2005.
- [33] J. Njuguna and K. Pielichowski, "Polymer nanocomposites for aerospace applications: Fabrication," *Adv. Eng. Mater.*, vol. 6, no. 4, pp. 193–203, 2004.
- [34] Y. Liu, H. Du, L. Liu, and J. Leng, "Shape memory polymers and their composites in aerospace applications: A review," *Smart Mater. Struct.*, vol. 23, no. 2, 2014.
- [35] N. K. James, D. Van Den Ende, U. Lafont, S. Van Der Zwaag, and W. A. Groen, "Piezoelectric and mechanical properties of structured PZT-epoxy

- composites,” *J. Mater. Res.*, vol. 28, no. 4, pp. 635–641, 2013.
- [36] K. Kuang and W. Cantwell, “Use of conventional optical fibers and fiber Bragg gratings for damage detection in advanced composite structures: A review,” *Appl. Mech. Rev.*, vol. 56, no. 5, pp. 493–513, 2003.
- [37] S. Soghrati, A. M. Aragón, and P. H. Geubelle, “Design of actively-cooled microvascular materials: A genetic algorithm inspired network optimization,” *Struct. Multidiscip. Optim.*, vol. 49, no. 4, pp. 643–655, 2014.
- [38] S. Soghrati *et al.*, “Computational analysis of actively-cooled 3D woven microvascular composites using a stabilized interface-enriched generalized finite element method,” *Int. J. Heat Mass Transf.*, vol. 65, pp. 153–165, 2013.
- [39] V. G. Pastukhov, Y. F. Maidanik, C. V. Vershinin, and M. A. Korukov, “Miniature loop heat pipes for electronics cooling,” *Appl. Therm. Eng.*, vol. 23, no. 9, pp. 1125–1135, 2003.
- [40] S. Soghrati, P. R. Thakre, S. R. White, N. R. Sottos, and P. H. Geubelle, “Computational modeling and design of actively-cooled microvascular materials,” *Int. J. Heat Mass Transf.*, vol. 55, no. 19–20, pp. 5309–5321, 2012.
- [41] A. P. Esser-Kahn *et al.*, “Three-dimensional microvascular fiber-reinforced composites,” *Adv. Mater.*, vol. 23, no. 32, pp. 3654–3658, 2011.
- [42] M. A. Burns *et al.*, “An integrated nanoliter DNA analysis device,” *Science (80-.)*, no. 282, pp. 484–487, 1998.
- [43] A. Strömberg, A. Karlsson, F. Ryttsén, M. Davidson, D. T. Chiu, and O. Orwar, “Microfluidic device for combinatorial fusion of liposomes and cells,” *Anal. Chem.*, vol. 73, pp. 126–130, 2001.
- [44] N. L. Jeon, S. K. W. Dertinger, D. T. Chiu, I. S. Choi, A. D. Stroock, and G. M. Whitesides, “Generation of solution and surface gradients using microfluidic systems,” *Langmuir*, vol. 16, pp. 8311–8386, 2000.
- [45] Y. Wang, G. Yuan, Y. K. Yoon, M. G. Allen, and S. A. Bidstrup, “Active cooling substrates for thermal management of microelectronics,” *IEEE Trans. Components Packag. Technol.*, vol. 28, no. 3, pp. 477–483, 2005.
- [46] X. Wei, Y. Joshi, and M. K. Patterson, “Experimental and Numerical Study of a Stacked Microchannel Heat Sink for Liquid Cooling of Microelectronic Devices,” *J. Heat Transfer*, vol. 29, no. 10, pp. 1432–1444, 2007.
- [47] R. B. Oueslati, D. Therriault, and S. Martel, “PCB-integrated heat exchanger for cooling electronics using microchannels fabricated with the direct-write method,” *IEEE Trans. Components Packag. Technol.*, vol. 31, no. 4, pp. 869–874, 2008.
- [48] C. J. Norris, I. P. Bond, and R. S. Trask, “Healing of low-velocity impact damage in vascularised composites,” *Compos. Part A Appl. Sci. Manuf.*, vol. 44, pp. 78–85, 2013.
- [49] A. S. Wu *et al.*, “Sensing of damage and healing in three-dimensional braided composites with vascular channels,” *Compos. Sci. Technol.*, vol. 72, no. 13, pp. 1618–1626, 2012.
- [50] C. J. Norris, I. P. Bond, and R. S. Trask, “Interactions between propagating cracks and bioinspired self-healing vasculature embedded in glass fibre reinforced composites,” *Compos. Sci. Technol.*, vol. 71, no. 6, pp. 847–853, 2011.
- [51] C. J. Norris, I. P. Bond, and R. S. Trask, “The role of embedded bioinspired vasculature on damage formation in self-healing carbon fibre reinforced

- composites," *Compos. Part A Appl. Sci. Manuf.*, vol. 42, no. 6, pp. 639–648, 2011.
- [52] C. J. Norris, G. J. Meadway, M. J. O'Sullivan, I. P. Bond, and R. S. Trask, "Self-healing fibre reinforced composites via a bioinspired vasculature," *Adv. Funct. Mater.*, vol. 21, no. 19, pp. 3624–3633, 2011.
- [53] R. S. Trask and I. P. Bond, "Bioinspired engineering study of Plantae vasculures for self-healing composite structures," *J. R. Soc. Interface*, vol. 7, no. 47, p. 921, 2010.
- [54] A. R. Hamilton, N. R. Sottos, and S. R. White, "Local strain concentrations in a microvascular network," *Proc. Soc. Exp. Mech. Inc.*, vol. 50, no. 2, pp. 255–263, 2010.
- [55] J. C. Hung, D. H. Chang, and Y. Chuang, "The fabrication of high-aspect-ratio micro-flow channels on metallic bipolar plates using die-sinking micro-electrical discharge machining," *J. Power Sources*, vol. 198, pp. 158–163, 2012.
- [56] J. G. Hemrick, E. Lara-Curzio, E. R. Loveland, K. W. Sharp, and R. Schartow, "Woven graphite fiber structures for use in ultra-light weight heat exchangers," *Carbon N. Y.*, vol. 49, no. 14, pp. 4820–4829, 2011.
- [57] D. Roach, "Real time crack detection using mountable Comparative Vacuum monitoring sensors," *Smart Struct. Syst.*, vol. 5, no. 4, pp. 317–328, 2009.
- [58] A. Kousourakis, A. P. Mouritz, and M. K. Bannister, "Interlaminar properties of polymer laminates containing internal sensor cavities," *Compos. Struct.*, vol. 75, no. 1–4, pp. 610–618, 2006.
- [59] S. M. S. Ltd., "Comparative Vacuum Monitoring: a New Method of In-Situ Real-Time Crack Detection and Monitoring," 2004. .
- [60] M. Motuku, U. K. Vaidya, and G. M. Janowski, "Parametric studies on self-repairing approaches for resin infused composites subjected to low velocity impact," *Smart Mater. Struct.*, vol. 8, no. 5, p. 623, 1999.
- [61] C. Dry, "Procedures developed for self-repair of polymer matrix composite materials," *Compos. Struct.*, vol. 35, no. 3, pp. 263–269, 1996.
- [62] C. M. Dry and N. R. Sottos, "Passive smart self-repair in polymer matrix composite materials," pp. 438–444, 1993.
- [63] Bond. I.P, "Self-repairing hollow fibre composites," *Reinf. Plast.*, vol. 48, no. 8, p. 16, 2004.
- [64] M. Hucker, I. Bond, S. Bleay, and S. Haq, "Investigation into the behaviour of hollow glass fibre bundles under compressive loading," *Compos. Part A Appl. Sci. Manuf.*, vol. 34, no. 11, pp. 1045–1052, 2003.
- [65] I. Bond, M. Hucker, S. Bleay, and S. Haq, "Optimising the Performance of Hollow Glass Fibre/Epoxy Composites Under Compressive Loading," in *43rd AIAA/ASME/ASCE/AHS/ASC Structures, Structural Dynamics, and Materials Conference*, 2002.
- [66] M. Hucker, I. Bond, A. Foreman, and J. Hudd, "Optimisation of hollow glass fibres and their composites," *Adv. Compos. Lett.*, vol. 8, no. 4, pp. 181–189, 1999.
- [67] A. Kousourakis, M. K. Bannister, and A. P. Mouritz, "Tensile and compressive properties of polymer laminates containing internal sensor cavities," *Compos. Part A Appl. Sci. Manuf.*, vol. 39, no. 9, pp. 1394–1403, 2008.
- [68] A. M. Coppola, P. R. Thakre, N. R. Sottos, and S. R. White, "Tensile

- properties and damage evolution in vascular 3D woven glass/epoxy composites,” *Compos. Part A Appl. Sci. Manuf.*, vol. 59, pp. 9–17, 2014.
- [69] A. T. T. Nguyen and A. C. Orifici, “Structural assessment of microvascular self-healing laminates using progressive damage finite element analysis,” *Compos. Part A Appl. Sci. Manuf.*, vol. 43, no. 11, pp. 1886–1894, 2012.
- [70] D. J. Hartl, G. J. Frank, and J. W. Baur, “Effects of microchannels on the mechanical performance of multifunctional composite laminates with unidirectional laminae,” *Compos. Struct.*, vol. 143, pp. 242–254, 2016.
- [71] N. Kharghani, C. G. Soares, and N. G. Tsouvalis, “Experimental and numerical study of the bolt reinforcement of a composite-to-steel butt-joint under three-point bending test,” *Mar. Struct.*, vol. 63, no. May 2018, pp. 384–403, 2019.
- [72] W. Fan *et al.*, “Fatigue behavior of the 3D orthogonal carbon / glass fibers hybrid composite under three-point bending load,” *Mater. Des.*, vol. 183, p. 108112, 2019.
- [73] L. Wu, F. Zhang, B. Sun, and B. Gu, “International Journal of Mechanical Sciences Finite element analyses on three-point low-cyclic bending fatigue of 3-D braided composite materials at microstructure level,” *Int. J. Mech. Sci.*, vol. 84, pp. 41–53, 2014.
- [74] X. Jia, Z. Xia, and B. Gu, “Numerical analyses of 3D orthogonal woven composite under three-point bending from multi-scale microstructure approach,” *Comput. Mater. Sci.*, vol. 79, pp. 468–477, 2013.
- [75] ASTM, “Standard Test Method for Flexural Properties of Polymer Matrix Composite Materials,” 2017.
- [76] J. S. and S. V. L. H. Tanabi, B. Sabuncuoglu, “Micro-CT measurement of fiber disturbance and composite stiffness: Application to in glass-fiber reinforced composites with embedded microvascular channels,” 2019.
- [77] Huntsman Corporation, “‘Araldite LY 564/ Aradur 2954,’ ed,” 2011.
- [78] K. Shivakumar and A. Bhargava, “Failure mechanics of a composite laminate embedded with a fiber optic sensor,” *J. Compos. Mater.*, vol. 39, no. 9, pp. 777–798, 2005.



HACETTEPE UNIVERSITY
GRADUATE SCHOOL OF SCIENCE AND ENGINEERING
THESIS/DISSERTATION ORIGINALITY REPORT

HACETTEPE UNIVERSITY
GRADUATE SCHOOL OF SCIENCE AND ENGINEERING
TO THE DEPARTMENT OF MECHANICAL ENGINEER

Date: 24/09/2019

Thesis Title / Topic: Investigation of Stress Distribution in Glass Fiber Reinforced Composite Materials with Microvascular Channels Under Tranverse Loading And Bending

According to the originality report obtained by my thesis advisor by using the *Turnitin* plagiarism detection software and by applying the filtering options stated below on 23/09/2019 for the total of 67 pages including the a) Title Page, b) Introduction, c) Main Chapters, d) Conclusion sections of my thesis entitled as above, the similarity index of my thesis is 10 %.

Filtering options applied:

1. Bibliography/Works Cited excluded
2. Quotes excluded
3. Match size up to 5 words excluded

I declare that I have carefully read Hacettepe University Graduate School of Sciene and Engineering Guidelines for Obtaining and Using Thesis Originality Reports; that according to the maximum similarity index values specified in the Guidelines, my thesis does not include any form of plagiarism; that in any future detection of possible infringement of the regulations I accept all legal responsibility; and that all the information I have provided is correct to the best of my knowledge.

I respectfully submit this for approval.

Date and Signature

Name Surname: Abdullah Gencer ATASOY

Student No: N13124676

Department: Mechanical Engineering

Program:

Status: Masters Ph.D. Integrated Ph.D.

24/09/2019

ADVISOR APPROVAL

APPROVED.

Assoc. Prof. Dr. Barış SABUNCUOĞLU

CURRICULUM VITAE

Credentials

Name, Surname : Abdullah Gencer ATASOY
Place of Birth : Keçiören / Ankara
Material Status : Married
E-mail : abduallahgenceratasoy@gmail.com
Address : Ankara, TURKEY

Education

BSc. : Gazi University Engineering and Architecture
Faculty Mechanical Engineering Department (2006-2011)
MSc. : -
PhD. : -

Foreign Language

English

Work Experience

2012 - 2013: Turkish Republic Ministry of Labor and Social Security - Occupational Safety and Health Associate

2013 - : Turkish Republic Presidency of Defense Industries, Defense Industries Senior Associate